



**POLITECNICO DI TORINO  
SAMARA STATE AEROSPACE UNIVERSITY**

---

DIMEAS

Corso di Laurea Magistrale in Ingegneria Aerospaziale

TESI DI LAUREA MAGISTRALE

**Study of the influence of blades arrangement  
on the mode shapes and stress scatter**

Candidato:

**Marco Convertini**

Matricola 231248

Relatore:

**Daniele Botto**

Correlatore:

**Aleksandr Urlapkin**

*a Mamma, Papà e Luca*

## **Abstract**

The purpose of this project is to investigate the influence of different mistuned blades arrangements on free-vibration response and dynamics of bladed disk. This rotor belongs to the first stage of the Low Pressure Compressor (LPC) in the NK-36ST engine, used as Gas Turbine Unit. Firstly, will be analyzed the influence of different mistuned patterns on mode shapes and natural frequencies. Then, a finite elements model of the LPC will be created and a CFD simulation run in order to evaluate the exciting aerodynamic force acting on each blade. The estimated force, written in harmonic form in function of Engine Order and time, will be used to excite blades in a transient structural analysis so as to minimize stress scatter and find the best mistuned arrangement.

## Sommario

L'obiettivo di questa tesi è di studiare l'influenza di diversi arrangiamenti di palette "mistuned" (stonate) sulla risposta a vibrazioni libere e sulla dinamica di un rotore provvisto di palette. Tale rotore fa parte del primo stadio del compressore di bassa pressione (LPC) della Gas Turbine Unit di manifattura russa NK-36ST. Dapprima, verrà analizzata l'influenza dell'utilizzo di diversi pattern sulle forme modali e sulle frequenze naturali del disco. Successivamente, verrà creato un modello ad elementi finiti del LPC per una simulazione CFD, con lo scopo di calcolare la forza aerodinamica agente su ogni paletta. La forza calcolata, scritta in forma armonica in funzione di Engine Order e tempo, verrà applicata sulle palette del disco in una analisi strutturale transitoria. Tale analisi è focalizzata nel trovare il miglior arrangiamento di palette stonate che riduce la concentrazione di stress lungo la circonferenza del disco.

# Acknowledgements

I thank all who in one way or another contributed in the completion of this thesis.

Foremost, I would like to express my gratitude to the thesis relators Prof. Daniele Botto from Politecnico di Torino and Prof. Aleksandr V. Urlapkin from the Samara State Aerospace University for the help, patience and support to my study and research.

I would also like to acknowledge Prof. Aleksandr S. Vinogradov for his continuous assistance during my studying period in Russia. His office door was always opened whenever I ran into a trouble spot.

Finally, I must express my profound gratitude to my parents and my friends for providing me with incessant support and encouragement throughout my years of study and, mostly, during difficult moments. This accomplishment would not have been possible without all of them.

# Glossary

**AR** Aspect Ratio

**B2B** Blade-to-Blade

**CFD** Computational Fluid Dynamics

**CFL** Courant-Friedrich-Levy

**CFV** Computational Field Visualization

**EO** Engine Order

**ER** Expansion Ratio

**GTE** Gas Turbine Engine

**GTU** Gas Turbine Unit

**HCF** High-Cycle Fatigue

**IGV** Inlet Guide Vane

**ITS** Initial Time Step

**LPC** Low-Pressure Compressor

**LPT** Low-Pressure Turbine

**PDF** Probability Density Function

**RANS** Reynolds Averaged Navier-Stokes

**RPM** Revolutions Per Minute

**SA** Spalart-Allmaras

**SET** Step End Time

**SST** Shear Stress Transport

# List of Figures

1.1	GTE components and ideal Joule-Brayton cycle . . . . .	3
1.2	The engine NK-36ST . . . . .	4
1.3	NK-36ST compressor units and LPC . . . . .	5
2.1	Example of stripe configuration . . . . .	14
2.2	Creation of the image mesh . . . . .	15
2.3	Examples of nodal diameters . . . . .	18
2.4	Motionless and rotating coordinate systems . . . . .	18
2.5	An example of Campbell diagram showing the relationship between natural frequencies, rotational speed and engine orders of the excitation (radial lines) . . . . .	19
3.1	Blades and flow path definition . . . . .	23
3.2	Compressor stages definition . . . . .	23
3.3	Cell representation . . . . .	24
3.4	B2B mesh parameters visualization . . . . .	25
3.5	Mesh generation steps . . . . .	26
3.6	Flow path and stages settings . . . . .	27
3.7	B2B Mesh Control Box . . . . .	28
3.8	3D mesh view and Grid quality box . . . . .	29
3.9	Blade modelling . . . . .	30
3.10	Disk modelling . . . . .	32
4.1	Fluid selection window . . . . .	34
4.2	Flow model page . . . . .	35
4.3	Rotating machinery page . . . . .	36
4.4	Boundary conditions page . . . . .	38
4.5	Numerical model interface . . . . .	39
4.6	Division of the meridional view in meridional sectors . . . . .	41
4.7	Initial solution for turbomachinery interface . . . . .	42
4.8	The Control Variables page . . . . .	43
4.9	Performance curve definition . . . . .	44
4.10	Influence of ER on performance curves . . . . .	47
4.11	Influence of MR on performance curves . . . . .	48
4.12	Influence of $y^+$ on performance curves . . . . .	49
4.13	Influence of mesh density on performance curves . . . . .	50
4.14	Influence of ER on flow visualization . . . . .	51
4.15	Influence of MR in flow visualization . . . . .	52
4.16	Influence of $y^+$ on flow visualization . . . . .	53

4.17	Influence of mesh density in flow visualization . . . . .	54
4.18	Influence of O-layer in flow visualization . . . . .	55
4.19	Influence of $ER_{B2B}$ on CFD results . . . . .	56
4.20	Visualization of the aerodynamic force acting on the $i$ -th blade . . . . .	58
4.21	LPC map of the NK36-ST . . . . .	58
5.1	Mesh and supports definition of the bladed disk . . . . .	59
5.2	Linear relationship extrapolation . . . . .	61
5.3	Gaussian distribution of frequencies and Young's modulus computation . . . . .	61
5.4	Different mistuned blades patterns visualization . . . . .	63
5.5	Free-vibration natural frequencies vs nodal diameters . . . . .	64
5.6	Mode shapes of the tuned bladed disk . . . . .	64
5.7	Sinusoidal patterns for some nodal diameters-mode shapes of the tuned bladed disk . . . . .	65
5.8	Localized mode shape of the mistuned bladed disk . . . . .	66
5.9	Vibration localization parameter vs nodal diameter-modes . . . . .	67
5.10	Vibration localization parameter bar charts . . . . .	68
5.11	Linking of modal and structural analysis objects . . . . .	69
5.12	Campbell diagram of the NK-36ST LPC rotor . . . . .	70
5.13	Transient Structural analysis settings . . . . .	71
5.14	Displacement results of the first blade over time . . . . .	73
5.15	Displacement pattern along disk circumference for the EO 3 . . . . .	74
5.16	Displacement pattern along disk circumference for the EO 4 . . . . .	75
A.1	FP mesh parameters . . . . .	78
A.2	FP mesh parameters . . . . .	79
A.3	B2B mesh parameters . . . . .	80
A.4	B2B mesh parameters . . . . .	81
B.1	Shroud coordinates . . . . .	82
B.2	Blade sections coordinates . . . . .	83
C.1	Mode 1 variations in normalized displacements from tuned system for different mistuned patterns. . . . .	85
C.2	Mode 2 variations in normalized displacements from tuned system for different mistuned patterns. . . . .	86
C.3	Mode 3 variations in normalized displacements from tuned system for different mistuned patterns. . . . .	87
C.4	Mode 4 variations in normalized displacements from tuned system for different mistuned patterns. . . . .	88
C.5	Mode 5 variations in normalized displacements from tuned system for different mistuned patterns. . . . .	89
C.6	Mode 6 variations in normalized displacements from tuned system for different mistuned patterns. . . . .	90
C.7	Mode 7 variations in normalized displacements from tuned system for different mistuned patterns. . . . .	91
C.8	Mode 8 variations in normalized displacements from tuned system for different mistuned patterns. . . . .	92
C.9	Mode 9 variations in normalized displacements from tuned system for different mistuned patterns. . . . .	93

C.10 Mode 10 variations in normalized displacements from tuned system for different mistuned patterns. . . . .	94
C.11 Mode 11 variations in normalized displacements from tuned system for different mistuned patterns. . . . .	95
C.12 Mode 12 variations in normalized displacements from tuned system for different mistuned patterns. . . . .	96
C.13 Mode 13 variations in normalized displacements from tuned system for different mistuned patterns. . . . .	97

# List of Tables

1.1	NK-36ST technical data . . . . .	4
1.2	LPC number of blades and tip clearances . . . . .	6
3.1	Disk geometrical characteristics . . . . .	31
4.1	Mesh parameters summary . . . . .	46
4.2	Aerodynamic exciting force and torque components . . . . .	57
5.1	Titanium alloys mechanical properties . . . . .	60
5.2	$\gamma$ values for different arrangements in EO 3 . . . . .	73
5.3	$\gamma$ values for different arrangements in EO 4 . . . . .	73

# Contents

<b>1</b>	<b>Introduction</b>	<b>1</b>
1.1	Historical Background and Definition of the Problem . . . . .	1
1.2	Literature review on bladed disk vibration . . . . .	2
1.3	Turbomachinery and its applications . . . . .	2
1.3.1	Gas Turbine Engines . . . . .	3
1.3.2	The NK-36ST LPC . . . . .	5
1.4	Introduction to the Softwares Used . . . . .	6
1.5	An overview of the thesis . . . . .	7
<b>2</b>	<b>Theoretical and Mathematical background</b>	<b>9</b>
2.1	CFD theory and models . . . . .	9
2.1.1	Navier-Stokes equations . . . . .	9
2.1.2	Time Averaging of Navier-Stokes equations . . . . .	10
2.1.3	Turbulence in RANS equations . . . . .	11
2.1.4	Turbulence models . . . . .	12
2.1.5	Dedicated turbomachinery models and mixing plane approach . . . . .	13
2.2	Vibration in turbomachinery . . . . .	16
2.2.1	Static analysis . . . . .	16
2.2.2	Modal analysis . . . . .	16
2.2.3	Nodal diameters and engine order excitation . . . . .	17
2.2.4	The resonance diagram . . . . .	19
2.2.5	Transient dynamic analysis . . . . .	20
2.2.6	Guidelines for Integration Step Size . . . . .	21
<b>3</b>	<b>Numerical model of the bladed disk</b>	<b>22</b>
3.1	Introduction . . . . .	22
3.2	Creation of model for CFD analysis . . . . .	22
3.2.1	Mesh parameters . . . . .	22
3.2.2	Project setup . . . . .	26
3.2.3	Flow paths control . . . . .	26
3.2.4	Blade to Blade control . . . . .	28
3.2.5	3D mesh generation and mesh optimization . . . . .	28
3.3	Creation of 3D model for ANSYS Mechanical simulations . . . . .	29
<b>4</b>	<b>CFD analysis. Defining of the excitation force</b>	<b>33</b>
4.1	Introduction . . . . .	33
4.2	Settings and flow simulation solver . . . . .	33
4.2.1	Fluid model . . . . .	34

4.2.2	Flow model . . . . .	34
4.2.3	Rotating machinery . . . . .	35
4.2.4	Boundary conditions . . . . .	37
4.2.5	Numerical model . . . . .	39
4.2.6	Initial solution . . . . .	40
4.2.7	Outputs . . . . .	41
4.2.8	Computation steering . . . . .	41
4.2.9	Performance curve . . . . .	43
4.3	Choice of the “best” mesh and CFD solution . . . . .	44
4.3.1	Influence of FP mesh parameters . . . . .	44
4.3.2	Influence of B2B mesh parameters . . . . .	45
4.3.3	Evaluation of the exciting aerodynamic force . . . . .	57
<b>5</b>	<b>Calculation of blades arrangement influence</b>	<b>59</b>
5.1	Introduction . . . . .	59
5.1.1	Mistuning modelling in the bladed disk . . . . .	60
5.1.2	Random geometric mistuning . . . . .	60
5.1.3	Creation of different mistuned patterns . . . . .	62
5.2	Modal analysis and influence on mode shapes . . . . .	62
5.2.1	Modal analysis of the tuned bladed disk . . . . .	62
5.2.2	Vibration of the mistuned bladed disk . . . . .	65
5.2.3	Modal analysis results . . . . .	66
5.3	Structural analysis and influence on stress scatter . . . . .	69
5.3.1	Static structural linked to modal analysis and Campbell diagram . . . . .	69
5.3.2	Transient structural analysis . . . . .	70
5.3.3	Transient analysis results . . . . .	72
<b>6</b>	<b>Conclusions and recommendations for future work</b>	<b>76</b>
<b>A</b>	<b>Mesh parameters</b>	<b>78</b>
<b>B</b>	<b>Blade section coordinates</b>	<b>82</b>
<b>C</b>	<b>Displacement patterns of mistuned blades arrangements</b>	<b>84</b>
	References . . . . .	98

# Chapter 1

## Introduction

*"Suppression of vibratory fatigue is the design challenge"*

---

Clarence Danforth, 1967

### 1.1 Historical Background and Definition of the Problem

Turbine engine rotors, and in general, bladed disks are complex dynamical systems. Exactly for this reason they are subjected not only to static forces, but they also suffer from serious vibration problems which can bring about unexpected failures due to fatigue. Bladed disk vibration first received significant attention from the research community in the late 1960s and the 1970s. Important early work was done by Whitehead, Wagner, Dye and Henry and Ewins. Vibratory failures occasionally occur in engine blades during final test phases, even if analytical predictions and computer simulations have not indicated a problem. Such was the case with the F-100 program (1950s) in which first-stage fan blade failures occurred during qualification tests. Even worse is the occurrence of failure of blades after an engine has successfully passed qualification tests and production has begun, as in the case of the General Electric engine J85-21. Of course, the worst situation ever is when failures occur in flight. One such example is the Cathay Pacific flight from Los Angeles during which a wide chord blade on an RB 211-524 G/H experienced a "primary failure" at 21,000 feet, the first of its kind for a component whose design had served well over 12 million engine hours [1]. Nowadays, engine vibration problems are key topics of national programs, technical congresses and expositions in the gas turbine engine community.

During the design process, all efforts are aimed at creating bladed disks with identical blades. However, there are always random deviations from the ideal situation caused by manufacturing tolerances and processes (milling, polishing, friction and welding), material inhomogeneity of the alloy, non-uniform wear during service, and other causes. This is called mistuning and it is unavoidable. It produces a lot of negative effects that have been studied for more than forty years. For instance, it can lead to mode localization and an increase of blade displacement and forced response as compared to those of the ideal, tuned bladed disks. Mistuning is usually very small and it can be characterized by fluctuations of the blade properties by 1-2%. The motivation for considering such small variations is that their effects on the forced response of bladed disks can be extremely large: they can lead to increases of the amplitude of vibration of some blades by 100% or more [2]. The correspondent increase in stresses can lead to premature High-Cycle

Fatigue (HCF) of the blades and it brings with itself a major cost, safety and reliability issue for gas-turbine engines. For instance, in 1998 it was estimated by the U.S. Air Force that about 55% of fighter jet engine safety mishaps (over \$1 million in damage) and 30% of all jet engine maintenance costs were due to HCF [3]. So it is widely clear how it is important and essential to predict and reduce the blades forced response increase due to mistuning.

## 1.2 Literature review on bladed disk vibration

In the last 40 years important progress has been made in structural modeling, analysis, understanding and prediction of mistuned bladed disk vibration. Important considerations on this topic are how to identify mistuning that is actually present in a manufactured bladed disk. For rotors with inserted blades, the blade-alone natural frequencies can be measured in order to verify the mistuning grade. However, for compressor stages with *blisk* configuration, blades can not be removed from the assembly. For this reason, mistuning identification techniques were developed in order to predict the behaviour of the bladed disk in terms of vibration, especially by Judge, Bladh, Feiner and Griffin [10].

Other important developments were made in the use of intentional mistuning in the design of rotors. Forced response amplitudes for mistuned disks are much greater than those of tuned rotors. However, it was demonstrated that the ratio of mistuned to tuned maximum vibration amplitudes is largest at small levels of mistuning. These amplitudes tends to increase with increasing mistuning up to a certain level, but a further increase in mistuning actually results in lower amplitudes. Castanier and Pierre demonstrated that intentional mistuning can be used in the design of bladed disk in order to avoid large forced response amplitudes and stresses that are caused by random mistuning.

A further step forward in the study of mistuned bladed disk vibration related problems was made with optimization analysis of intentional mistuned patterns, i.e. the work by Beirow, Giersch, Kuhhorn and Nipkau "*Optimization-Aided Forced Response Analysis of a Mistuned Compressor Blisk*". They studied the effects of vibration in mistuned disks with varying mistuning, engine order excitations and the consideration of aerodynamic influence. Furthermore, depending on the latter two factors, two different mistuning patterns (one-blade-mistuned and alternating mistuning pattern) were analyzed in order to find the best one with respect to the maximum blade displacement. From this research, the alternating mistuning pattern seemed to be a good way to reduce the blade forced response in case of low engine order excitation.

## 1.3 Turbomachinery and its applications

The term turbomachinery describes a machine that transfer energy between a flowing fluid and a rotor (or impeller), i.e. a rotating bladed wheel of a compressor or a turbine. The rotor is immersed in fluid continuum which can be gas, steam, water or air. When energy is transferred from the rotor to the fluid, the machine is called compressor, fan or pump. Vice versa, a turbine transfers energy from the fluid to the rotor. The rotor produces a change in stagnation enthalpy, kinetic energy and stagnation pressure of the fluid.

Turbomachines are the fundamental components in:

- aircraft, marine and space propulsion systems;
- hydraulic, steam and gas turbines;
- stationary industrial applications.

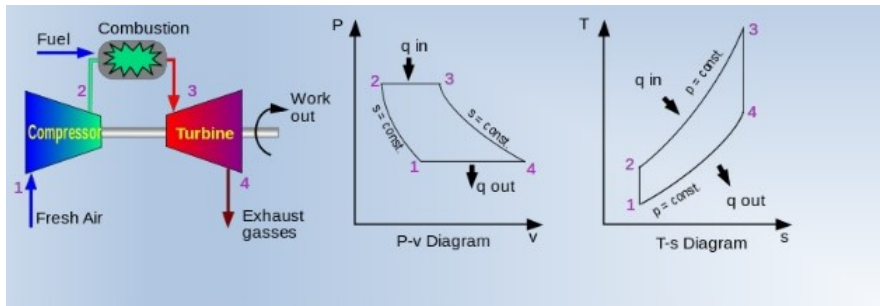


Figure 1.1: GTE components and ideal Joule-Brayton cycle

Turbomachines can be classified in several groups, depending on various aspects. First of all, they can be divided into two main groups:

- *extended* machines, without a shroud or annulus in correspondence of the blades tips. These "open" machines act on an infinite extent of fluid. For instance, aircraft and ship propellers or wind turbines;
- *enclosed* machines, which are housed in a casing so that the machine operates on a finite quantity of fluid that passes through the housing.

The enclosed turbomachines can be also classified according to the direction of the flow path:

- *axial* flow machines, if the flow direction is parallel to the axis of rotation;
- *radial* or *centrifugal* machines, if the flow is predominantly perpendicular to the axis of rotation;
- *mixed* flow machines, if the flow is partially axial and partially radial.

### 1.3.1 Gas Turbine Engines

One of the most widely spread applications of turbomachinery is the Gas Turbine Engine (GTE), which is a type of internal combustion engine that transforms the chemical energy of the fuel. The GTE realizes the Joule-Brayton cycle and, in its simplest configuration, consists of a compressor placed on the same shaft of a turbine and a combustion chamber located between these two components. The set compressor-turbine shaft is called spool. From the thermodynamic point of view, the ideal Joule-Brayton cycle consists of four processes: an isentropic compression, an isobaric combustion, an isentropic expansion and an isobaric heat rejection (Fig. 1.1). Of course, in the real cycle the compression and expansion are not isentropic and the combustion is not isobaric because of pressure drops in the combustion chamber. A GTE may consist of several spools (generally two, more rarely three) which rotate at different speeds in order to optimize the compression efficiency. The extracted energy is made available as shaft power or thrust.

The main applications of GTE are for aircraft and space propulsion units, but they are also widely used as stationary industrial units in many countries. In this case, the design of the engine significantly differ from a GTE and it is usually called Gas Turbine Unit (GTU). For example, in Russia, large stocks of gas and petroleum are situated very far from the main places of consumption. Due to the increasing economic competition with foreign companies, such as Boeing or Airbus, in many Russian engine plants, after the Soviet period, the demand for their products dramatically decreased. It was for this reason that they began to seek for new markets



Figure 1.2: The engine NK-36ST

Table 1.1: NK-36ST technical data

Output shaft power	26500	kW
Rotational speed of turbine rotor	5000	rpm
Exhaust gas temperature	730 (457)	K (C°)
Fuel consumption	5233	$\frac{kg}{h}$
Fuel	Natural gas	
Drive efficiency	36,5 %	
Mass	8690	kg
Specified life	45000	hrs
Overall dimensions		
Length	6000	mm
Diameter	2300	mm

for their engines. The main direction of this research became the industrial application of Gas Turbine Units, specially for gas pumping or electricity generation. Several GTUs were created on the basis of existing aircraft and marine gas turbine engines.

### The NK-36ST

The GTU object of this work is a Russian engine named NK-36ST (Fig.1.2), produced in Samara by the *JSC Kuznetsov* in 1993. *JSC Kuznetsov* is one of the prominent participants of the GTU Russian market. This company produces a family of gas turbines for driving gas pumping units and power plants ranging from 4 to 32 MW. The engine NK-36ST, with a capacity of about 27 MW, takes an important place in this context. Its main characteristics are shown in Tab. 1.1 [4].

The NK-36ST is created on the base of the aircraft engine NK-32 (more than the 60% of its design). It combines the last achievements in the field of the aircraft engine manufacturing and the great experience in the operation of the most used GTUs NK-12ST, NK-14ST on the cross-country gas pipe-lines. The engine NK-36ST is characterised by high operation reliability, high efficiency and improved technical data in comparison with the original aircraft engine equipped

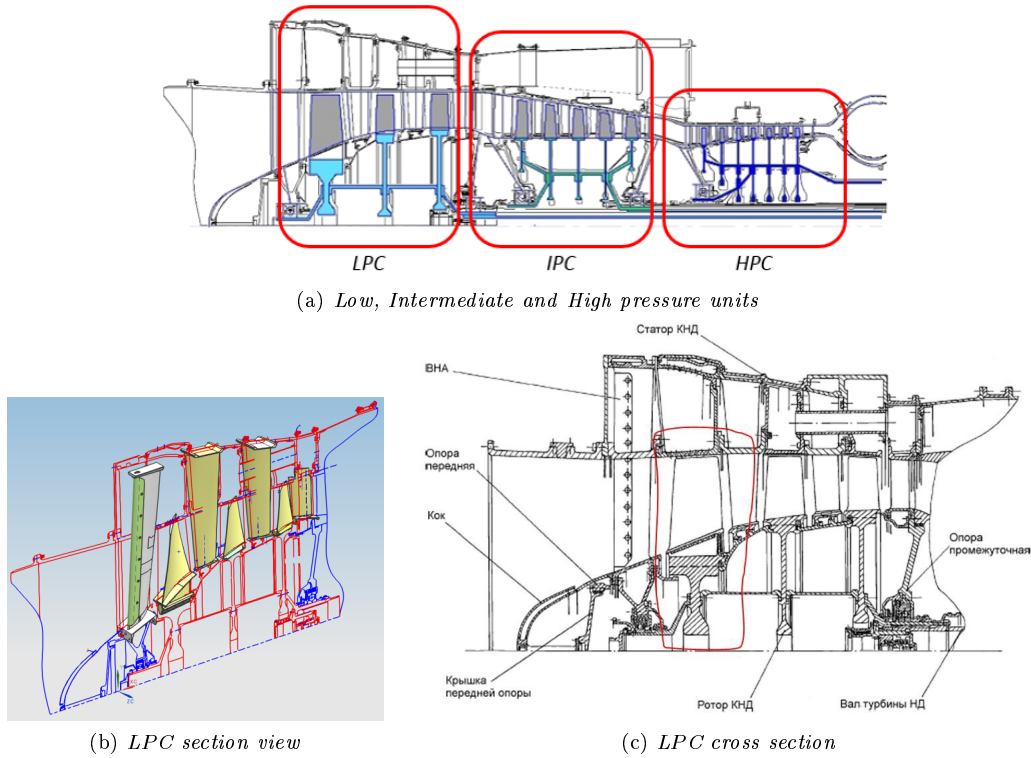


Figure 1.3: NK-36ST compressor units and LPC

on the strategic bomber Tu-160. The level of NO<sub>x</sub> emission is reduced to 120 mg/m<sup>3</sup> on the engine. This is less than the norm (150 mg/m<sup>3</sup>). Tolerance, control, protection and alarm systems (which secure the automatic starting and detect failures) are provided for this engine. In addition, the anti-ice system, which permits to operate at non-favorable atmospheric conditions is also provided for it. The modular construction of the engine also permits an easy transport and highly increases its maintainability level. The gas-pumping unit, of which the engine NK-36ST is part, operates successfully in the Tolyatti gas station.

### 1.3.2 The NK-36ST LPC

The NK-36ST is a three-spool engine, therefore it is equipped with low, intermediate and high pressure units (Fig.1.3a). The turbomachinery object of the present work is its Low-Pressure Compressor (LPC) (Figs. 1.3b and 1.3c). It has three stages and their characteristics are shown in Tab. 1.2.

It is basically an axial compressor which continuously pressurize air. It is a rotating, airfoil-based compressor in which the working fluid principally flows parallel to the axis of rotation. It differs from other rotating compressors such as centrifugal compressors, in which the fluid flow has a "radial component" too. The energy level of the fluid increases as it flows through the compressor due to the action of the rotor blades which exert a torque on the fluid. The stationary blades, also called guide vanes, slow the fluid, converting the circumferential component of flow into pressure. The compressor is driven by the Low-Pressure Turbine (LPT) through the low pressure shaft. The compressor drum is retained by bearings (the number of bearings depends on

Table 1.2: LPC number of blades and tip clearances

	Blade#	Tip clearance [mm]
IGV	18	
R1	27	0,7
S1	34	
R2	39	0,5
S2	43	
R3	47	0,45
S3	56	

engine complexity) and the disk has a certain number of annular airfoil rows attached by means of fir-tree connections. The guide vanes are instead attached to the stationary tubular casing. A pair of rotating and stationary airfoils is called a stage. The rotating blades accelerate the fluid, while the guide vanes convert the increased rotational kinetic energy into static pressure through diffusion and redirect the flow direction of the fluid, preparing it for the rotor blades of the next stage. The cross-sectional area between rotor drum and casing is reduced in the flow direction to maintain an optimum Mach number using variable geometry as the fluid is compressed.

The work will be focused on the first stage of the LPC and, particularly, on the rotor. This is because the majority of mistuning and HCF related problems arise in rotating units. This rotor is preceded, as usual in GTEs, by an Inlet Guide Vane (IGV), which purpose is to direct the air-flow to the compressor. By transporting the air at the proper angle the inlet guide vane ensures the most efficient compression. In this engine the IGV blades are also equipped with electric heaters in order to avoid ice formation and to increase the flow temperature. The first stage is then followed by other two low compressor stages, in which the flow pass cross section and the blades height gradually decreases.

## 1.4 Introduction to the Softwares Used

The present thesis project has been carried on by using softwares in order to create 3D models, to mesh them and to calculate results in static and dynamic conditions. The used SWs are listed here:

- *Siemens NX* (v.8.5);
- *NUMECA Software*;
- *ANSYS Workbench* (v.16.2).

The first one, formerly known as *NX UniGraphics*, is an advanced CAD and CAM software package. It is currently used by a wide spread of industry sectors, from product design to automotive to aerospace. The software comes with a plethora of options and features to perform any sort of modeling job desired and it's really easy to use after some training. The software allows the user to create any kind of models, from the simplest geometric shape to complex parts ready for the manufacturing process. However, during the modelling process, it is always possible to activate or deactivate some features which make the model simpler and lighter, with lots of benefits from the processing time and computer memory points of view.

NUMECA is a Belgian company which is largely known today as the one of the most innovative in the field of Computational Fluid Dynamics (CFD) and multiphysics design, analysis

and optimization. Based on the most advanced technology, this software is largely recognized for its application-driven features and interface, optimal solutions including high quality automatic full hex meshing, accurate and fast CFD solvers, multi-physics, robust design and optimization with uncertainty quantification. NUMECA offers grid generation and some CFD optimization tools used in this work, with integrated software environments, such as Numeca/FINE™/Turbo, Numeca/IGG-Autogrid5™, Numeca/CFView™. They respectively provide features for the following items [5]:

- CFD suite for rotating machinery with incompressible and compressible fluids, from subsonic to hypersonic flow regimes;
- Full automatic hexahedral grid generation for all types of rotating machinery: complex axial, radial, and mixed-flow configurations;
- Polyvalent parallelized Computational Flow Visualisation software system.

Last but not least, *ANSYS Workbench*. It provides a comprehensive, user-friendly and integrated simulation system, a unique integration with CAD systems (*Siemens NX* included) and design processes and it is comprised of various applications [6], with the following employed in this thesis:

- *Mechanical* for performing some analyses using the ANSYS solver:
  - *Modal analysis*, for calculating vibrating characteristics, such as natural frequencies and mode shapes;
  - *Structural analysis*, for solving static linear or transient (time-dependent) studies.
- *Geometry (DesignModeler)* for creating and modifying CAD geometry to prepare the solid model for use in Mechanical;
- *Meshing Application* for generating CFD and Explicit Dynamics meshes.

## 1.5 An overview of the thesis

This thesis is divided into six chapters.

A mathematical basement is provided in Chapter 2. Firstly, Computational Fluid Dynamics theory and equations are examined, comprising turbulence models and approaches. Then, equations governing vibration in turbomachinery are analyzed, both for free-vibration and prestressed modal analysis.

In Chapter 3, the numerical model of the rotor disk is built. Two models need to be constructed, one for the CFD solver *NUMECA* and one for *ANSYS Mechanical*. The former needs an accurate analysis of mesh parameters in order to find their best combination and better simulate the flow dynamics. For the second model, instead, it is not necessary the same level of accuracy in the meshing phase. However, the 3D model has to be created through the CAD software, suitably meshed and constrained.

The actual CFD computation is discussed in Chapter 4. The whole procedure is explained, from loading the mesh file to the application of boundary conditions. Different CFD computations (addressed to different meshes) of an analogous compressor stage (*Stage 37*) are calculated. The mesh which best match experimental performance curves for the Stage 37 is chosen to represent the finite element model of the NK-36ST compressor stage. After the computation is completed, the exciting aerodynamic force acting on blades is calculated.

Chapter 5 deals with the analysis of the actual influence of different blades arrangements. At first a random mistuned set of blades is generated. Then different blade pattern are created and their vibrating characteristics are studied and compared with the tuned, ideal counterpart. Discrepancies in mode shapes and normalized displacements are used to choose the best arrangement. The second part of the chapter is dedicated to the transient structural analysis, in which the bladed disk is studied from a dynamic point of view. The aerodynamic force calculated in chapter 4 is now applied to each blade and compressor rotating velocity is applied.

## Chapter 2

# Theoretical and Mathematical background

### 2.1 CFD theory and models

In this section it is described in details the theoretical background of the physical and numerical models used in the CFD analysis through *Numeca FINE™/Turbo*. The equations governing the mechanics of fluids, the fluid and turbulence models, including boundary conditions and turbomachinery models are analyzed.

#### 2.1.1 Navier-Stokes equations

The *Navier-Stokes* equations are the fundamental partial differentials equations that describe the flow of compressible and incompressible fluids. They consist of the conservation equations of mass, momentum and energy. The general Navier-Stokes equations written in a Cartesian frame can be expressed as:

$$\frac{\partial}{\partial t} \int_{\Omega} U d\Omega + \int_S \vec{F}_I \cdot d\vec{S} + \int_S \vec{F}_V \cdot d\vec{S} = \int_{\Omega} S_T d\Omega \quad (2.1)$$

where  $\Omega$  is the volume and  $S$  the surface.  $U$  is the vector of the conservative variables:

$$U = \begin{bmatrix} \rho \\ \rho v_1 \\ \rho v_2 \\ \rho v_3 \\ \rho E \end{bmatrix} \quad (2.2)$$

$\vec{F}_I$  and  $\vec{F}_V$  are respectively the inviscid and viscous flux vectors:

$$\vec{F}_I = \begin{bmatrix} \rho v_i \\ \rho v_1 v_i + p \delta_{1i} \\ \rho v_2 v_i + p \delta_{2i} \\ \rho v_3 v_i + p \delta_{3i} \\ (\rho E + p) v_i \end{bmatrix} \quad (2.3)$$

$$-\vec{F}_V = \begin{bmatrix} 0 \\ \tau_{i1} \\ \tau_{i2} \\ \tau_{i3} \\ q_i + v_i \tau_{ij} \end{bmatrix} \quad (2.4)$$

where  $E$  is the total energy, defined by the sum of the molecular internal energy and the mechanical energy of the fluid elements, and  $q_i$  are the heat flux components, proportional to the temperature  $T$  ( $\kappa$  is the laminar thermal conductivity):

$$E = e + \frac{1}{2} v_i v_i \quad (2.5)$$

$$q_i = \kappa \frac{\partial}{\partial x_i} T \quad (2.6)$$

$S_T$  is the vector containing the source terms (considering no mass source or sinks):

$$S_T = \begin{bmatrix} 0 \\ \rho f_{e1} \\ \rho f_{e2} \\ \rho f_{e3} \\ W_f \end{bmatrix} \quad (2.7)$$

where  $f_{e1}$ ,  $f_{e2}$  and  $f_{e3}$  are the components of the external forces and  $W_f$  is the work accomplished by those external forces:

$$W_f = \rho \vec{f}_e \cdot \vec{v} \quad (2.8)$$

In this work it is used also another source term: gravity. To close the Navier-Stokes equations we need to specify the constitutive laws of the shear stress tensor  $\bar{\tau}$  in function of the other variables. For this study it is enough to consider only Newtonian fluids<sup>1</sup>. Considering the case of any reference frame, the constitutive law is given by:

$$\tau_{ij} = \mu \left[ \left( \frac{\partial v_j}{\partial x_i} + \frac{\partial v_i}{\partial x_j} \right) - \frac{2}{3} (\vec{\nabla} \cdot \vec{v}) \delta_{ij} \right] \quad (2.9)$$

### 2.1.2 Time Averaging of Navier-Stokes equations

In principle, the Navier-Stokes equations describe both laminar and turbulent flows. However, turbulence is a nonlinear process with a wide range of spatial and temporal scales. The direct simulation of complex turbulent flows in most engineering applications is not possible and will not be for the foreseeable future.

In the context of scale modelling, the most direct approach is offered by the partitioning of the flow field into a mean and fluctuating part. This process will produce the Reynolds Averaged Navier-Stokes (RANS) equations. The Reynolds averaged equations are derived by averaging the viscous conservation laws over a time interval  $T$ , large enough with respect to the time scales

---

<sup>1</sup>Fluids which obey the Newton's law of viscosity are called as Newtonian fluids. Newton's law of viscosity is given by  $\tau = \mu \frac{dv}{dy}$  where  $\tau$  is the shear stress,  $\mu$  is the viscosity of the fluid and  $\frac{dv}{dy}$  is the shear rate, rate of strain or velocity gradient. So the relation between the shear stress and the velocity gradient is linear. All gases and most liquids which have simpler molecular formula and low molecular weight such as water, benzene, ethyl alcohol, CCl<sub>4</sub>, hexane and most solutions of simple molecules are Newtonian fluids.

of the turbulent fluctuations, but small enough with respect to all other time-dependent effects. Time averaging is performed as follows.

The quantity  $A$  in the Navier-Stokes equations is time averaged related to the instantaneous value through:

$$A = \bar{A} + A' \quad (2.10)$$

where  $\bar{A}(\vec{x}, t) = \frac{1}{T} \int_{-T/2}^{T/2} A(\vec{x}, t + \tau) d\tau$

$\bar{A}$  is the time averaged value and  $A'$  is the fluctuating part, with  $\overline{A'} = 0$ . The density weighted average is defined through the equation:

$$\tilde{A} = \frac{\overline{\rho A}}{\bar{\rho}} \quad (2.11)$$

where  $A = \tilde{A} + A''$  and  $\overline{\rho A''} = 0$

Density and pressure are time averaged, while energy, velocity components and temperature are density weighted time averaged. The  $U$ ,  $\vec{F}_I$  and  $-\vec{F}_V$  vectors assume the following form:

$$U = \begin{bmatrix} \bar{\rho} \\ \bar{\rho}\tilde{v}_1 \\ \bar{\rho}\tilde{v}_2 \\ \bar{\rho}\tilde{v}_3 \\ \bar{\rho}\tilde{E} \end{bmatrix} \quad \vec{F}_I = \begin{bmatrix} \bar{\rho}\tilde{v}_i \\ \bar{\rho}\tilde{v}_1\tilde{v}_i + \frac{\overline{\rho v_1'' v_i''}}{\bar{\rho}} + \bar{p}\delta_{1i} \\ \bar{\rho}\tilde{v}_2\tilde{v}_i + \frac{\overline{\rho v_2'' v_i''}}{\bar{\rho}} + \bar{p}\delta_{2i} \\ \bar{\rho}\tilde{v}_3\tilde{v}_i + \frac{\overline{\rho v_3'' v_i''}}{\bar{\rho}} + \bar{p}\delta_{3i} \\ (\bar{\rho}\tilde{E} + \bar{p})\tilde{v}_i + \frac{\overline{\rho E'' v_i''}}{\bar{\rho}} + \bar{p}v_i'' \end{bmatrix} \quad -\vec{F}_V = \begin{bmatrix} 0 \\ \bar{\tau}_{i1} \\ \bar{\tau}_{i2} \\ \bar{\tau}_{i3} \\ \bar{q}_i + \overline{v_i \tau_{ij}} \end{bmatrix}$$

where the density averaged total energy is defined by:

$$\tilde{E} = \tilde{e} + \frac{1}{2}\tilde{v}_i\tilde{v}_i + \tilde{k} \quad (2.12)$$

while  $k$  is the turbulent kinetic energy:

$$k = \frac{1}{2} \left( \frac{\overline{\rho v_i'' v_i''}}{\bar{\rho}} \right) \quad (2.13)$$

### 2.1.3 Turbulence in RANS equations

The RANS equations have led to the introduction of the Reynolds stress tensor and the turbulent heat diffusion term. These quantities are unknown. This means that in order to solve the equations applied to turbulent flows it is needed a modelization of these unknown relations. This modelization is based both on theoretical analysis and on empirical information.

For the linear eddy viscosity turbulence models, the equation (2.14) is used for the Reynolds stress. They are evaluated using the *Bousinesq eddy viscosity* assumption.

$$-\overline{\rho v_i'' v_j''} = \mu_t \left[ \frac{\partial \tilde{v}_i}{\partial x_j} + \frac{\partial \tilde{v}_j}{\partial x_i} - \frac{2}{3} \left( \vec{\nabla} \cdot \vec{v} \right) \delta_{ij} \right] - \frac{2}{3} \bar{\rho} \tilde{k} \delta_{ij} \quad (2.14)$$

where  $\mu_t$  is the turbulent eddy viscosity. For the turbulent heat diffusion term, a gradient approximation is used:

$$c_p \overline{\rho v_i'' T} = -\kappa_t \frac{\partial \tilde{T}}{\partial x_i} \quad \kappa_t = \frac{\mu_t c_p}{Pr_t}$$

where  $\kappa_t$  is the turbulent thermal conductivity which can be expressed through the turbulent Prandtl number.

In the RANS equations the Reynolds stresses and the heat flux components are given by:

$$\bar{\tau}_{ij} = (\mu + \mu_t) \left[ \frac{\partial \tilde{v}_i}{\partial x_j} + \frac{\partial \tilde{v}_j}{\partial x_i} - \frac{2}{3} \left( \vec{\nabla} \cdot \vec{v} \right) \delta_{ij} \right] \quad \bar{q}_i = (\bar{\kappa} + \kappa_t) \frac{\partial \tilde{T}}{\partial x_i}$$

$\mu_t$  and  $\kappa_t$  need to be solved by the turbulence model. To this date, there is no single turbulence model that is best for all classes of problems. The choice of a model depends on many factors such as the physics of the flow under consideration, the level of accuracy required, the available computational resources, and the amount of time available for the simulation.

### 2.1.4 Turbulence models

Among the linear eddy viscosity turbulence models, many have been developed. They can be grouped into three main categories:

- Algebraic model:
  - Baldwin-Lomax
- 1-equation model:
  - Spalart-Allmaras (SA)
- 2-equation models:
  - $k - \varepsilon$  (Standard wall function)
  - $k - \varepsilon$  (Low Re Chien)
  - Shear Stress Transport (SST)

In the present work is used the Spalart-Allmaras model. It is a one equation turbulence model which can be considered as a bridge between the algebraic model of Baldwin-Lomax and the two equation models. It is very popular and common in CFD calculations because of its ability to treat complex flows. Its advantage in comparison with the Baldwin-Lomax model is that the turbulent eddy viscosity field is always continuous. On the other hand, compared with the  $k - \varepsilon$  model, it needs lower CPU and memory usage.

The SA model is based on the resolution of an additional transport equation which contains an advective, a diffusive and a source term and it is implemented in a non conservative form [8]. The turbulent viscosity is given by:

$$\nu_t = \tilde{\nu} f_{\nu 1} \tag{2.15}$$

where  $\tilde{\nu}$  is the turbulent working variable,  $\nu = \frac{\mu}{\rho}$  and  $f_{\nu 1}$  a function defined by:

$$f_{\nu 1} = \frac{\chi^3}{\chi^3 + c_{\nu 1}^3}$$

In the previous equation  $\chi$  is the ratio between the working variable  $\tilde{\nu}$  and the molecular kinematic viscosity  $\nu$ :

$$\chi = \frac{\tilde{\nu}}{\nu}$$

The turbulent working variable obeys the following transport equation:

$$\begin{aligned}
\frac{\partial \tilde{\nu}}{\partial t} + \tilde{v}_j \frac{\partial \tilde{\nu}}{\partial x_j} = & \underbrace{c_{b1}(1 - f_{t2})\tilde{S}\tilde{\nu}}_{\text{Production}} \\
& - \underbrace{\left[ c_{w1}f_{w1} - \frac{c_{b1}}{\kappa^2}f_{t2} \right] \left( \frac{\tilde{\nu}}{d} \right)^2}_{\text{Wall destruction}} \\
& + \underbrace{\frac{1}{\sigma} \left[ \frac{\partial}{\partial x_j} \left( (\nu + \tilde{\nu}) \frac{\partial \tilde{\nu}}{\partial x_j} \right) + c_{b2} \frac{\partial \tilde{\nu}}{\partial x_i} \frac{\partial \tilde{\nu}}{\partial x_i} \right]}_{\text{Diffusion}} \quad (2.16)
\end{aligned}$$

Additional definitions are given in [8].

### 2.1.5 Dedicated turbomachinery models and mixing plane approach

The challenges that occur within the modeling of systems containing rotating and swirling flows, such as turbomachinery, are essential. The first particularity of these systems is that they involve one or more rotative parts, that usually revolve about a single axis at given angular velocities and impart a motion to the fluid. Furthermore the relative motion between successive blade rows, boundary layers, shocks, wakes and tip leakage are sources of unsteadiness. All these phenomena are strictly coupled and they affect the performance of the machine.

Solving for such flows needs the solution of unsteady and viscous equations therefore the CFD solver has to manage enormous quantity of data. In order to simplify the solution and decrease the computer memory requirements is necessary to solve a steady flow field in a truncated computational domain. This requires the imposition of particular boundary conditions at the so-called *rotor/stator interfaces*. In the *Numeca FINE™/Turbo* environment these boundary conditions are known as the *mixing plane approach*. The rotor/stator interaction is done by exchanging circumferentially averaged flow quantities. Practically, it means that the blade separations occurring in the flow passage are mixed circumferentially before entering the downstream component. In this way, the pressure and the velocity components are uniform in the circumferential direction at the rotor/stator interface. The exchange of information at the interface then depends on the local direction of the flow. The mixing plane technique is the most used rotor/stator modelling and in *FINE™/Turbo* is possible to select between the following approaches:

- Default Mixing Plane Method;
- Full Non-matching Technique for Mixing Planes;
- Full Non-matching Technique with Frozen Rotor;
- Non Reflecting Boundary Conditions.

#### Default mixing plane method

This method imposes the following geometrical constraints:

- The patches on both sides of the rotor/stator interface must cover the same range in spanwise direction.
- The meshes need not to match in the spanwise direction but the azimuthal mesh lines on the boundaries must be circular arcs.

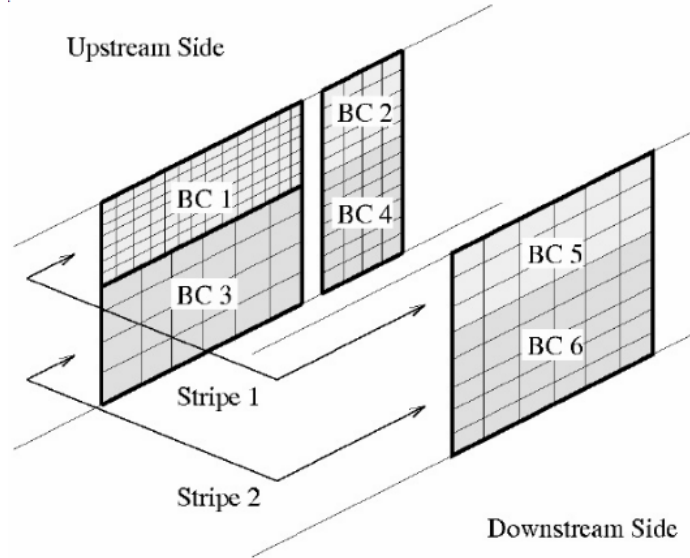


Figure 2.1: Example of stripe configuration

In this approach the rotor/stator interfaces are defined by stripes. The required averaging in tangential direction is carried out along each stripe. The upstream and the downstream sides are distinguished and each boundary condition must belong either to the upstream or to the downstream side. Fig. 2.1 shows these constraints. The upstream side of the interface is composed by three blocks, while there is a single block on the downstream side. The pitchwise grid lines have constant radius and the pitchwise line that joins the blocks BC 1 and BC 3 works as an inner grid line on all other boundaries. Finally the interface is decomposed into two stripes, stripe 1 consists of BC 1, BC 2 and BC 5, and stripe 2, consisting of BC 3, BC 4 and BC 6. Two kinds of boundary conditions are available in the *FINE<sup>TM</sup>/Turbo* interface:

- *The Conservative Coupling by Pitchwise Rows* (no flux decoding);
- *The Local Conservative Coupling* (with flux decoding).

The first approach operates the circumferential mixing and it is recommended due to its capability to provide an exact conservation of mass flow, momentum and energy through the interface. This approach adopts the same coupling procedure for all the nodes along the circumferential direction, even if the local flow direction is different from the averaged one. This technique offers the advantage of being able to guarantee a strict conservation of mass, momentum and energy through the interface. Moreover it shows to be very robust and is therefore used by default.

The second approach is only recommended for special cases, as the rotor/stator interface between an impeller and a volute. It is similar to the first technique except the fact that experience has shown that in cases where significant flow variations are observed in the circumferential direction (as for instance in the case of rotor-volute interactions) it is more stable to base the flux decomposition on the local flow direction. Small conservation errors can be observed with this technique, which is therefore only used for special configurations.

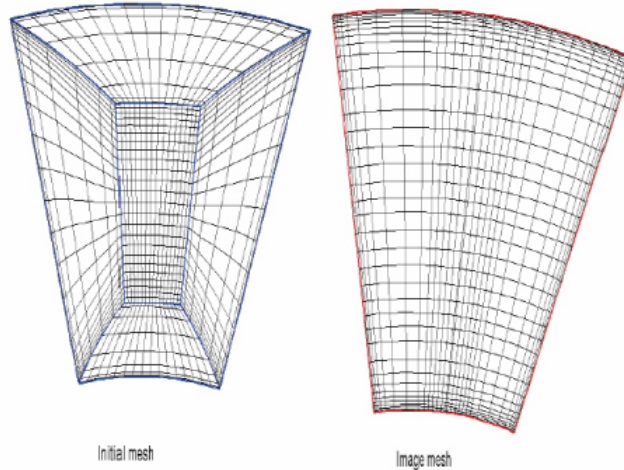


Figure 2.2: Creation of the image mesh

### Full non-matching technique for mixing planes

In order to avoid the great quantity of geometrical constraints required for the default mixing plane approach, a new interpolation technique is implemented. The full non matching mixing plane approach removes the geometrical constraints imposed by the default method. The only remaining constraint is that the rotor/stator patches should lie on the same common axisymmetric surface. This module uses the concept of *image*. On both sides of the interface between rotor and stator an image of the real mesh is built and they must match in spanwise direction. Each image is a "concatenation" of all the patches constituting the left or right side of the interface. The creation of the image mesh is illustrated in Fig. 2.2.

This method respects an exact conservation of mass flow, momentum and energy through the interface as the *Conservative Coupling by Pitchwise Rows* approach but has less geometric restrictions. Therefore it's recommended for most applications also because of small pre-processing CPU time and small memory requirements.

### Full non-matching technique with frozen rotor

The principle of the frozen rotor technique consists of neglecting the rotor movement in the connecting algorithm. The implementation is the same of the one adopted in the full non matching approach, except the fact that there is no rotation of the rotor image. For the rotor the governing equations are solved in a rotating frame of reference, while for the stator are solved in a absolute reference frame. In this way unsteady effects are neglected.

### Non reflecting boundary conditions

The complexity of solving multistaged systems is increased by the difficulty that CFD codes have to work with rotor/stator interfaces located close to blade rows. A common way to handle this problem is to use a steady-state non reflecting boundary condition based upon a characteristic analysis of the linearized Euler equations. This method uses the full non-matching technique and that the geometrical constraints associated with the default mixing plane approach are eliminated. This method is recommended when wave reflection is observed at the interface,

although attention should be paid to the mass flow conservation. Additional information are given in [7].

## 2.2 Vibration in turbomachinery

The goals of this section are to understand the fundamental mechanisms and principles governing the vibration phenomena in rotating structures.

Mathematical theory and numerical methods on which *ANSYS* Mechanical solver is based will be described in details. Firstly, the equations governing static structural analysis will be discussed. After that, the focus will move on the assumptions and description of modal analysis solvers. Finally, also dynamic time-dependent systems will be described for a complete understanding of the vibration characteristics in bladed rotating disks.

### 2.2.1 Static analysis

In static structural analysis inertial and damping effects are ignored. The overall equilibrium equations for linear structural analysis are:

$$[K]\{u\} = \{F^a\} + \{F^r\} \quad (2.17)$$

where  $[K] = \sum_{m=1}^N [K_e]$  is the total stiffness matrix,  $N$  is the number of elements,  $[K_e]$  the element stiffness matrix,  $\{u\}$  the nodal displacement vector,  $\{F^r\}$  the reaction load vector and  $\{F^a\}$  the total applied load vector, defined by:

$$\{F^a\} = \{F^{nd}\} + \{F^{ac}\} + \sum_{m=1}^N \{F_e^{th}\} + \{F_e^{pr}\} \quad (2.18)$$

where  $\{F^{nd}\}$  is the applied nodal load vector,  $\{F^{ac}\} = -[M]\{a_c\}$  the acceleration load vector,  $[M] = \sum_{m=1}^N [M_e]$  the total mass matrix,  $[M_e]$  the element mass matrix,  $\{a_c\}$  the total acceleration vector,  $\{F_e^{th}\}$  and  $\{F_e^{pr}\}$  respectively the element thermal and pressure load vectors. The Newton-Raphson procedure is used to solve the equations. PARLARE DEL METODO DELLE TANGENTI OPPURE NO?

### 2.2.2 Modal analysis

A free-vibration modal analysis is used in order to determine the vibration characteristics, i.e. natural frequencies and mode shapes, in structures. It can also be, as it will be shown, a starting point for another, more detailed, transient dynamic analysis.

Modal analysis performed in the present work are characterized by the following assumptions and restrictions:

1. the structure has constant stiffness and mass effects;
2. there is no damping;
3. the structure has no time varying forces, displacements, pressures or temperatures (*free vibration*).

For an undamped system, the equation of motion expressed in matrix notation is:

$$[M]\{\ddot{u}\} + [K]\{u\} = \{0\} \quad (2.19)$$

where  $\{\ddot{u}\}$  the nodal acceleration vector (the remaining terms have already been discussed). For a linear system, free vibration will be harmonic of the form:

$$\{u\} = \{\phi\}_i \cos \omega_i t \quad (2.20)$$

where  $\{\phi\}_i$  is the eigenvector representing the mode shape of the  $i$ -th natural frequency,  $\omega_i$  the  $i$ -th natural circular frequency and  $t$  the time. Substituting the equation (2.20), the equation (2.19) becomes:

$$(-\omega_i^2[M] + [K])\{\phi\}_i = \{0\} \quad (2.21)$$

This equation is satisfied if either  $\{\phi\}_i = \{0\}$  or if the determinant of  $([K] - \omega_i^2[M])$  is null. Since the first solution is trivial, the second one gives the solution:

$$|[K] - \omega_i^2[M]| = 0 \quad (2.22)$$

This is an eigenvalue problem which may be solved for up to  $n$  (number of DOFs) values of  $\omega^2$  and  $n$  eigenvectors  $\{\phi\}_i$  which satisfy the equation (2.21).

The eigenvalue and eigenvector extraction is performed through the *Block Lanczos* method, usually applied for large symmetric eigenvalue problems.

### 2.2.3 Nodal diameters and engine order excitation

Ideal, tuned bladed disks have identical blades. Defining a sector as one blade plus the corresponding segment of the disk, the bladed disk will be composed of  $N$  identical sectors (where  $N$  is the number of blades). In this way the structure has a *cyclic symmetry*.

The *nodal diameter* concept is related to the appearance of the bladed disk when it vibrates in a certain mode. Mode shapes contain lines of null displacement crossing the entire disk, as shown schematically in Fig. 2.3, where the number of nodal diameters changes from 0 to 2. Sometimes, especially for complicated structures at high frequencies, lines of zero displacements may be not clearly observable in the mode shape. In this way, mode shapes are often classified by the number of nodal diameters, thus the first mode shape will be characterized by one zero displacement line across the bladed disk, and so on. Natural frequencies and mode shapes for each nodal diameter are obtained by solving the equation (2.21). The total number of nodal diameters/mode shapes depends on the blade number  $N$ :

$$k_{max} = \frac{N}{2} \quad \text{for even } N \quad (2.23)$$

$$k_{max} = \frac{N-1}{2} \quad \text{for odd } N \quad (2.24)$$

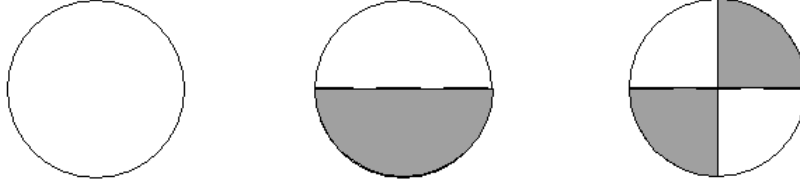


Figure 2.3: Examples of nodal diameters

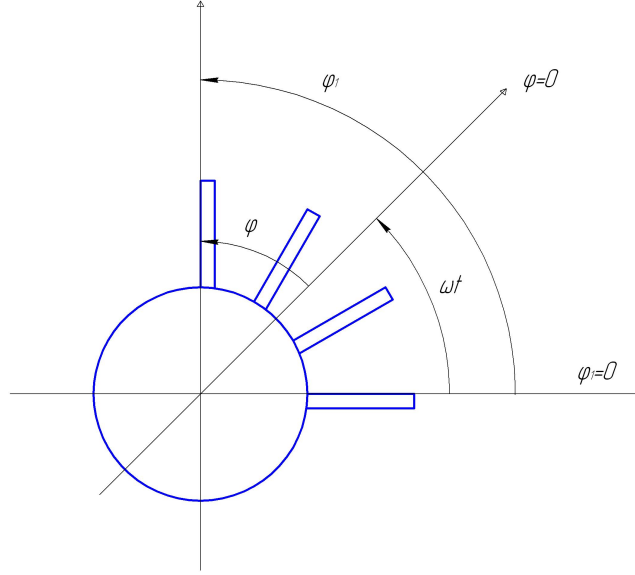


Figure 2.4: Motionless and rotating coordinate systems

A concept which is strictly related to mode shapes is that of the *engine order excitation*. It is related to the amount of flow distortions per revolution and its index assumes values from 0 to  $k_{max}$ . That is because the flow which passes through the engine is non-uniform. Therefore the gas force  $F$  acting on the blade experiences some obstructions, both up-stream and down-stream. Because  $F$  changes periodically, it can be represented as a Fourier series:

$$F = \sum_{k=0}^{k_{max}} f \cos(k\varphi_1 - \Psi) \quad (2.25)$$

where  $f$  is the gas force amplitude,  $k$  is the Engine Order (EO) index,  $\varphi_1$  is the blade position in a motionless coordinate system and  $\Psi$  an eventual initial phase angle.  $\varphi_1$  can be expressed in a coordinate systems which rotates with the disk (Fig. 2.4):

$$\varphi = \varphi_1 - \omega t \quad \Rightarrow \quad \varphi_1 = \varphi + \omega t$$

Any part of the series (2.26), neglecting the initial phase angle, can be expressed as:

$$\tilde{F} = f \cos(k\varphi + k\omega t) = f \cos(k\varphi + \omega_k t) \quad (2.26)$$

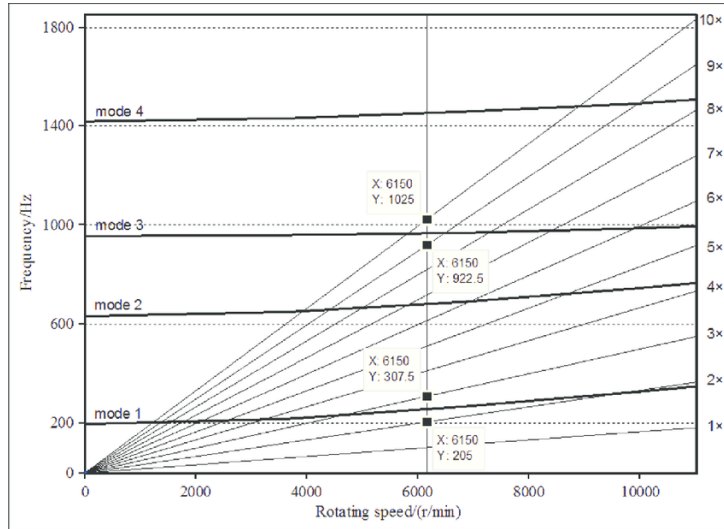


Figure 2.5: An example of Campbell diagram showing the relationship between natural frequencies, rotational speed and engine orders of the excitation (radial lines)

Thus any part of the series depends on blade position  $\varphi$  and on time and can excite vibration. This equation represents a back running travelling wave of amplitude  $f$  traveling in the negative direction (descending blade number). The frequency  $\omega_k$  of the harmonics depends linearly with the rotating speed  $\Omega$ :

$$\omega_k = k\Omega \quad (2.27)$$

Generally first harmonics have high vibration amplitudes and it reduces as EO increases.

## 2.2.4 The resonance diagram

Rotating machines, such as compressors, run at high rotating speed under actual operating condition. The centrifugal force generated by high speed rotation increases the stiffness of the bladed disk. Thus an important relation do exists between natural frequencies and rotating speed.

It is convenient to express the vibration characteristics of a rotating bladed disk in a resonance diagram, also called *Campbell diagram*. It represents two kind of curves: the dependency of natural frequencies of the bladed wheel and the frequencies of exciting harmonics as functions of the rotational speed. Regarding the first one, for a compressor disk, natural frequencies usually increase with rotational velocity. While, as already said in the previous paragraph, the frequency of the exciting harmonics depends linearly on the rotating speed. In this way, it is possible to draw the  $k$ -th EO lines for  $1 \leq k \leq 13$ .

To detect the possible *resonant points* is necessary to superpose on the graph the EO lines and find intersection points between the  $k$ -th EO line and the curve of natural frequencies characterised by the same nodal diameter. At these speeds (called *critical speeds*), where intersections exist, resonance takes place. However, only at enduring critical speed over time dangerous resonance arise. Dangerous vibration has no time to develop if the engine quickly surpasses these velocities.

An example of resonant diagram is shown in Fig. 2.5. Usually the first EOs are the most dangerous. In fact, as predictable, only EO lines with low angular coefficient can intersect the rotor frequency curve in regions inside the rotational speed range of the engine.

### 2.2.5 Transient dynamic analysis

A transient dynamic analysis is a technique used to determine the dynamic response of a system under the action of any time-dependent loads, such as the harmonic aerodynamic force acting on the compressor blades. It can be used to determine the time-varying displacements, strains, stresses and forces in the structure. The basic equation of motion solved by a transient dynamic analysis is:

$$[M]\{\ddot{u}\} + [C]\{\dot{u}\} + [K]\{u\} = \{F^a(t)\} \quad (2.28)$$

where  $[C]$  is the structural damping matrix,  $\{\dot{u}\}$  the nodal velocity vector and  $\{F^a(t)\}$  the applied load vector (the other terms have already been defined). The *ANSYS* program uses the Newmark time integration method to solve these equations at discrete timepoints and it is one of the most popular time integration methods as a single step algorithm. The semi-discrete equation of motion 2.28 can be rewritten as:

$$[M]\{\ddot{u}_{n+1}\} + [C]\{\dot{u}_{n+1}\} + [K]\{u_{n+1}\} = \{F_{n+1}^a(t)\} \quad (2.29)$$

where  $\{\dot{u}_{n+1}\}$  can be thought as the nodal acceleration vector  $\{\ddot{u}(t_{n+1})\}$  at time  $t_{n+1}$  and analogously for the other terms. In addition to equation 2.29, the Newmark method require displacement and velocity to be updated as follows:

$$\{\dot{u}_{n+1}\} = \{\dot{u}_n\} + [(1 - \delta)\{\ddot{u}_{n+1}\} + \delta\{\ddot{u}_n\}]\Delta t \quad (2.30)$$

$$\{u_{n+1}\} = \{u_n\} + \{\dot{u}_n\}\Delta t + [(\frac{1}{2} - \alpha)\{\ddot{u}_n\} + \alpha\{\ddot{u}_{n+1}\}]\Delta t^2 \quad (2.31)$$

where  $\alpha$  and  $\delta$  are Newmark's integration parameters. The Newmark integration scheme consists of the three finite difference equations 2.29, 2.30 and 2.31 with three unknowns  $\{u_{n+1}\}$ ,  $\{\dot{u}_{n+1}\}$  and  $\{\ddot{u}_{n+1}\}$  which can be numerically calculated from initial known quantities  $\{u_n\}$ ,  $\{\dot{u}_n\}$  and  $\{\ddot{u}_n\}$ . In practical terms, by making use of the previous three equations, a single step time integrator can be written as:

$$(a_0[M + a_1[C] + [K])\{u_{n+1}\} = \{F_{n+1}^a(t)\} + [M](a_0\{u_n\} + a_1\{\dot{u}_n\} + a_2\{\ddot{u}_n\} + [C](a_3\{u_{n+1}\} + a_4\{\dot{u}_n\} + a_5\{\ddot{u}_n\)) \quad (2.32)$$

where

$$\begin{aligned} a_0 &= \frac{1}{\alpha\Delta t^2} & a_1 &= \frac{\delta}{\alpha\Delta t} & a_2 &= \frac{1}{\alpha\Delta t} & a_3 &= \frac{1}{2\alpha} - 1 \\ a_4 &= \frac{\delta}{\alpha} - 1 & a_5 &= \frac{1}{2\alpha} - 1 & a_6 &= \Delta t(\frac{\delta}{2} - 2) & a_7 &= \delta\Delta t \end{aligned}$$

At first, the unknown  $\{u_{n+1}\}$  is calculated. Then, the program calculates also the two unknowns  $\{\dot{u}_{n+1}\}$  and  $\{\ddot{u}_{n+1}\}$  by using the following equations:

$$\{\dot{u}_{n+1}\} = a_1(\{u_{n+1}\} - \{u_n\}) - a_4\{\dot{u}_n\} - a_5\{\ddot{u}_n\} \quad (2.33)$$

$$\{\ddot{u}_{n+1}\} = a_0(\{u_{n+1}\} - \{u_n\}) - a_2\{\dot{u}_n\} - a_3\{\ddot{u}_n\} \quad (2.34)$$

As will be explained in the next paragraph, choosing an appropriate time integration scheme for the finite element semi-discrete equation of motion 2.28 is a key point in terms of solution accuracy, stability and dissipation. In the Newmark method, the amount of numerical dissipation is controlled by the two parameters seen in equations 2.29 and 2.30. Newmark integration method is considered unconditionally stable if these parameters satisfy the following conditions:

$$\delta \geq \frac{1}{2} \quad \alpha \geq \frac{1}{4} \left( \frac{1}{2} + \delta \right)^2 \quad (2.35)$$

### 2.2.6 Guidelines for Integration Step Size

The accuracy of a transient dynamic solution depends on the integration time step: the smaller the time step, the higher the accuracy. In fact, a time step that is too large introduces an error that affects the system response. On the other hand, a time step that is too small wastes computer resources. The optimum time step size depends on the frequency of the system. Since the dynamic response of a structure can be thought as a combination of modes, the time step should be able to deal with the highest frequency of the selected mode that contributes to the response. The solver then calculates an aggregate response at every time point. A general rule of thumb is to use a minimum of twenty points per cycle at the response frequency. That is, if  $\Omega$  is the rotating frequency of the system, the Initial Time Step (ITS) is given by:

$$ITS = \frac{1}{20 \cdot \Omega} \quad (2.36)$$

Smaller ITS can be applied if accurate results are needed.

# Chapter 3

## Numerical model of the bladed disk

### 3.1 Introduction

Since this study will be divided into two main parts by using two different softwares, it is necessary to generate two 3D models:

- a simplified 3D model created in *Numeca* used for the CFD analysis;
- a realistic 3D model which will be used for the modal and transient analysis in *ANSYS* ambient.

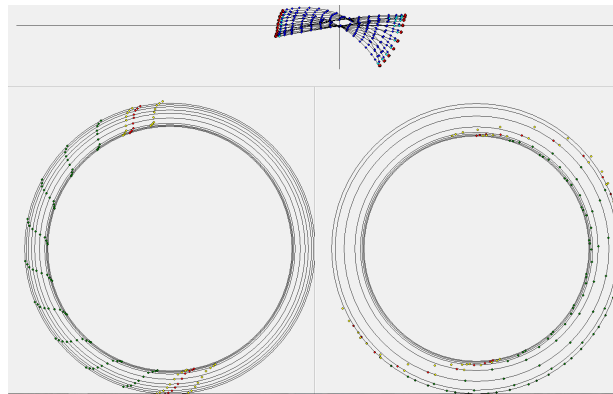
### 3.2 Creation of model for CFD analysis

The *Numeca* application which allows the creation of a simplified geometric model is *Autogrid5*<sup>TM</sup>. In this ambient it is needed to load the blades as a .geomTurbo file (which is a text file) generated through a profiler. Simply by opening the .txt file with the blade coordinates, the profiler automatically generates the blade (Fig. 3.1a) and it is possible to save it in the format required. Besides the blades, it is also necessary to create the 3D model of the flow pass section. Once given its coordinates in one cross section, it is enough to save them as a .dat file. Now that the required files are ready, in the *Autogrid5* interface is imported the flow path section (Fig. 3.1b) and then the upper side is linked to the *Shroud* and the lower side is linked to the *Hub*. After that, the rows of blades can be loaded. In order to calculate the fluid force acting on the first rotor blades, all the three stages are loaded in the model (Fig. 3.2).

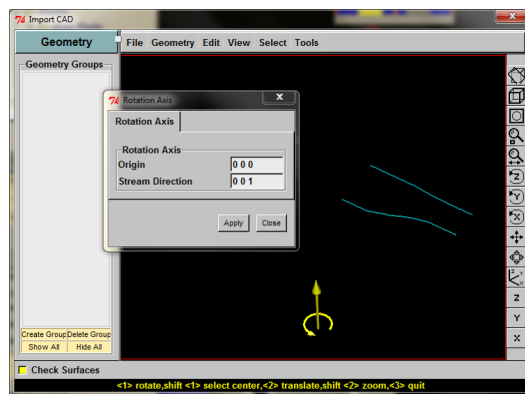
#### 3.2.1 Mesh parameters

This step is one of the most important of the entire analysis. In fact the decisions made at this stage will profoundly affect the accuracy and economy of the analysis. Using a mesh of adequate geometrical quality is an important part of controlling discretization error. It is also important for avoiding round-off errors during, for example, the solution of the linear equations that are produced by the discretization process. For the mesh quality optimization purpose, several types of meshes will be generated. Along the height of the flow passage it is analyzed the influence of 3 main parameters:

- Expansion Ratio (ER)



(a) Generation of .geomTurbo file through the Profiler



(b) Generation of the flow path

Figure 3.1: Blades and flow path definition

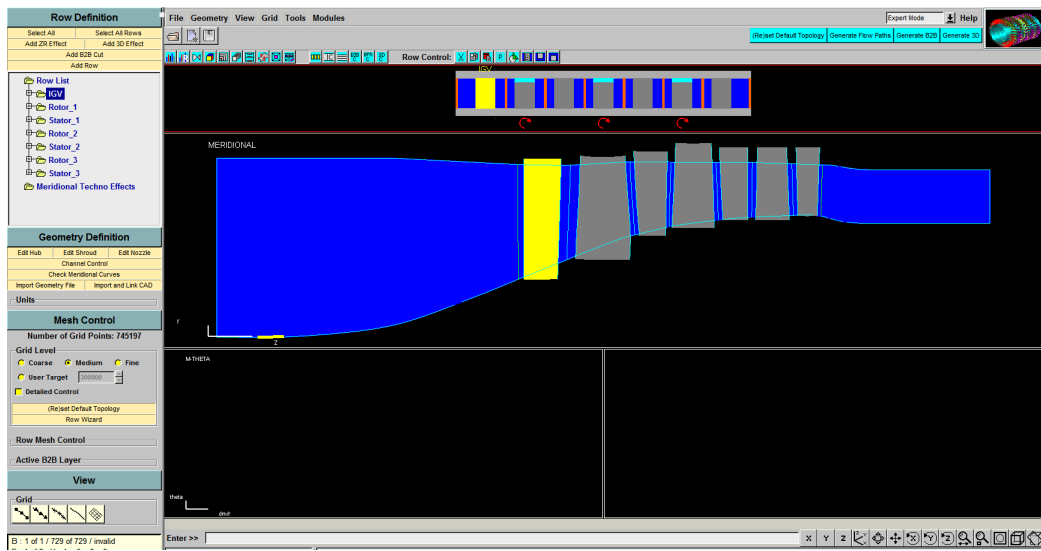


Figure 3.2: Compressor stages definition

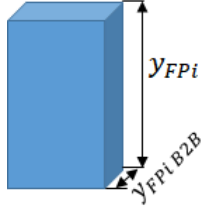


Figure 3.3: Cell representation

- Aspect Ratio (AR)
- First cell width at the solid wall  $y^+$

The concept of *Expansion Ratio* is relative to the rate of change in the magnitude of adjacent element face areas (volumes in 3D mesh). It can be defined as following:

$$ER = \frac{y_{FPi}}{y_{FPi-1}} \quad (3.1)$$

where  $y_{FPi}$  represents the height of the  $i$ -th element (Fig. 3.3). This parameter directly influences the numerical error of the solution. Its range should be between 1 and 1,5 usually.

The concept of mesh *Maximum Aspect Ratio* (sometimes referred as *MR*) relates to the degree that mesh elements are stretched. The maximum AR should be around 1000 to have a good mesh quality. It is defined by the following equation:

$$AR_{max} = MR = \frac{y_{max}}{y_{min}} \quad (3.2)$$

where  $y_{max}$  and  $y_{min}$  represents the maximum and minimum value of the height or widthness Blade-to-Blade (B2B) of the cell. The term Blade-to-Blade refers to the single layer mesh, in a orthogonal plane to the flow passage.

The dimensionless wall distance  $y^+$  can be defined in the following way:

$$y^+ = \frac{u_* y}{\nu} \quad (3.3)$$

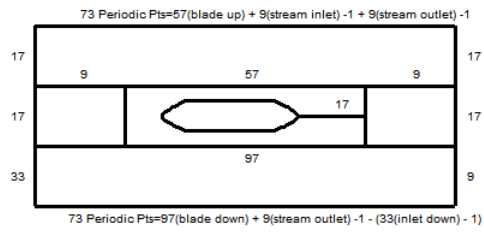
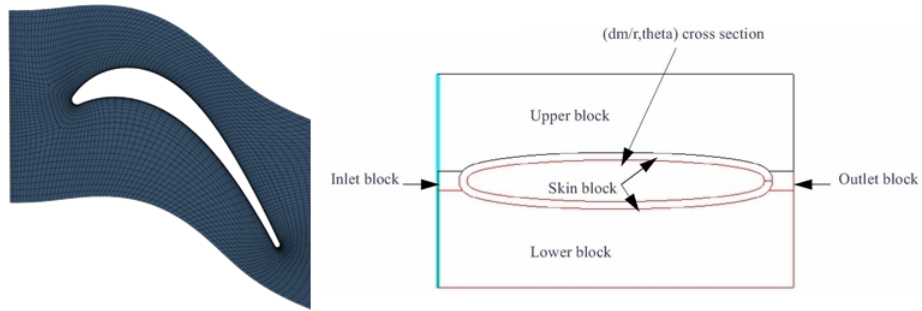
where  $u_*$  is the friction velocity at the nearest wall,  $y$  is the distance to the nearest wall and  $\nu$  is the local kinematic viscosity of the fluid. In *Autogrid5* is not possible to select  $y^+$ , so it is necessary to calculate the real wall distance  $y$ .

In the same way will be investigated the influence of other mesh parameters in the B2B distribution.

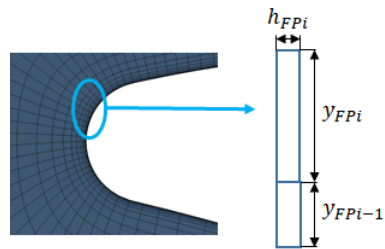
It is studied the influence of the following parameters:

- Mesh density;
- *O-layer*;
- B2B Expansion Ratio ( $ER_{B2B}$ )

The first item regards the number of mesh elements in the  $L$  and  $H$  blocks (Fig. 3.4a). Then the influence of the number of elements in the *O-layer* will be investigated. Finally the influence of the ER in Blade-to-Blade configuration. The  $ER_{B2B}$  can be defined in the same way of the  $ER$  related to the flow path (Fig. 3.4b).



(a) *B2B topological blocks in Autogrid 5*



(b) *ER\_{B2B} graphic representation*

Figure 3.4: B2B mesh parameters visualization

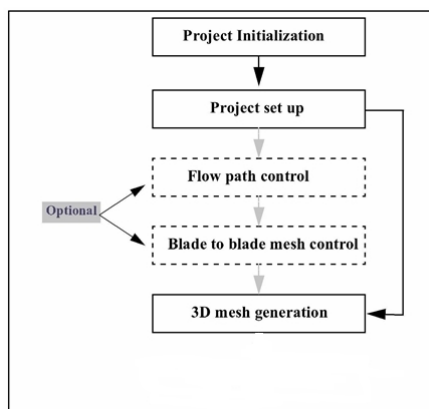


Figure 3.5: Mesh generation steps

The mesh generation of a turbomachinery configuration is divided into 6 main steps, which can be seen in Fig. 3.5 [7].

The first step has already been completed with the geometry definition of the compressor section. The model has been initialized both manually (the external CAD file of the flow path) and automatically (the .geomTurbo file of the compressor rows).

In Appendix A, Figs. A.1 and A.2 display the different meshes created for the model changing in FP parameters, while Figs. A.3 and A.4 show changing in B2B parameters. Cells highlighted in green indicate the varying parameter in question while yellow rows highlight the chosen parameter setting based on the analysis of the next chapter.

### 3.2.2 Project setup

The project setup can also be divided into 3 steps:

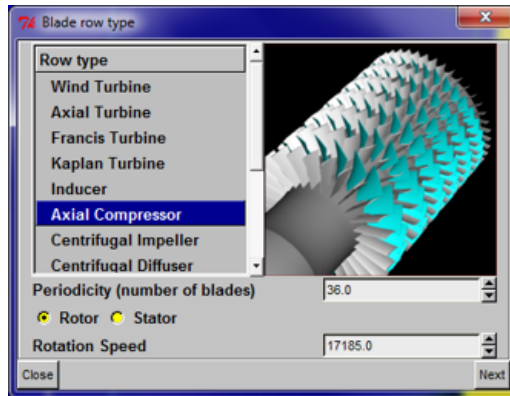
1. Geometry and Configuration definition;
2. Global parameters settings;
3. B2B topology definition.

The first one is necessary only if the project is initialized from external CAD file. In this case it is not needed because the flow path doesn't require the *Row Definition*.

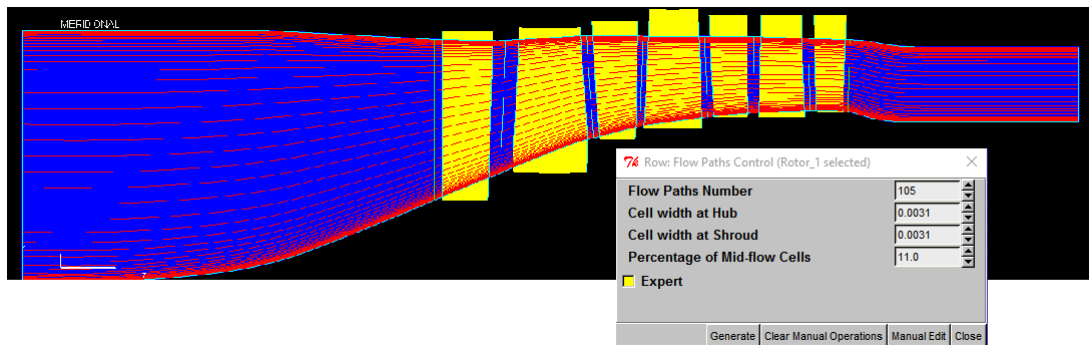
The Global parameters settings concern the definition of the periodicity for each row, the rotation speed (although this information will be not used by the grid generation process), the shroud and hub gap and the first cell width at the solid wall. This step needs to be done for each row through the feature *Row Wizard*. In fig. 3.6a is illustrated the procedure referred to the first rotor. In the last window, besides the *Wall Cell Width*, it can be selected the *Spanwise Grid Point Number*. Choosing it at this step, allows the system to predict the *Spanwise Expansion Ratio*.

### 3.2.3 Flow paths control

At this step it is possible to adjust the mesh in the flow path level. As seen in Fig. 3.6b, the *Flow Paths Number* and the *Percentage of Mid-flow Cells* (which is the percentage of cells in



(a) Global parameters settings



(b) Flow path generation and control

Figure 3.6: Flow path and stages settings

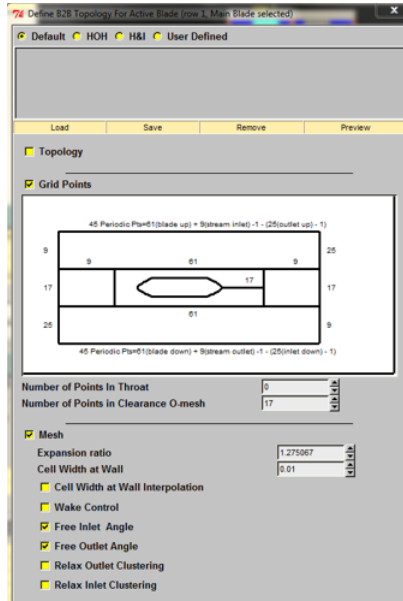


Figure 3.7: B2B Mesh Control Box

the region away from the walls) can be choosed. These two features will profoundly affect the values of  $ER$  and  $AR$ .

### 3.2.4 Blade to Blade control

The 3D row meshes generated with *AutoGrid5* are obtained by stacking blade to blade meshes created in the  $(dm/r, \theta)$  space. Each blade to blade mesh is related to a flow path. A blade to blade mesh is generated in two steps:

1. Conformal mapping;
2. B2B topology optimization.

Regarding the first step, the flow paths defined in the meridional space are used to create surfaces of revolution named layers. These surfaces are intersected by the blades definition to obtain 3D sections projected into the  $(dm/r, \theta)$  space. The projection, named *conformal mapping*, preserves the angles and ensures reciprocity of the distances.

In the second step, it is necessary to set the B2B topology. As it can be seen in fig. 3.4, the B2B topology is composed by 5 blocks. The inlet, outlet, upper and lower blocks use a H-topology. The skin block around the blade uses a O-topology. Fig. 3.7 shows the *B2B Mesh Control Box* in which it is possible to set the number of mesh elements for each block. In this box is also possible to set the  $ER$  related to the B2B level. The blade to blade view is used to display and control the quality of the blade to blade mesh of the rows.

### 3.2.5 3D mesh generation and mesh optimization

The 3D mesh generation of the active blade rows is performed through the button *Generate 3D*. Then the 3D mesh is automatically computed and displayed in the 3D view. A mesh quality report is also displayed.

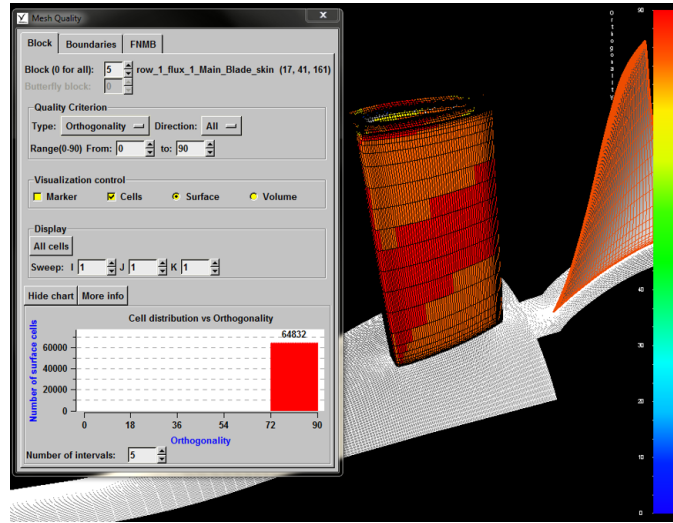


Figure 3.8: 3D mesh view and Grid quality box

Once generated the 3D mesh, it is necessary to check that the above mesh parameters fall within the required ranges. It is necessary to select the row in question and then open the *Grid Quality Box* in which is possible to check parameters like Aspect Ratio and Expansion Ratio (Fig. 3.8).

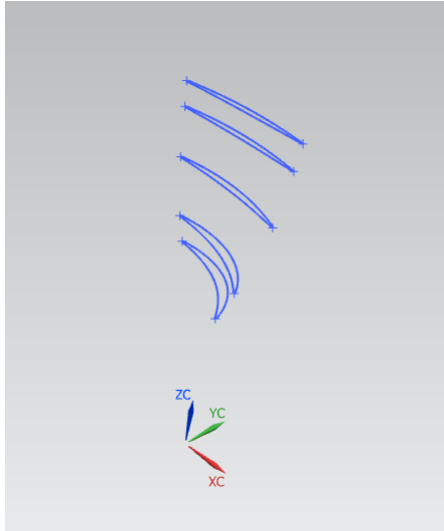
As already said, different meshe files with changing parameters will be created and then used for the CFD computation in order to choose the “best” mesh that will give results as close as possible to experimental curves and data. For this aim, this preliminary study will be conducted over a simpler compressor stage model, called *Stage 37*. Blade and flow passage coordinates and overall performances of this compressor stage can be found in [9]. After analyzing and comparing the results of the simulations with these experimental data, the mesh that will give closest results to the experimental curves will be chosen. Results and discrepancies with the NASA’s paper will be shown in the next chapter.

### 3.3 Creation of 3D model for ANSYS Mechanical simulations

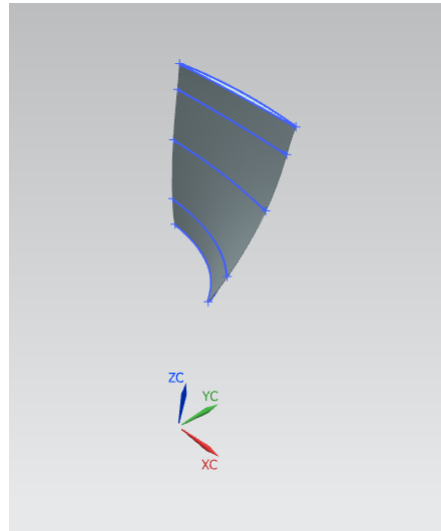
The first step of the second part of the work is to generate a 3D model with a medium-high level of details in comparison to the the real compressor rotor stage. Blades and shrouds are created by using the coordinates  $x, y, z$  given in Figs. B.2 and B.1 in Appendix B, where the  $x$  axis is parallel to the engine longitudinal axis,  $z$  is radial and  $y$  is perpendicular to them. The coordinates of each section are then copied in a \*.dat file, which is loaded in a new sketch in *NX* through the feature *Spline from points* (Fig. 3.9a). Once all the sections are loaded it is possible to create the blade surface by means of the function *Mesh Surface Through Curves* (Fig. 3.9b).

The next step is to add the shroud and the fir-tree basement. Regarding the shroud, the best way is to use the previous feature *Spline from points* and then use the command *Revolve* around the engine axis (Fig. 3.9c). Finally, the basement is extruded starting from a sketch in the vertical plane (Fig. 3.9d).

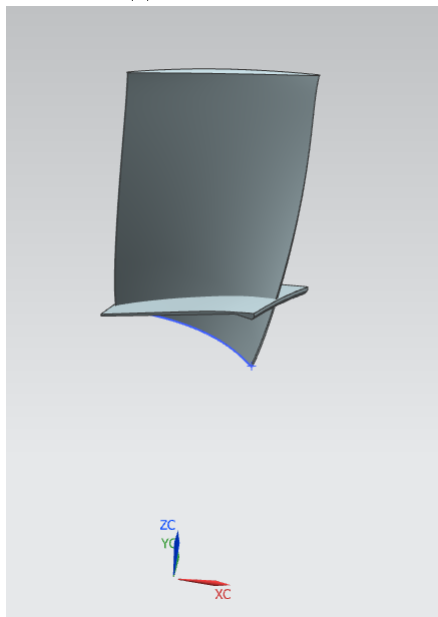
In order to simplify the model and to reduce the calculation time all the little radiuses and



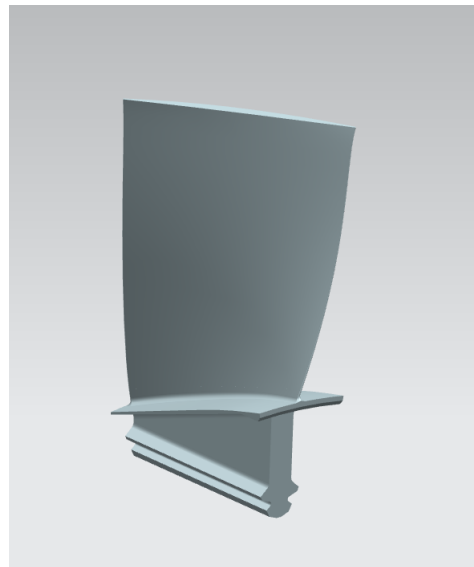
(a) *Splines from points*



(b) *Mesh surface through curves*



(c) *Shroud*



(d) *Completed blade*

Figure 3.9: Blade modelling

Table 3.1: Disk geometrical characteristics

Inner radius	40	mm
Outer radius	240	mm
Width @ inner radius	60	mm
Width @ outer radius	130	mm
Number of blades	27	

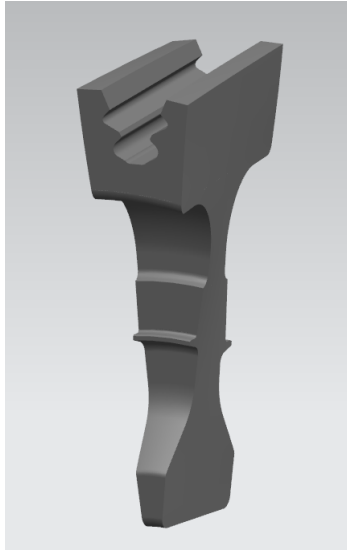
blends are neglected.

The disk of the first stage is modelled starting from a disk sector (Fig. 3.10a). The main characteristics of the disk are listed in Tab. 3.1.

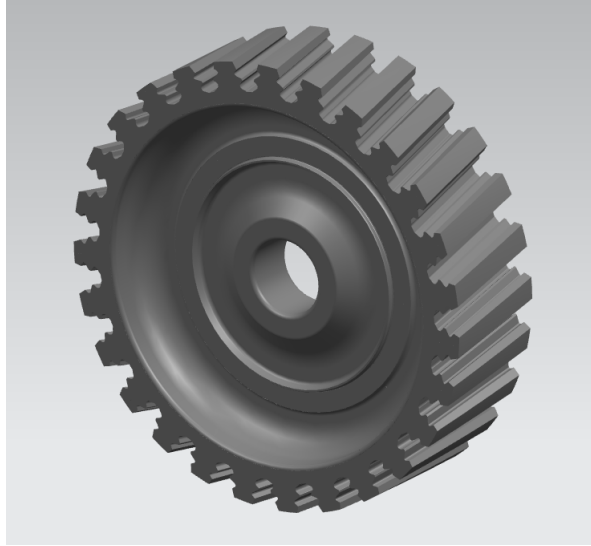
The whole disk can be constructed just by using the feature *Circular pattern* around the engine longitudinal axis (Fig. 3.10b).

Also during disk modelling, all little radiuses, champhers, blends, holes and shrouds are neglected because otherwise the 3D model would be too complex and the simulations would take too much time to solve.

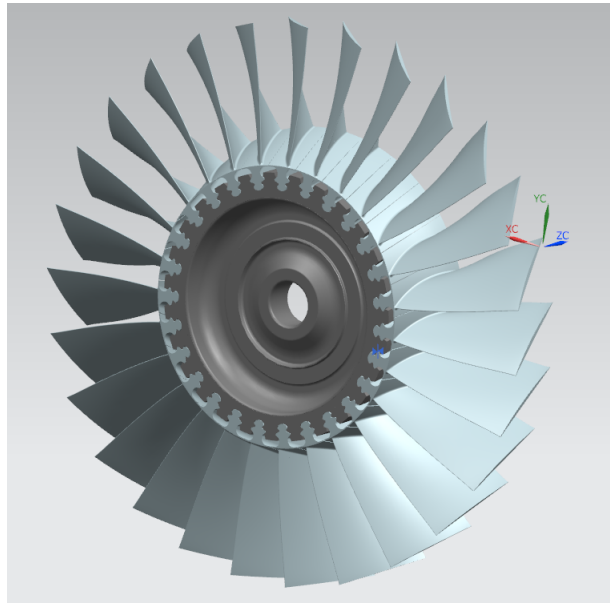
Once created the blade and the disk, the following step is simply to create an *Assembly* in which it is needed to load them and then apply the constraints between blade and disk. It is enough to align the blade longitudinal axis with the disk axis and then to block the axial displacement of the blades along the disk slots. The final assembly can be seen in Fig. ??c.



(a) *Disk sector*



(b) *Disk*



(c) *Bladed wheel*

Figure 3.10: Disk modelling

## Chapter 4

# CFD analysis. Defining of the excitation force

### 4.1 Introduction

In order to calculate the exciting force of the flow acting on the compressor blades it is needed a Computational Fluid Dynamics (CFD) analysis. It consists of the following steps:

- *Pre-Processing*: discretization of the domain
- *Solver*: settings and flow computation
- *Post-Processing*: analysis of the results

The first step of the CFD simulation process has already been completed in the previous chapter. It includes the identification of the fluid domain of interest. This domain is then further divided into smaller elements which represents the mesh.

Once the problem has been identified and discretized, it is possible to set the fluid material properties, the flow physical model and the boundary conditions.

The post-processing step regards the analyzation of the results by using plots, streamlines, and data curve.

To perform these steps NUMECA has developed three software systems. The first one, *Autogrid5<sup>TM</sup>*, has been widely examined previously. The second software system, the *FINE<sup>TM</sup>/Turbo* solver, is a state of the art 3D multiblock flow solver able to simulate Euler or Navier-Stokes (laminar or turbulent) flows. The third one, *CFView<sup>TM</sup>*, is a highly interactive Computational Field Visualization (CFV) system. Detailed discussions about the second and third steps follow.

### 4.2 Settings and flow simulation solver

The first step is to create a new project in the *FINE/Turbo* interface, loading the *.trb Grid file* generated through *Autogrid5*. Once changed the units in millimeters, according to the grid file, the project is ready to be set. The setting of all the parameters required for the simulation project regards the following items:

- Fluid model

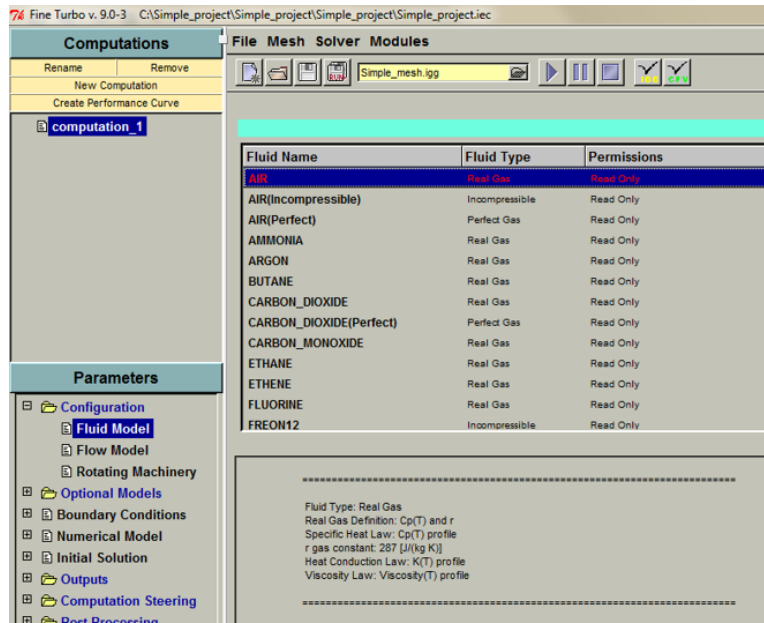


Figure 4.1: Fluid selection window

- Flow model
- Rotating machinery
- Boundary conditions
- Numerical model
- Initial solution
- Outputs
- Computation steering

In the next paragraphs each step is described in details.

#### 4.2.1 Fluid model

The first window we have to interact with is the one of the fluid model parameters (Fig. 4.1). In this window is possible to select a fluid from the fluid database. Since the engine is designed to work only with air, it is enough to select it from the list of pre-defined fluids. By opening the *Show Fluid Properties* window the heat capacity, heat conductivity and dynamic viscosity are plotted as a function of temperature.

#### 4.2.2 Flow model

The flow model page can be used in order to specify several characteristics of the flow:

- the time configuration to define time dependence of the equation to solve

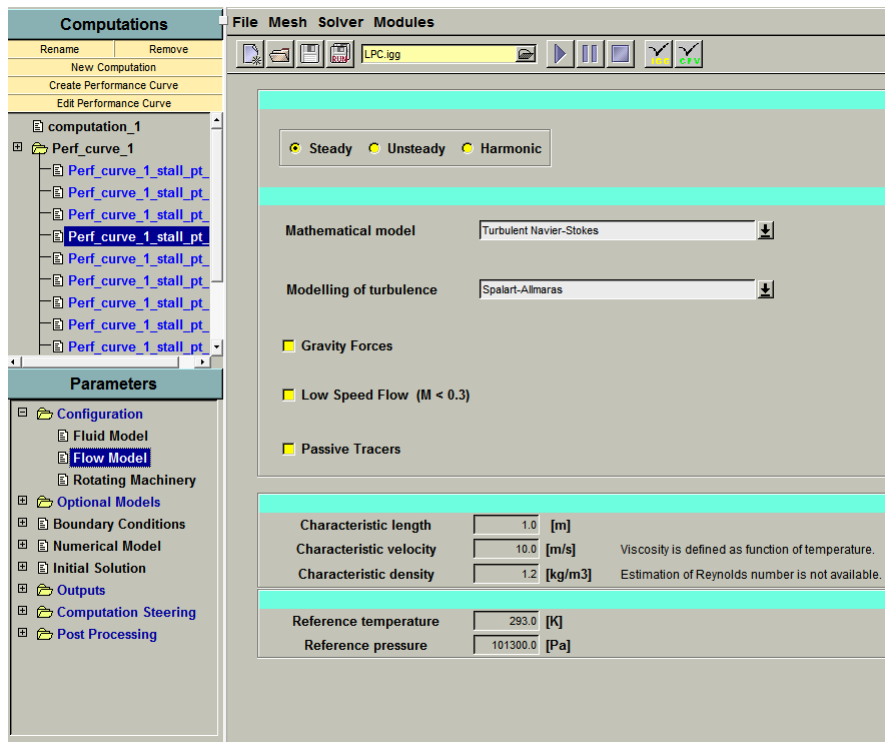


Figure 4.2: Flow model page

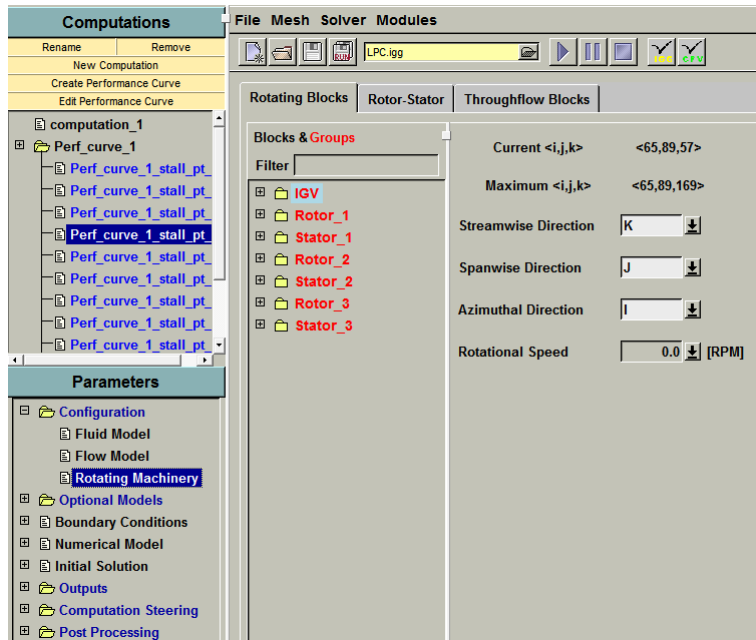
- the mathematical model to:
  - choose between viscous and non-viscous flow
  - choose between laminar and turbulent flow
  - activate gravity
  - activate pre-conditioning for low speed flow
- the characteristic scales which define the Reynolds number of the flow
- the reference values of temperature and pressure in the flow

Fig. 4.2 shows how the flow model parameters are setted. The computation that will be performed is time independant, therefore it is sufficient to select *Steady* in the *Time Configuration* tab. Is then time to select the appropriate mathematical model, according to what said in the second chapter. Gravity force is not needed in the present project.

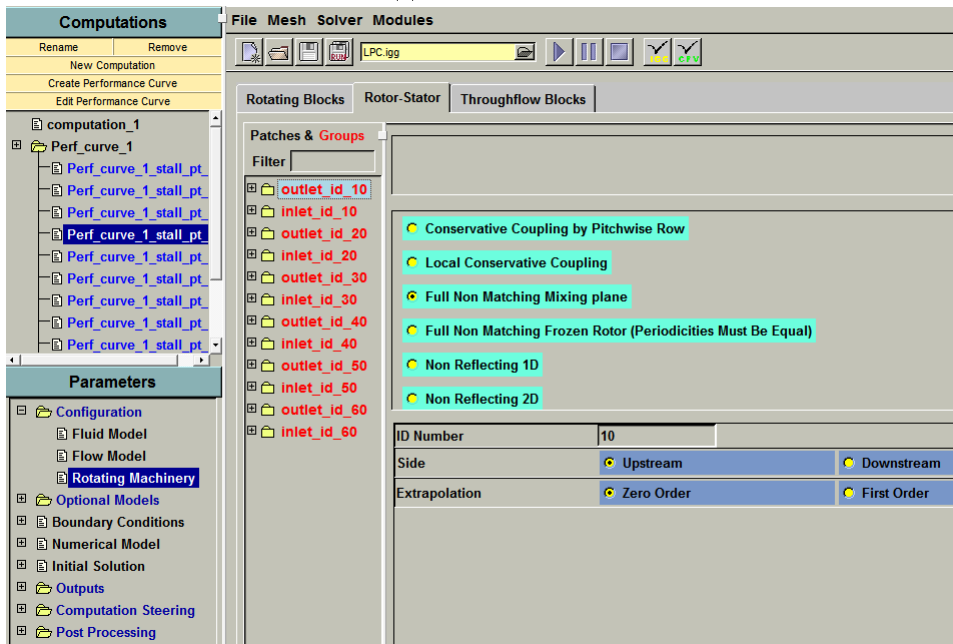
### 4.2.3 Rotating machinery

In this page dedicated turbomachinery models can be setted.

The *Rotating Blocks* tab gives access to the definition of the typical information for each block created by the grid generator (Fig. 4.3a). On the left is displayed the list of all the blocks, which are grouped per row. Whereas on the right side of the window, the information for each row is given. For the selected row are shown the current and maximum number of nodes in the



(a) Rotating blocks



(b) Rotor/stator interfaces

Figure 4.3: Rotating machinery page

three grid directions. Then it is needed to set the streamwise, spanwise and azimuthal directions, which allow to determine the block orientation. Since *Autogrid5* was used for the grid generation, the three directions are automatically setted. For the rotating blocks is then necessary to set the rotational speed in Revolutions Per Minute (RPM). The software solves the equations in a relative frame of reference, so also mesh blocks which surround the rotating blades rotate with them too. A positive value for the rotational speed indicates a rotation in positive  $\theta$  direction according to a right handed coordinate system.

Fig. 4.3b shows the *Rotor-Stator* interface definition page in steady mode. On the left side the rotor/stator interfaces indicated through an *ID Number* are listed. For each of them is necessary to specify if the interface is on the *Upstream* or *Downstream* side. A zero order of extrapolation is enough for this type of calculations. Furthermore in this tab is necessary to choose the *Full Non Matching Mixing Plane* boundary condition for the rotor/stator interface, according to what said in the paragraph 2.1.5.

#### 4.2.4 Boundary conditions

The importance of imposing realistic and proper boundary conditions can not be underestimated. Indeed, the imposition of wrong boundary conditions can cause the divergence of the CFD simulation or, worse, calculate unreliable results even if the solution converges.

During the grid generation process in *Autogrid5* ambient, some boundary conditions have already been imposed. However, all necessary boundary conditions will be set in *FINE/Turbo* interface too. Five tabs are available, which correspond to five types of boundary conditions:

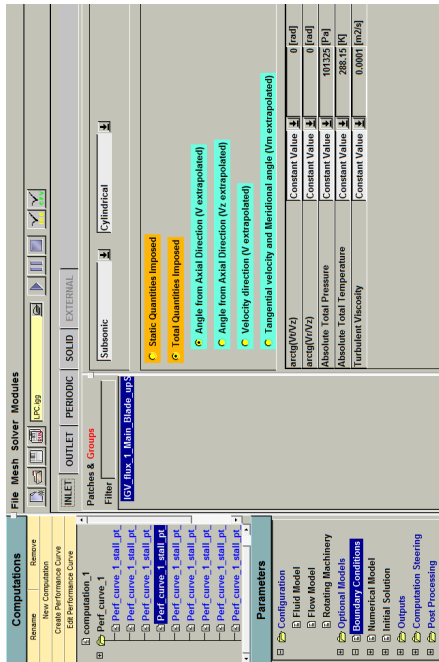
- *Inlet*
- *Outlet*
- *Periodic*
- *Solid*
- *External*

Each page of the five boundary conditions is splitted into two areas, as usual. The left area contains the list of the different patches that are of the boundary condition type of the selected tab. In the right area is possible to specify the boundary condition parameters.

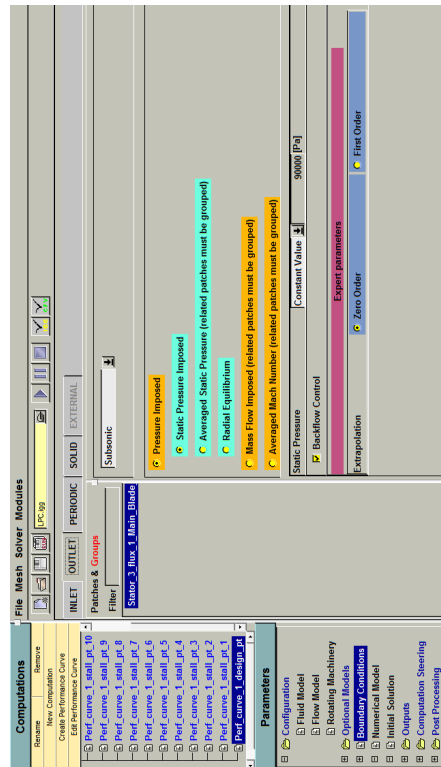
Fig. 4.4a shows the *Inlet Boundary Condition* page. On the top of this page is possible to select the configuration type of the project between Cartesian or cylindrical. Furthermore there are two categories of inlet condition: *Supersonic* or *Subsonic*, with the latter that is chosen for this project. In the lower part of the page are displayed input boxes for the physical variables required to fully determine the boundary condition. Among the eight major types of inlet boundary conditions available, *Total Quantities Imposed* is chosen. In the variables input boxes is necessary to set the total pressure, the total temperature and the flow direction.

In Fig. 4.4b is shown the *Outlet Condition*. In the upper part of the page is necessary to set a *Subsonic* outlet. Five types of subsonic outlet boundary condition are available and the *Pressure Imposed* one is set. In the latter condition, three different methods are selectable: *Static Pressure Imposed*, *Averaged Static Pressure* and *Radial Equilibrium*. Among these, the first one is selected. In this way the static pressure is imposed on the boundary, the static temperature and the absolute velocity components are extrapolated.

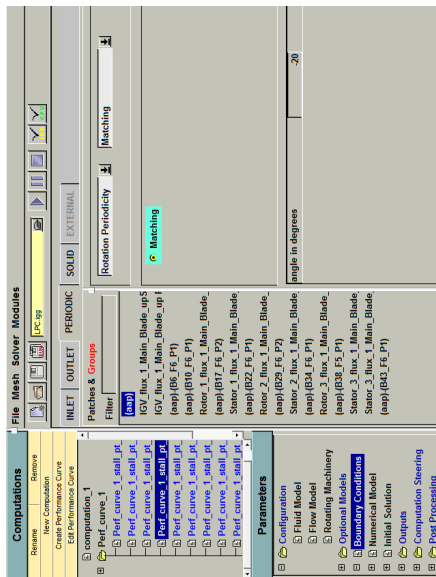
The third tab available is the *Periodic Condition* (Fig. 4.4c). The advantage of the *Autogrid5* mesh generator concerns the automatic establishment of all periodic boundary conditions. In



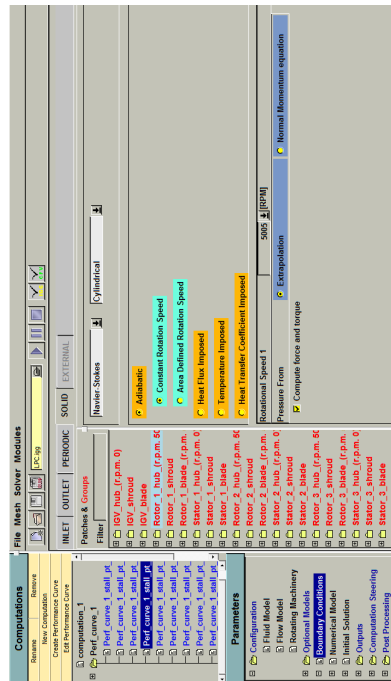
(a) Inlet tab



(b) Outlet tab



(c) Periodic tab



(d) Solid wall tab

Figure 4.4: Boundary conditions page

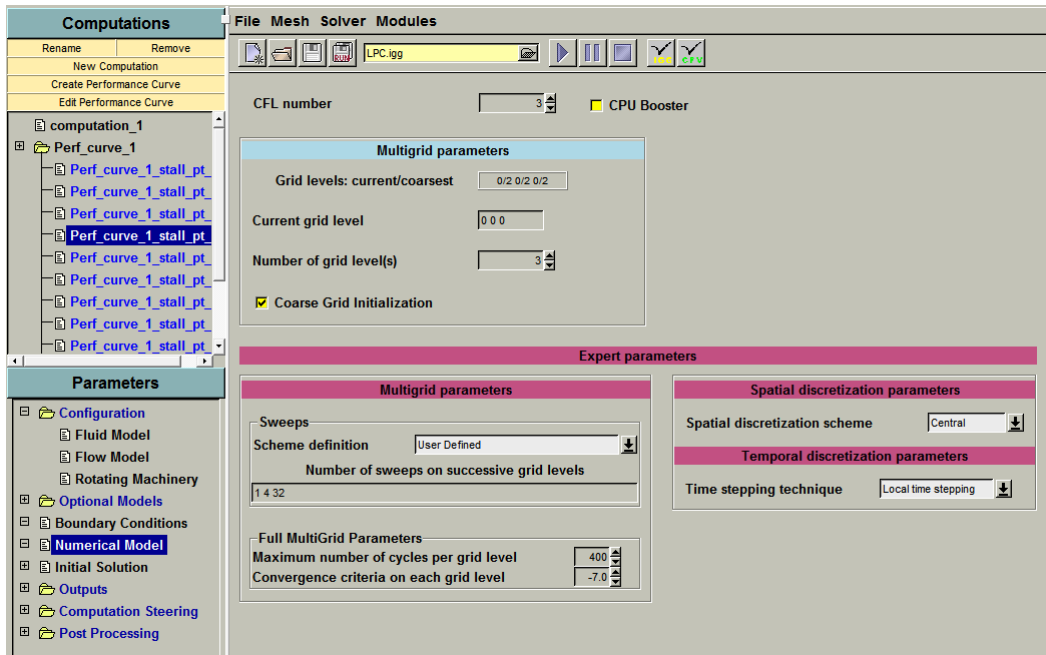


Figure 4.5: Numerical model interface

fact the information is automatically transmitted to the *FINE/Turbo* interface, so that the user doesn't need to set these boundary conditions. By default the periodic condition is set to *Matching*, which means that the number of mesh points along the connectes patches are identical and the corresponding point along these patches coincide.

The *Solid Wall Boundary Condition* can be set according to the type of calculation, if it is inviscid or viscous. For the Navier-Stokes cylindrical case, four options are available: *Adiabatic*, *Heat Flux Imposed*, *Temperature Imposed* and *Heat Transfer Coefficient Imposed*. For this project the *Adiabatic* condition is selected, with *Constant Rotation Speed* that needs to be entered by the user to the rotating blocks. At the bottom of the page the *Compute force and torque* option needs to be selected in order to include the selected patches in the calculation of the axial thrust (the sum of forces from fluid on solid, considered positive when in the direction of the z-axis) and the torque, calculated at (0,0,0).

The *External Condition* is provided to treat far-field boundaries when dealing with external flow computations, so it is not needed for the present project.

#### 4.2.5 Numerical model

This page of the CFD solver defines several numerical aspects of the computation (Fig. 4.5), such as:

- the CFL number
- the multigrid parameters
- preconditioning parameters (if applicable)

The first box allows to tune the Courant-Friedrich-Levy (CFL) number<sup>1</sup> to be employed in the computation. This number is needed to scale the time-step sizes used for the time-marching scheme of the flow solver.

The next item is the *Multigrid parameters*, in which is possible to set the *Grid levels: current/coarsest*. It indicates for each of the i, j and k directions the currently selected grid level and the number of the coarsest grid level available in the corresponding direction. Then there is an input box which allows to set the *Current grid level* for each of the i, j and k directions. The coarsest grid level indicates the number of times the grid can be coarsened along each direction. For example, if the grid has  $17 \times 33 \times 33$  points, it has respectively  $16 \times 32 \times 32$  cells. So the i direction (16 cells) can be divided 4 times by 2, while the others can be divided 5 times by 2. On the other hand, the current grid level is the finest grid level for each direction on which the computation will take place. The levels should be in the range between 0 and the coarsest grid level available. Usually a (0 0 0) level gives a finer solution. The last input box of the multigrid parameters is named *Number of grid levels*. It allows to accelerate the convergence because the flow calculation is performed simultaneously on all the grid levels. Furthermore, the button *Coarse Grid Initialization* permits to perform a preliminary flow calculation on a coarser mesh automatically created. When this option is activated, the computation starts on the coarsest grid level and includes a finer grid level each time on of the following criteria is satisfied:

- The maximum number of cycles on each grid level is reached. This value can be specified through the input box in the *Full MultiGrid Parameters* area.
- The residual on the current grid level goes under a certain order of magnitude which can be specified in the *Convergence criteria on each grid level* input box.

Among the expert parameters is present the *Sweeps* box. It permits to select the number of sweeps to be performed on the coarse grid levels through the *Number of sweeps on successive grid levels* input box. Physically, the number of sweeps indicates the amount of times the Runge-Kutta operator is applied. Recommended set of values in case of 3 grid levels is (1 4 32).

#### 4.2.6 Initial solution

In this page is possible to set the computation start from an initial solution. Four initial solution types are available: *constant values*, *from file*, *for turbomachinery* and *from throughflow*. The third type will be used. The initial solution for turbomachinery, in fact, is used for cylindrical rotating machinery. Its characteristics are listed here:

- it respects the inlet and outlet boundary conditions imposed;
- it assumes a constant rothalpy<sup>2</sup> along symmetric stream surfaces;
- the velocity field is automatically aligned with the blade passage;

<sup>1</sup>The CFL (or simply Courant) number depends on velocity, cell-size and time step and is typically calculated for each cell. A physical explanation, for a CFD simulation, of the Courant number could be that it tells you something about how fluid is moving through your computational cells. If the Courant number is  $\leq 1$  fluid particles move from one cell to another within one time step. If it is  $> 1$  a fluid particles moves through two or more cells at each time step. Usually, the higher the CFL number, the faster the convergence will be.

<sup>2</sup>The rothalpy is a function that remains constant throughout a rotating machine, i.e in an adiabatic irreversible process relative to the rotating component. It is defined as:

$$i = h + \frac{1}{2}v_r^2 - \frac{1}{2}u^2$$

where  $h$  is the static enthalpy,  $v_r$  the relative velocity and  $u$  the rotor dragging speed.

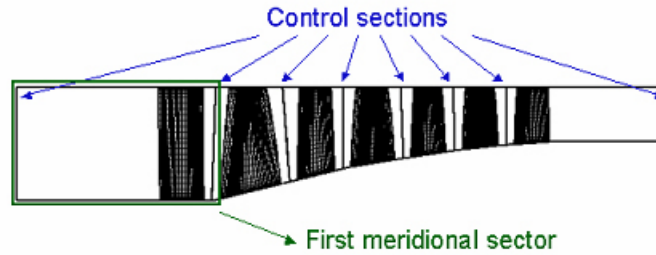


Figure 4.6: Division of the meridional view in meridional sectors

- it works only with subsonic inlet boundary conditions.

The initial solution for turbomachinery is solved on the 2D meridional view, which is divided in different parts called *meridional sectors*. In Fig. 4.6 are displayed the control sections of the meridional mesh generated by *Autogrid5*. They also define these meridional sectors. The conservation of mass and rothalpy is applied on the streamlines of each meridional sector. Then the initial solution in the 2D meridional view is interpolated in the 3D mesh.

The initial solution for turbomachinery interface is divided into three main parts: the *Channel main entrance*, the *Rotor/stator interfaces* and the *Channel main exit* (Fig. 4.7).

The channel main entrance box lists all the existing inlet patches that belong to the first raw. In this project the main entrance patch is *IGV\_flux\_Main\_Blade\_upStream\_inlet*. On the right side of the page it is needed to set the type and the value of the static pressure (*Constant distribution* with an estimated static pressure of  $100000Pa$ ).

The internal R/S connections box lists all the existing rotor/stator interfaces. Also here it is needed to set the static pressure.

Finally the channel main exit lists all the existing outlet patches belonging to the last raw (*Stator\_3\_flux\_Main\_Blade\_downStream\_outlet*). No pressure needs to be set because this patch is an actual outlet.

#### 4.2.7 Outputs

In this interface it is possible to specify the outputs generated by the solver. Among the *Computed variables* are needed to be calculated all the quantities, which include *Thermodynamics*, *Velocities*, *Vorticities*, *Residuals*, *Solid data* and *Turbulence*. In the same way is necessary to select all the quantities among the *Azimuthal Averaged Variables*, which relates to the pitchwise-averaged outputs. The global output is then written in an ASCII file with the .mf extension. The file which can be used in *CFView* in order to analyze the results has the .run extension.

#### 4.2.8 Computation steering

In the *Computation Steering/Control Variables* page, shown in fig. 4.8, the user can define some global parameters for the computation:

- *Maximum Number Of Iterations* on the finest grid level, set to a test value of 300.
- *Convergence Criteria* represents the negative number of orders of magnitude the norm of the residuals must decrease before stopping the calculation. If this criterion is not reached the calculation proceeds until the the maximum number of iterations.

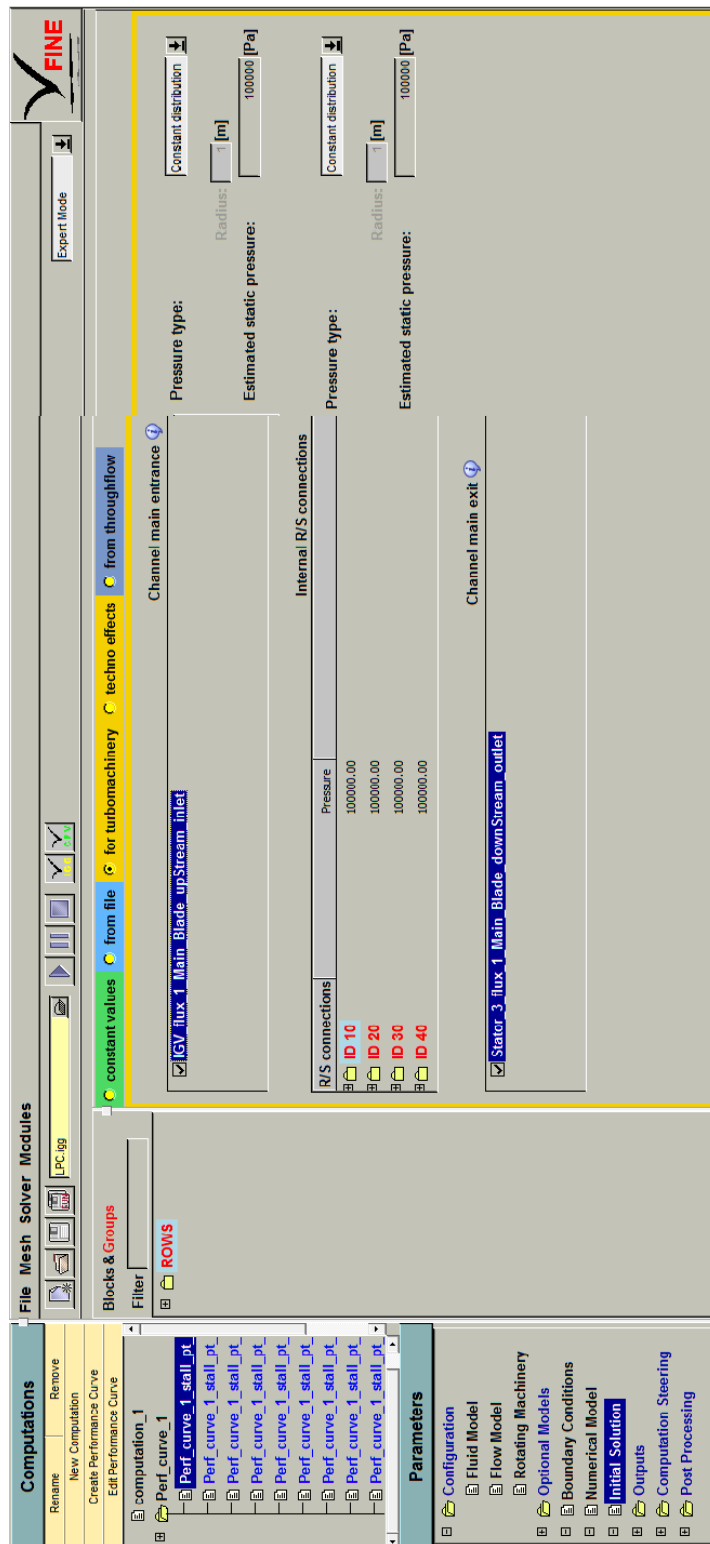


Figure 4.7: Initial solution for turbomachinery interface

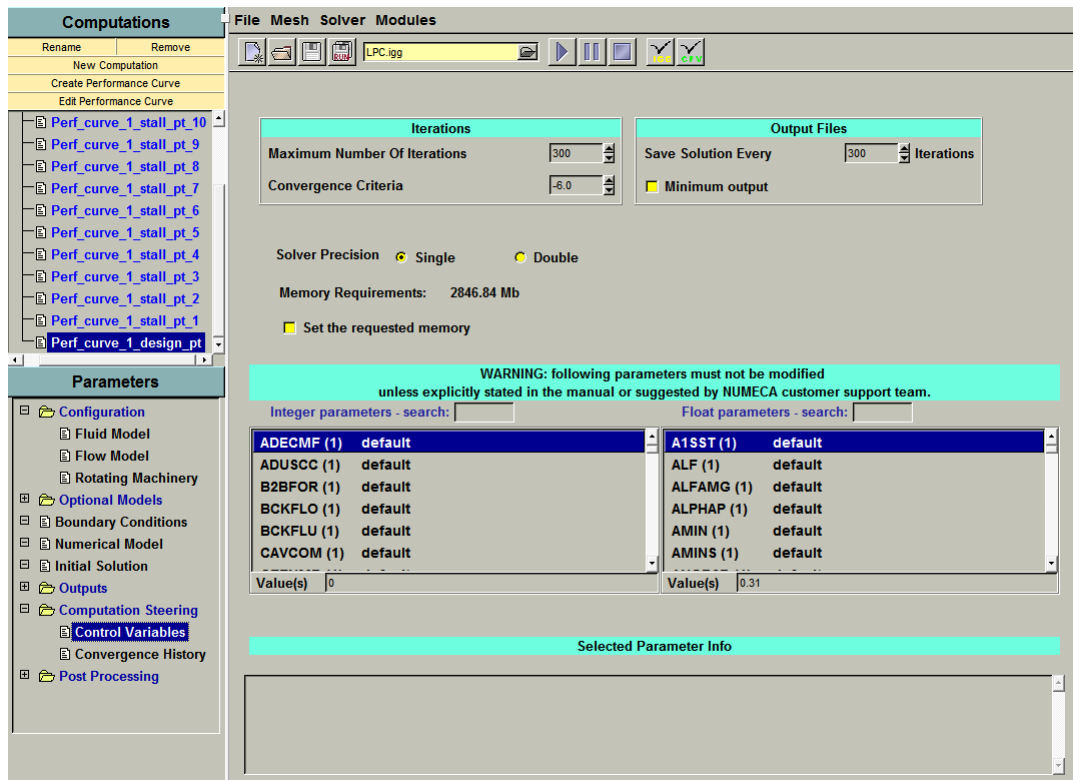


Figure 4.8: The Control Variables page

- *Save Solution Every* allows to set the frequency of creating the output files to be read in *CFView*
- *Solver Precision*, which can be single or double. Usually, the single precision solver is preferred because it is accurate enough and demands less memory consumption.

#### 4.2.9 Performance curve

Once the project features are fully set, is necessary to create a *Performance Curve*, which is a graphical representation that shows the characteristics of the compressor. So will be visualized the *Outlet Static Pressure* in  $[Pa]$  versus the *Mass Flow* in  $[kg/s]$ , (fig. 4.9). It is necessary to impose the number of operating points and the boundary conditions. In particular, the parameters needed to be inputted are: the *Rotation Speed*, the *Number of points in stall and choke region* (although it is more interesting to analyze the situation near the stall region), the *Stall area control* (which will be of the *Outlet Pressure* type) and the *Initial Solution from* (by default, the initial solution is set from the previous operating point, except for the design point). On the right side of the *Performance Curve Definition* box is possible to input an initial value of *Outlet Static Pressure* for each operating point. For instance, starting from a value of  $90000[Pa]$  for the design point until a value of  $190000[Pa]$  for the supposed stall point.

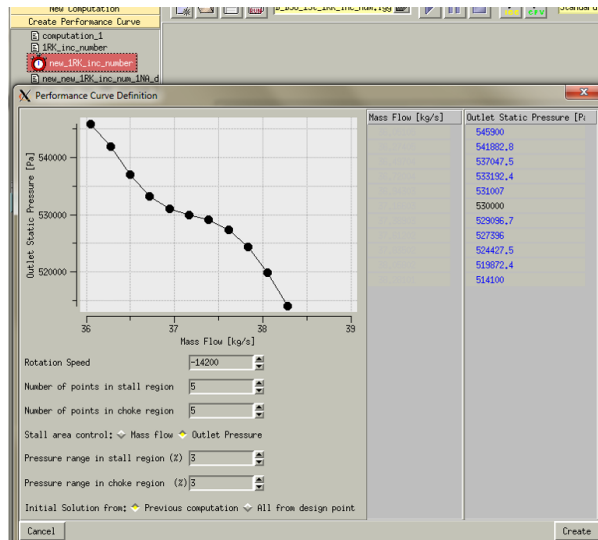


Figure 4.9: Performance curve definition

## 4.3 Choice of the “best” mesh and CFD solution

In this section the results coming from the CFD computation of the *Stage 37* will be analyzed. The calculation tends to be very complex, heavy and long. It is for this main reason that it has been conducted by using the university computer cluster in order to speed up the process.

To obtain correct results for each operating point, it is necessary to give a look to the *Performance Curve* results, within the *Post Processing* page. If the outlet and inlet pressure are very distant from one another, or, if the mass flow value sharply drops, it is needed to manually correct the initial value of the outlet static pressure for that operating point and restart the calculation from the previous point. Otherwise, no action is needed and the calculation will proceed without problems. In some cases, especially for points near the stall region, the maximum number of iterations should be increased, as seen in the paragraph 4.2.8.

Results coming from all the CFD calculations made with different meshes will be analyzed and compared to the NASA’s experimental curves. Results will be analyzed comparing efficiency and pressure ratio vs mass flow plots. Moreover, another useful instrument for choosing of the “best” mesh will be the Numeca application *CFView*. In fact it helps to visualize parameter contours in compressor sections, such as relative/absolute pressure, velocities and turbulent viscosity. The mesh evaluated as the most accurate will be then applied to the NK-36ST compressor project.

As usual, FP and B2B parameters will be treated independently, thus their mutual influence will be not considered.

In Tab. 4.1 the choices for all mesh parameters are summarized.

### 4.3.1 Influence of FP mesh parameters

#### Expansion Ratio

As shown in performance curves in Fig. 4.10, meshes with high ER, i.e.  $ER = 1,6$  and  $ER = 1,8$ , seem to be the worst. By giving a look at the left part of the graphs, it is clear that the stall points occur too soon for these meshes, meaning that they are too coarse to get reliable results. Otherwise, for the remaining two meshes, good results are obtained and, in particular,  $ER = 1,4$

gives closest results to the experimental data. Moreover, confirming what just said about ER1.2 and ER1.4 meshes, opening the CFD results file for the maximum efficiency points in *CFView*, it is clear how they better represent flow turbulences and unsteadiness (Fig. 4.14). For the aforementioned reasons, the selected mesh parameter will be  $ER = 1, 4$ .

### Max Aspect Ratio

From pressure ratio and efficiency curves (Fig. 4.11) is notable that  $MR_{200}$  and  $MR_{1000}$  are coincident respectively with  $MR_{500}$  and  $MR_{2000}$ . Fig. 4.15 shows turbulent viscosity contours in the rotor section and absolute total pressure contours in the stator section (in the maximum efficiency points). As expected, better results are obtained for lower maximum aspect ratios, even if differences are not so clear. Considering results analysis, questions of memory allocation and solution end time, the mesh with  $MR = 1000$  is chosen.

### Dimensionless wall distance $y^+$

Fig. 4.12 displays performance curves for changing dimensionless wall distance. Regarding the compressor map, curves with  $y^+ = 0, 5$  and  $y^+ = 1$  appear to be closer to the experimental curve and these meshes well simulate the flow pass in the stall point. By giving a look to the efficiency vs mass flow plot this hypothesis seems to be confirmed by the maximum efficiency points: those meshes reach approximately the same maximum value of the NASA's report. Turbulent viscosity contours and absolute total pressure respectively in a rotor section and a stator section are shown in Fig. 4.16. Meshes with  $y^+ = 0, 5$  and  $y^+ = 1$  have very similar behaviours, however the former uses a greater number of elements, that means more memory request and calculation time. Thus, the mesh with  $y^+ = 1$  is chosen.

## 4.3.2 Influence of B2B mesh parameters

### Mesh density

In Figs. 4.13 are shown the compressor map and the efficiency curve obtained for different meshes created by varying the number of elements in the  $L$  and  $H$  blocks in the B2B view. In theory, meshes with higher number of elements should better describe the flow. In fact, especially in the pressure ratio plot,  $B2B2$ ,  $B2B3$  and  $B2B4$  present the closest results to the experimental curve. Even in the flow visualizations of the maximum efficiency point in Fig. 4.17, this situation is confirmed: increasing the mesh elements, higher values of turbulent viscosity are visible in the blades pressure side, meaning that flow separation is better represented. Also here, mostly for reasons of simplification, the mesh  $B2B_0$  is chosen.

### O-layer

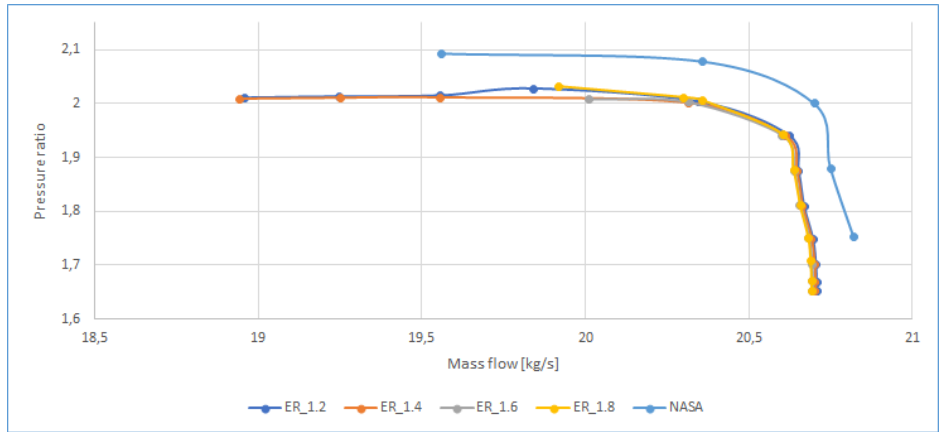
Varying the number of mesh elements in the O-layer is not possible to detect relevant differences in performance curves. For this reason, the finest number of O-layer elements will be decided through flow visualizations in *CFView* in a plane parallel to the plane passing through the axis of the engine (Fig. 4.18). Both images refers to the maximum efficiency point in the performance curves. Except a little increase for turbulent viscosity values, increasing the number of O-layer elements there is no clear improvement in the flow representation. Thus, a mean value  $Olayer_0$  is chosen.

### B2B Expansion Ratio

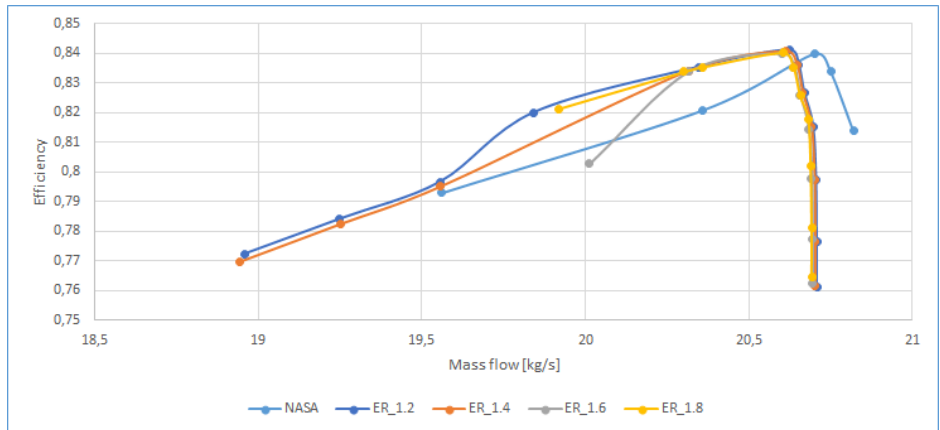
Even in this case, changing the value of this parameter no substantial discrepancies are visible in the performance curves plots. Thus, also here, the “best” mesh will be chosen only by looking at the CFView flow visualizations (Fig. 4.19). No appreciable differences are visible, thus a mean value  $ER_{B2B} = 1, 2$ , is chosen.

Table 4.1: Mesh parameters summary

<b>ER</b>	<b>MR</b>	<b>y<sup>+</sup></b>	<b>B2B</b>	<b>O-layer</b>	<b>ER<sub>B2B</sub></b>
1, 4	1000	1	<i>B2B_0</i>	<i>Olayer_0</i>	1, 2

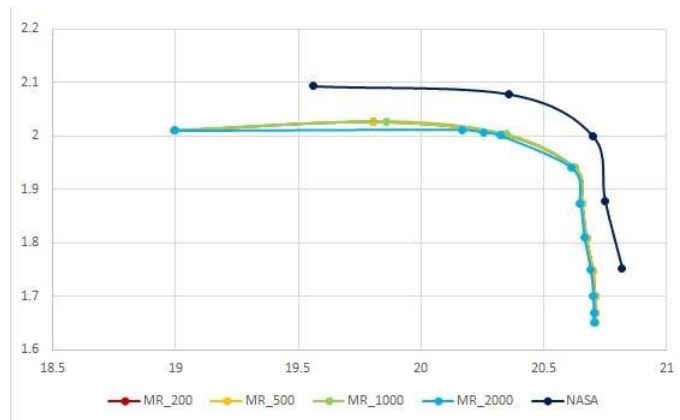


(a) *Compressor map*

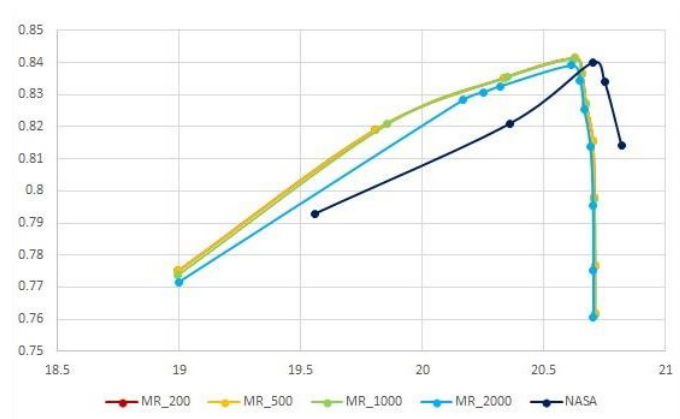


(b) *Efficiency*

Figure 4.10: Influence of ER on performance curves

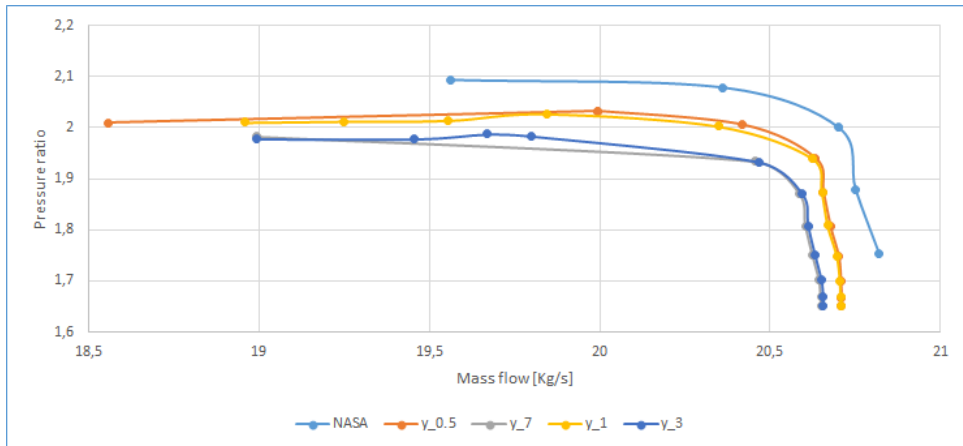


(a) *Compressor map*

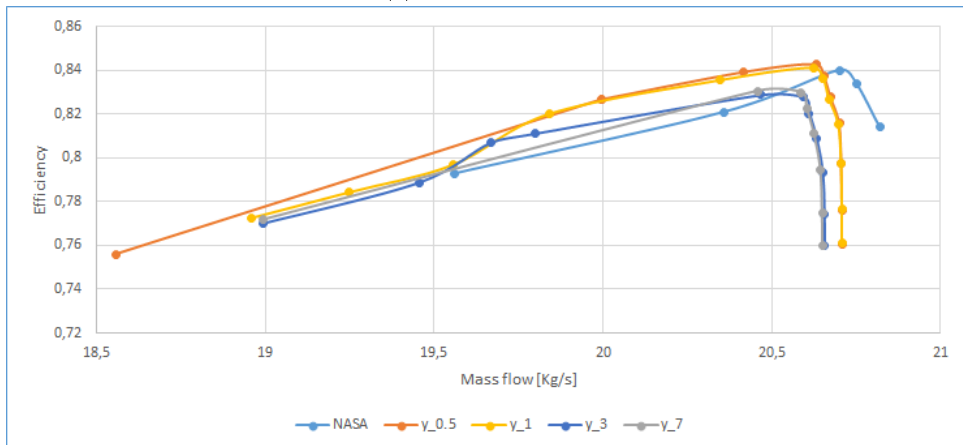


(b) *Efficiency*

Figure 4.11: Influence of MR on performance curves

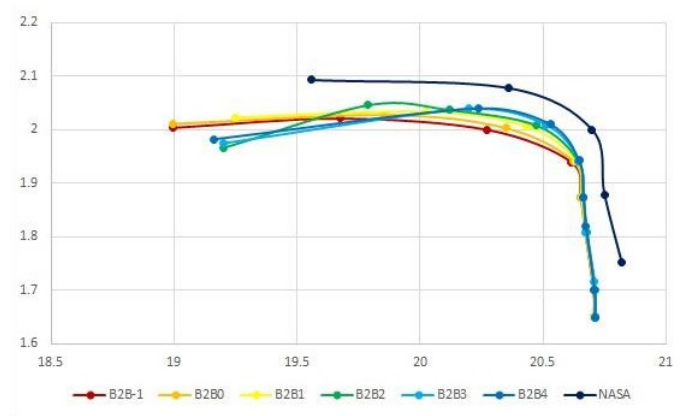


(a) Compressor map

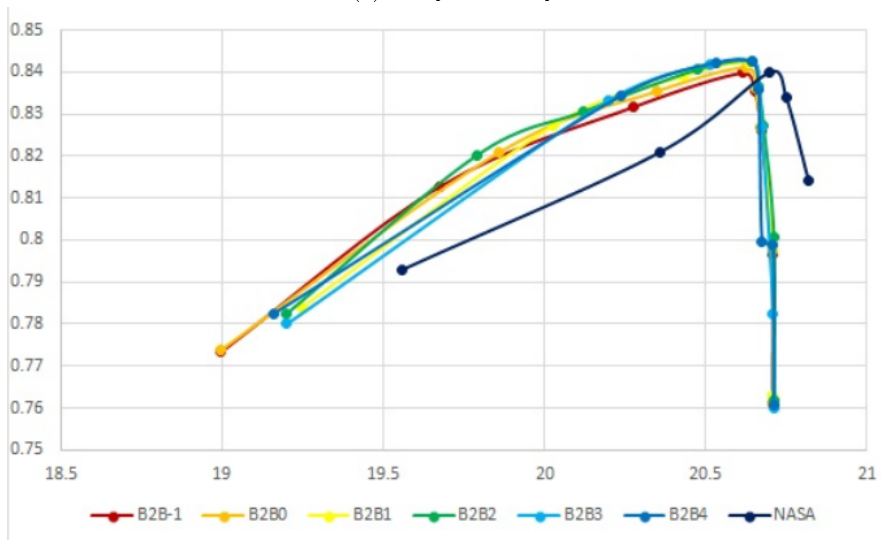


(b) Efficiency

Figure 4.12: Influence of  $y^+$  on performance curves

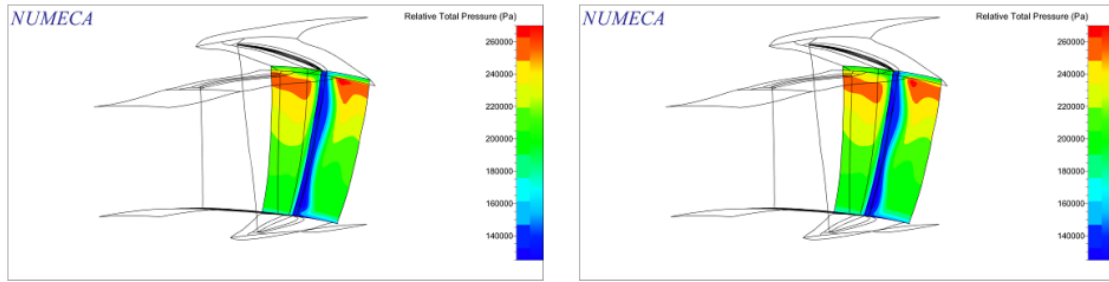


(a) *Compressor map*



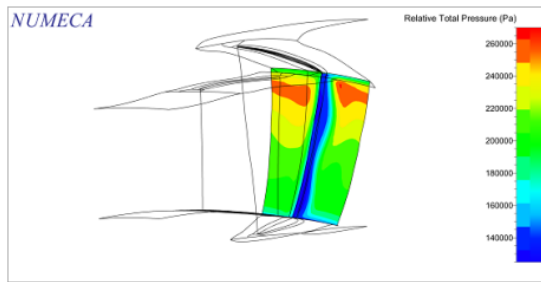
(b) *Efficiency*

Figure 4.13: Influence of mesh density on performance curves

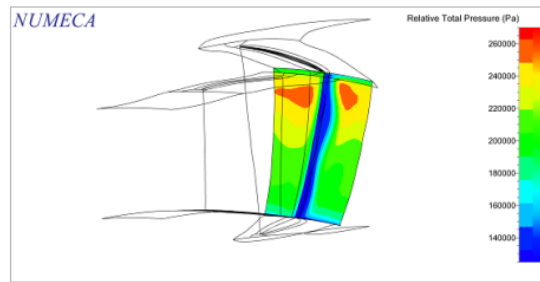


(a) *E.R. 1.2.*

(b) *E.R. 1.4*

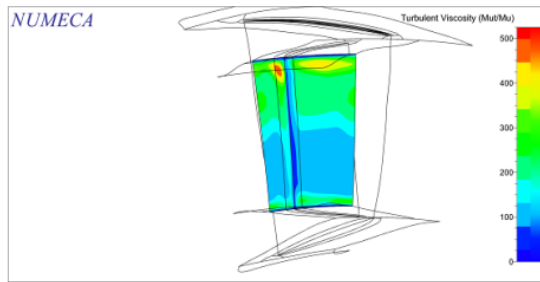


(c) *E.R. 1.6*

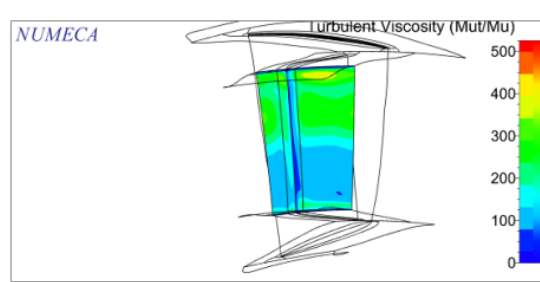


(d) *E.R. 1.8*

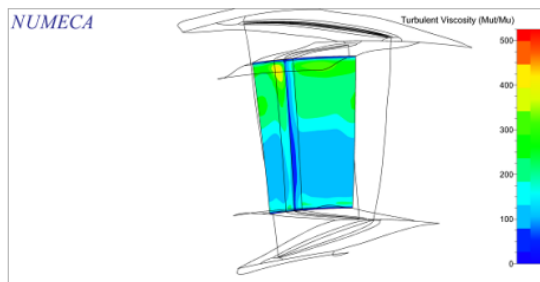
(a) *Relative total pressure in rotor transversal section*



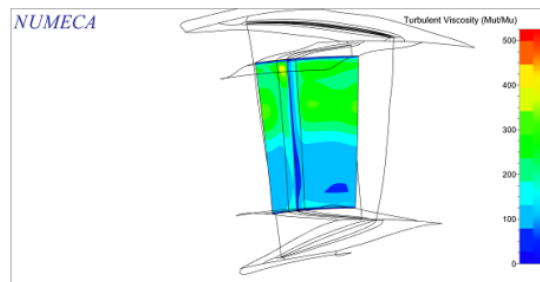
(a) *E.R. 1.2.*



(b) *E.R. 1.4*



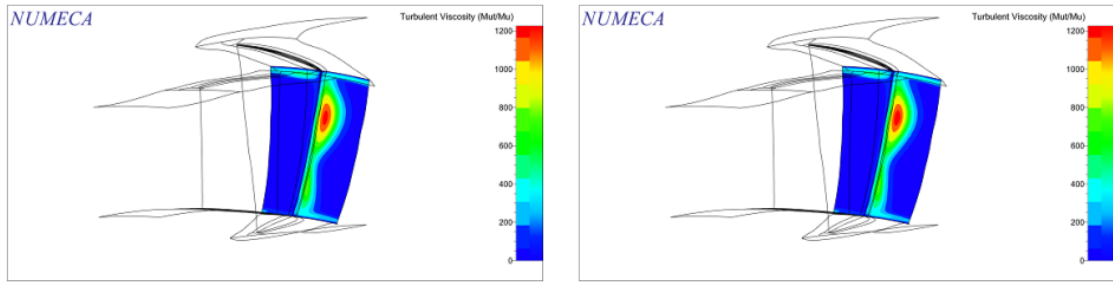
(c) *E.R. 1.6*



(d) *E.R. 1.8*

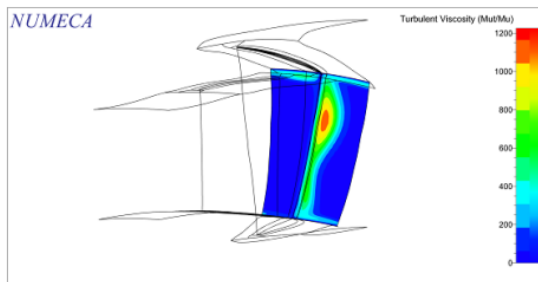
(b) *Relative total pressure in stator transversal section*

Figure 4.14: Influence of ER on flow visualization

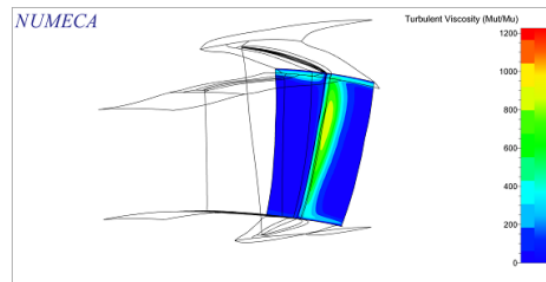


(a) *MR 200.*

(b) *MR 500*

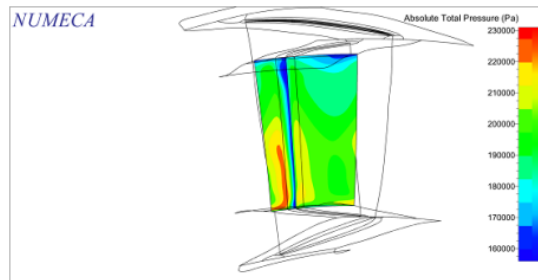


(c) *MR 1000*



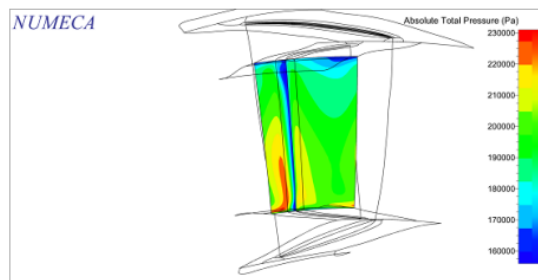
(d) *MR 2000*

(a) *Turbulence viscosity in rotor section*

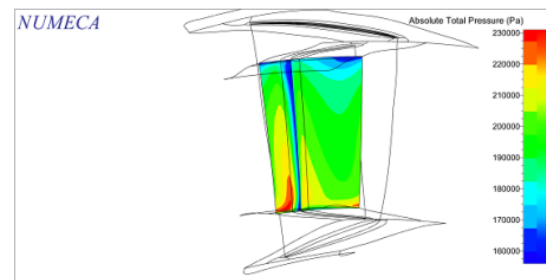


(a) *MR 200.*

(b) *MR 500*



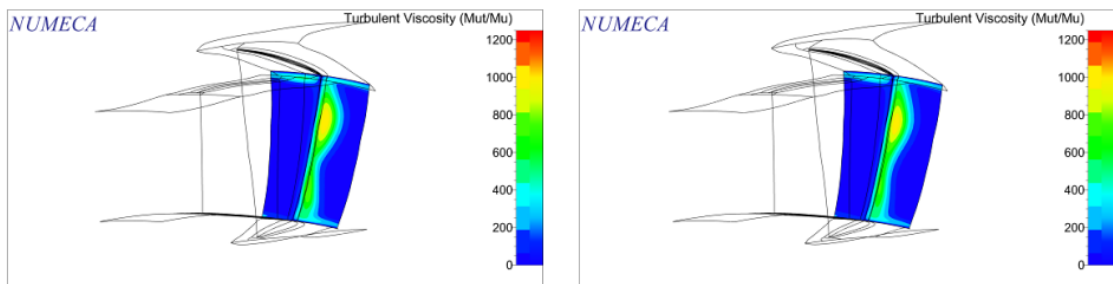
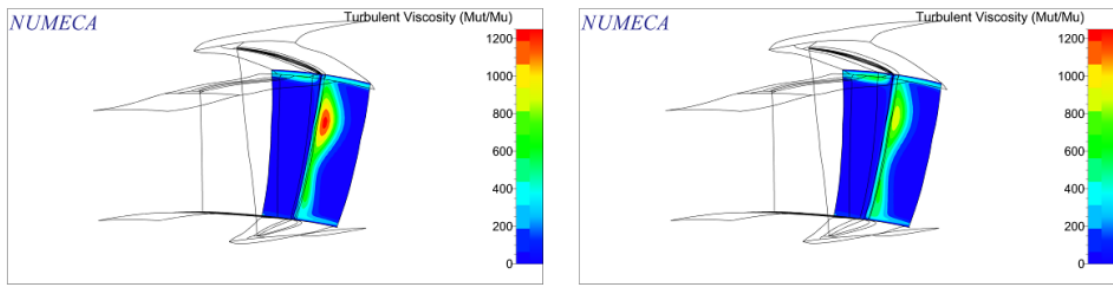
(c) *MR 1000*



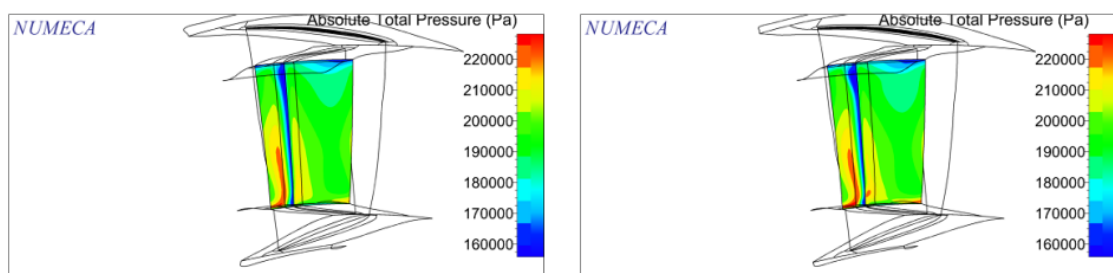
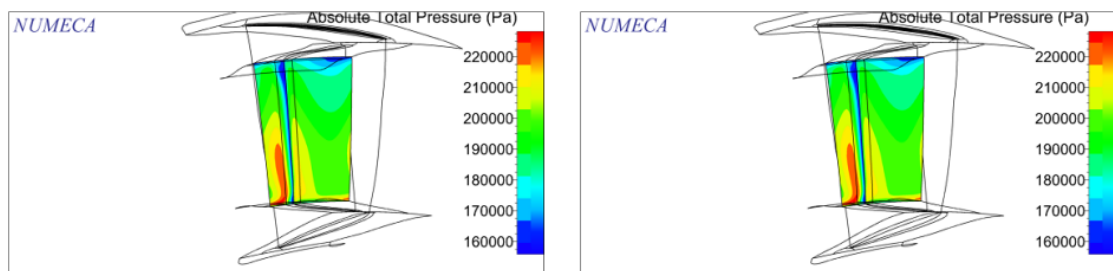
(d) *MR 2000*

(b) *Absolute total pressure in stator section*

Figure 4.15: Influence of MR in flow visualization



(a) Turbulent viscosity in rotor transversal section



(b) Absolute total pressure in stator transversal section

Figure 4.16: Influence of  $y^+$  on flow visualization

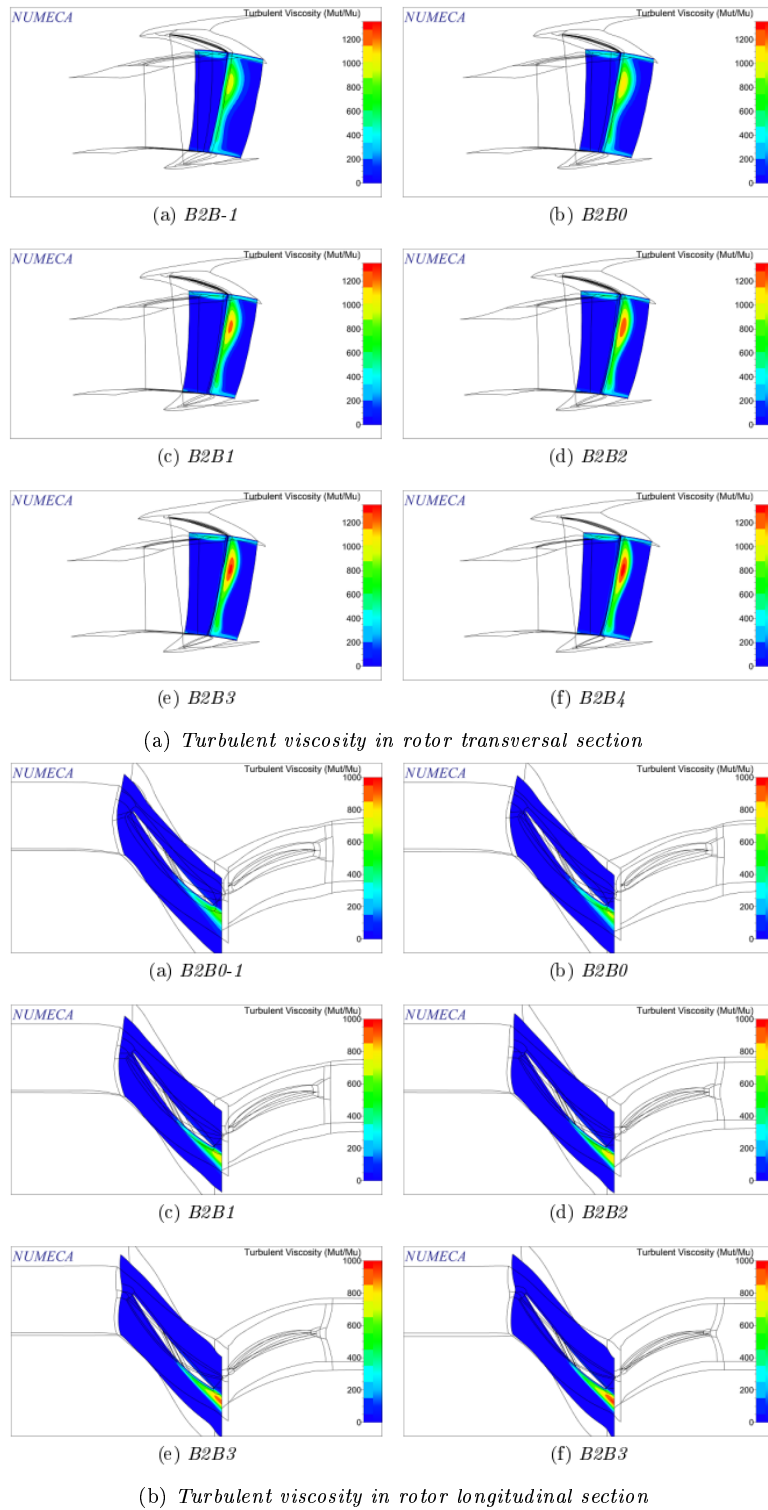
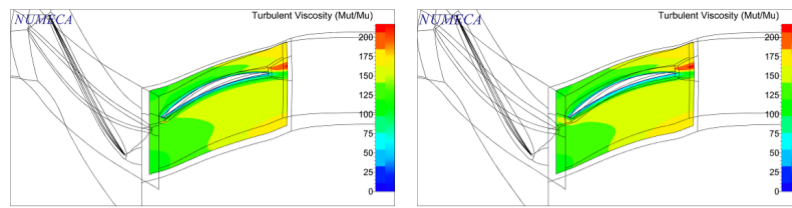
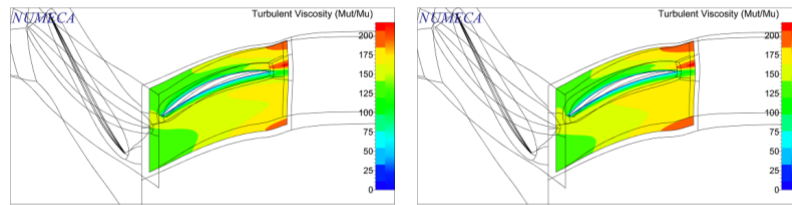


Figure 4.17: Influence of mesh density in flow visualization



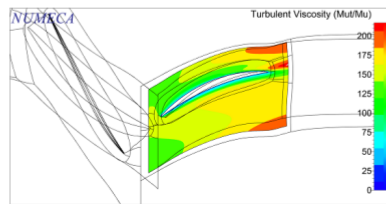
(a) *Olayer -2*

(b) *Olayer -1*



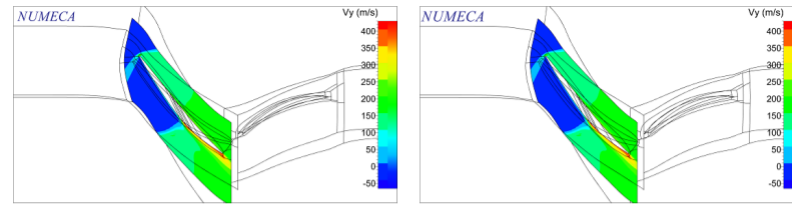
(c) *Olayer 0*

(d) *Olayer 1*



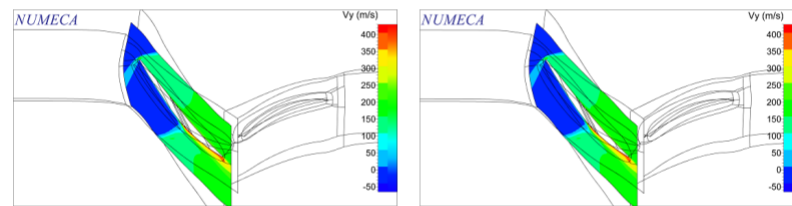
(e) *Olayer 2*

(a) *Turbulent viscosity in rotor longitudinal section*



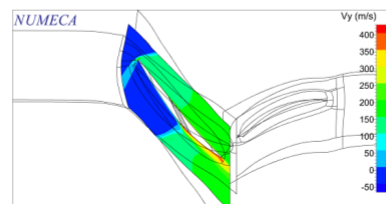
(a) *Olayer -2*

(b) *Olayer -1*



(c) *Olayer 0*

(d) *Olayer 1*



(e) *Olayer 2*

(b) *V<sub>y</sub> velocity in rotor longitudinal section*

Figure 4.18: Influence of O-layer in flow visualization

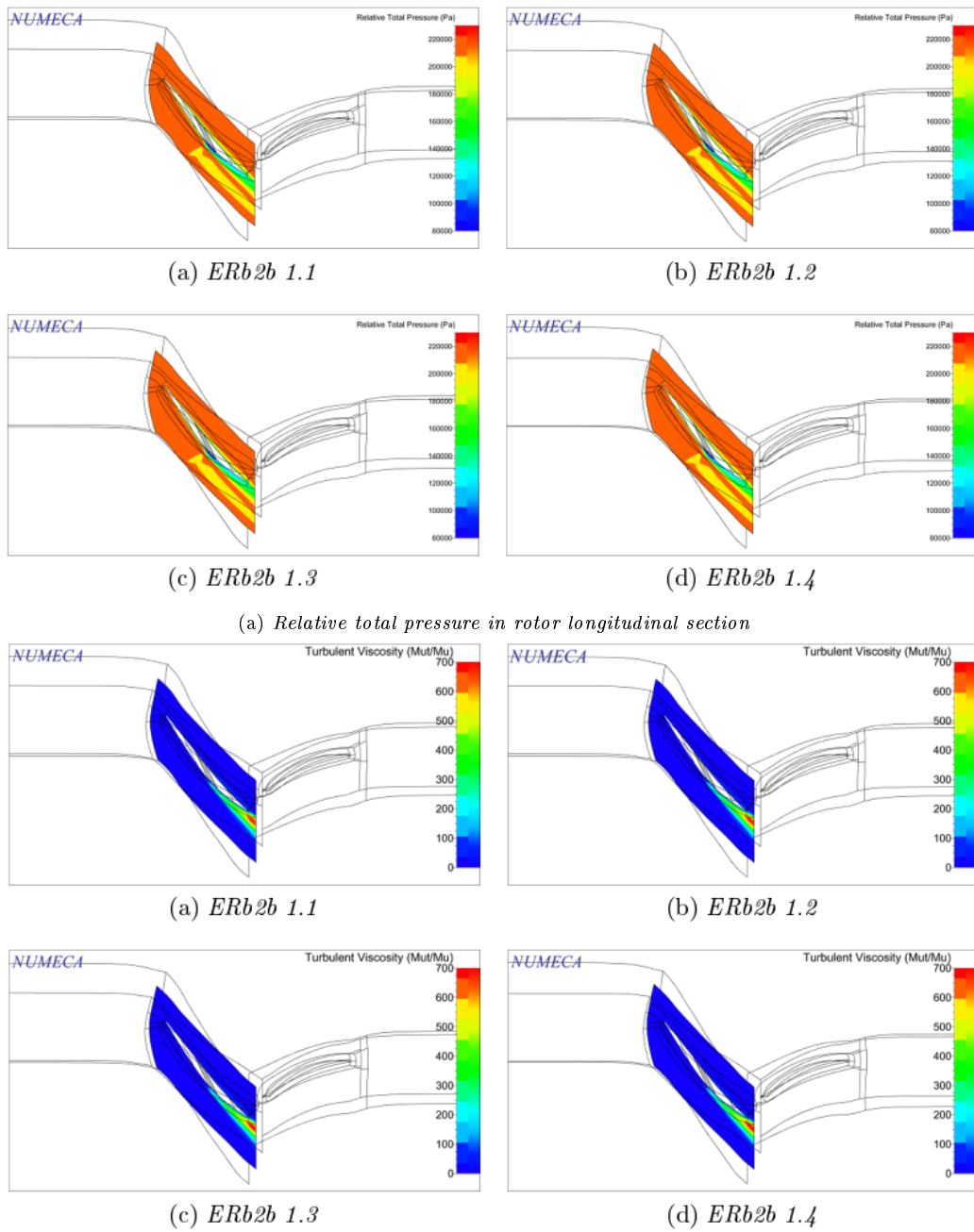


Figure 4.19: Influence of  $ER_{B2B}$  on CFD results

### 4.3.3 Evaluation of the exciting aerodynamic force

Now that the “best” mesh has been identified, it can be applied to the NK-36ST Low Pressure Compressor. Once loaded the \*.trb meshed file onto FINE/Turbo, the project can be completed by applying the same procedure as done with the *Stage 37*.

After simulating the CFD analysis and adjusting outlet static pressures in the *Performance Curve* definition, the compressor map of the whole LPC of the engine is visualized (Fig. 4.21). Results can be examined in the design point folder of the project directory. The design point comes from official engine documents and it is characterized by the following abscissa and ordinate values (highlighted in the compressor map):

$$G = 105,5 \frac{Kg}{s} \quad \text{Mass flow}$$
$$\pi_c^* = 2,18 \quad \text{Pressure ratio}$$

Opening the \*.mf file, located in the design point folder, it is possible to look at all quantities calculated by the CFD analysis, including relative/absolute pressures, velocities, forces and torques components. Their values are summarized in Tab. 4.2.

Fig. 4.20 shows the force vector applied to the one-sector model of the bladed disk.

Table 4.2: Aerodynamic exciting force and torque components

$f_x$	$f_y$	$f_z$	$M_x$	$M_y$	$M_z$
94,7174 [N]	560,627 [N]	358,116 [N]	447,99 [N·m]	-221,40 [N·m]	217,33 [N·m]

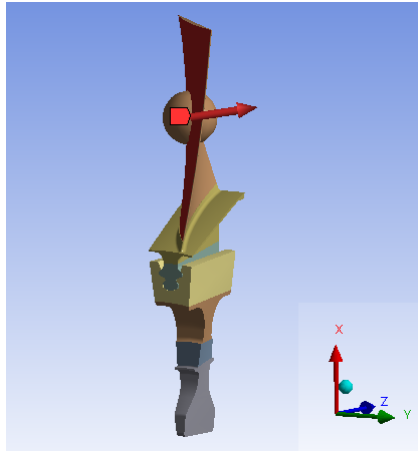


Figure 4.20: Visualization of the aerodynamic force acting on the  $i$ -th blade

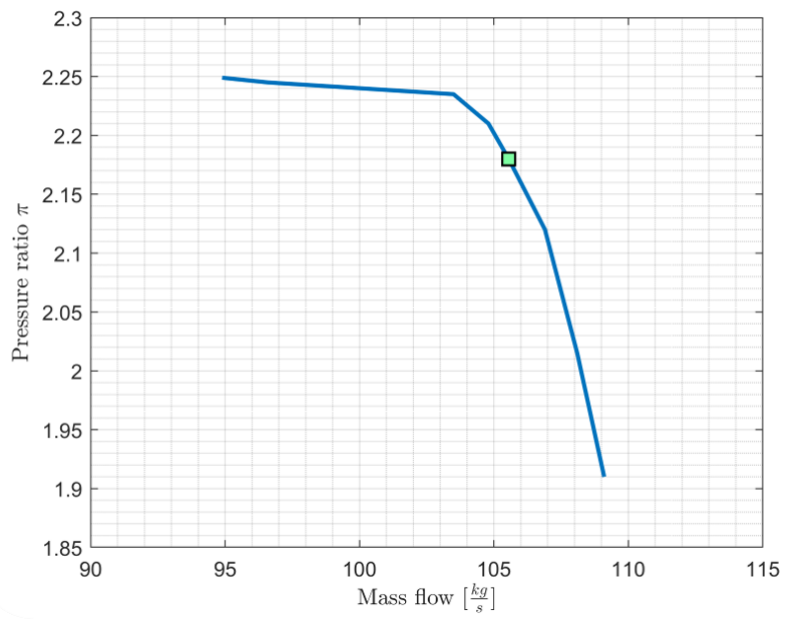


Figure 4.21: LPC map of the NK36-ST

## Chapter 5

# Calculation of blades arrangement influence

### 5.1 Introduction

In this chapter the numerical model of the bladed disk will be loaded in the *ANSYS* Workbench ambient and analyzed. Different blades arrangements will be created and studied through a static modal analysis, firstly, and a transient structural analysis after.

For each analysis object, the model will be constrained and meshed in the same way, just by duplicating the projects. At first, the bladed disk model created in *Siemens NX* is loaded, then, it is meshed and constrained through supports. Meshing procedure needs to be very accurate to have reliable results. By default, *SOLID185* is the shape function used by the program to mesh the model. Theory about shape functions can be found in [11]. After meshing the model, it needs to be constrained through boundary conditions. It is enough to apply a null *Displacement* in the *Z* (axial) direction and a *Cylindrical Support* on the walls of the disk cavity.

The finite element model of the bladed disk and the location of its supports are shown in Fig. 5.1.

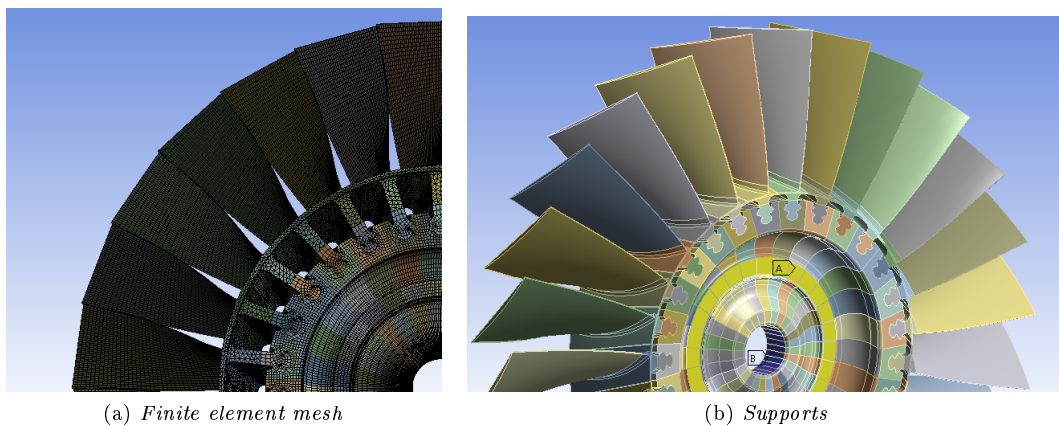


Figure 5.1: Mesh and supports definition of the bladed disk

Table 5.1: Titanium alloys mechanical properties

	Ti Alloy 1	Ti Alloy 2	Ti Alloy 3	
Density	4460	4460	4460	$[kg \cdot m^{-3}]$
Young's Modulus	110	120	130	$[GPa]$
Poisson's Ratio	0,3	0,3	0,3	
Bulk Modulus	91,67	100	108,33	$[GPa]$
Shear Modulus	42,308	46,154	50	$[GPa]$

### 5.1.1 Mistuning modelling in the bladed disk

Deviations of blades from the ideal situation are very small: they can differ in shape, density or stiffness. In this work, mistuning is realized in the model considering little Young's modulus deviations from its nominal value in Titanium alloys (see Ti alloy 1 in Tab.5.1). Other approaches, for instance changing in blades shape, could have resulted difficult and expensive in terms of time and computer resources. Under the assumption of little deviations, the relationship between the natural frequency and the Young's modulus can be linearized. For this aim, a modal analysis on a single blade is needed.

The very first operation is to set a modal analysis on *ANSYS* Workbench for the single compressor blade. It is a *Free Vibration* analysis, in which the natural circular frequencies  $\omega_i$  and mode shapes  $\Phi_i$  are calculated from the equation (2.21), with the following assumptions:

- $[K]$  and  $[M]$  are constant:
  - Linear elastic material behavior is assumed
  - Small deflection theory is used, and no nonlinearities included
  - Damping is not included
  - No excitation of the structure is assumed
- Mode shapes  $\{\Phi\}$  are relative values, not absolute

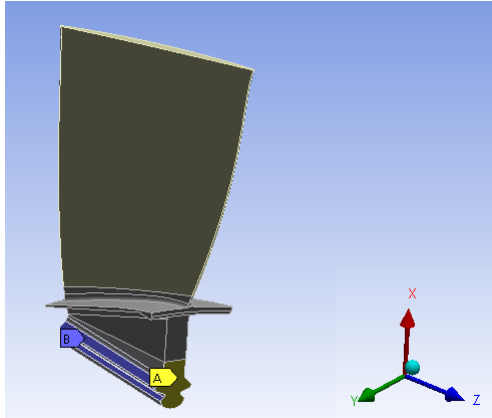
Three Titanium alloys are then created and their material properties are listed in Tab. 5.1. Subsequently, boundary conditions and constraints can be set. They are showed in Fig. 5.2a: a null *Given Displacement* (A) which constrains the blade root in the  $Z$  direction and a *Frictionless Support* (B) that fixes the normal direction of the selected body faces. The solution is then solved for each alloy, obtaining three values for the first mode frequency. The frequency trend is showed in fig. 5.2b. A linear dependency is obtained:

$$\omega = 8 \cdot 10^{-10} E + 93,513$$

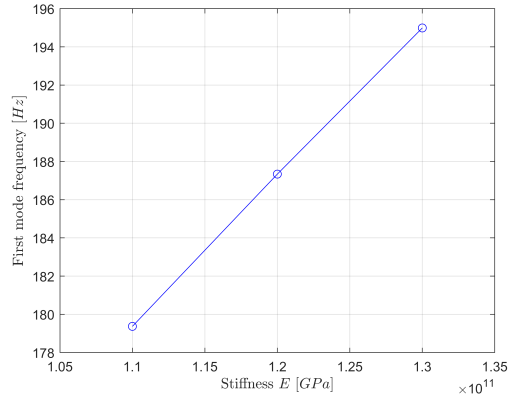
where  $E$  is the Young's modulus and  $\omega$  the first mode frequency.

### 5.1.2 Random geometric mistuning

The only way to simulate a random mistuning for compressor blades is to apply a statistical approach: generate a normal (Gaussian) distribution of frequencies and then evaluate each corresponding Young's modulus through the previous linear equation. The Probability Density Function (PDF) is characterized by a *mean value*  $\mu = 187,34[Hz]$  and a *standard deviation*  $\sigma = 1,2$ . In figure 5.3 are shown the PDF, the random array of frequencies from the normal distribution and the relative array of Young's modulus.

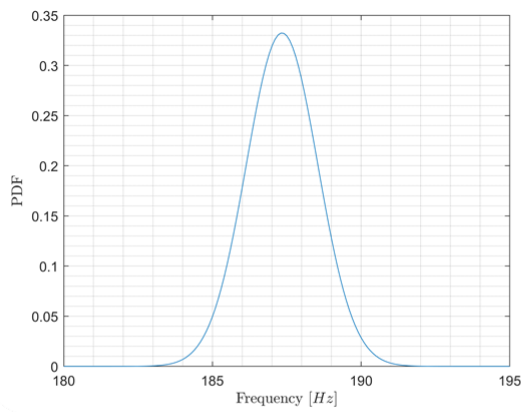


(a) Supports for the single blade modal analysis



(b) First mode frequency vs Young's modulus

Figure 5.2: Linear relationship extrapolation



Frequency [Hz]	Young's Modulus [Pa]
187,33	1,17E+11
189,18	1,20E+11
186,42	1,16E+11
187,79	1,18E+11
187,07	1,17E+11
188,68	1,19E+11
186,03	1,16E+11
187,38	1,17E+11
188,00	1,18E+11
188,66	1,19E+11
189,19	1,20E+11
187,44	1,17E+11
185,55	1,15E+11
186,45	1,16E+11
186,07	1,16E+11
190,16	1,21E+11
186,60	1,16E+11
188,24	1,18E+11
187,11	1,17E+11
188,41	1,19E+11
186,42	1,16E+11
185,66	1,15E+11
185,63	1,15E+11
187,93	1,18E+11
187,13	1,17E+11
187,10	1,17E+11
189,04	1,19E+11

Figure 5.3: Gaussian distribution of frequencies and Young's modulus computation

### 5.1.3 Creation of different mistuned patterns

Different patterns of mistuned blades will be analyzed in order to find out the best arrangement in terms of vibration localization and stress scatter.

Using the generated random array of Young's modulus in the previous paragraph, six blades arrangements are created only by relocating the same 27 blades. They are shown in Fig. 5.4 and here explained (darker shades stand for higher values of stiffness):

- $r$ , in which the blades arrangement is absolutely random;
- $a1$ , characterized by an alternate pattern of blades: those with low Young's modulus are always followed by blades with higher stiffness;
- $a2$ , similar to the  $a1$  pattern, but this time blades are alternate two by two;
- $a3$ , with blades that are alternate three by three;
- $g1$ , where the stiffness gradient from one side of the disk to the other is the minimum possible;
- $g2$ , in which the two blades with highest stiffness are attached on the opposite sides of disk and blades with decreasing  $E$  are attached one after another on both sides.

## 5.2 Modal analysis and influence on mode shapes

In this section the influence of different positioning of blades around disk circumference on mode shapes and on vibration amplitudes will be evaluated. At the end of the analysis, the "best" pattern will be chosen in relation to vibration localization, as it will be explained.

### 5.2.1 Modal analysis of the tuned bladed disk

The focus now shifts on the tuned bladed disk. A new Modal Analysis object can be dragged in the *Ansys* Project Schematic. In the tuned, ideal case, the disk is equipped with absolutely identical blades, namely with the same Young's modulus ( $E = 120$  [GPa]). After meshing and constraining the model, the analysis can be run.

In the idealized case, the bladed disk can be thought as divided in 27 identical sectors and the structure has cyclic symmetry (according to what said in the paragraph 2.2.3). The free linear vibrations of cyclic structures have an important characteristic: each system mode shape consists of identical motions in each sector except for a fixed sector-to-sector phase difference. For this reason, the mode shapes are sinusoidal in the circumferential direction and are represented as nodal diameters.

Among the analysis solution tab is important to have a look to the *Total deformation* results in order to distinguish and recognize each nodal diameter-mode shape. The maximum number of nodal diameters depends on the blade number  $N = 27$ , which is odd, thus:

$$k = \frac{N - 1}{2} = 13$$

All 13 bending mode shapes are identified and distinguished from torsional mode shapes, which are not relevant for this work. As example, two mode shapes for the tuned system are shown in Fig. 5.6. In (a) is displayed the second mode (two nodal diameters), in (b) the third mode (three nodal diameters).

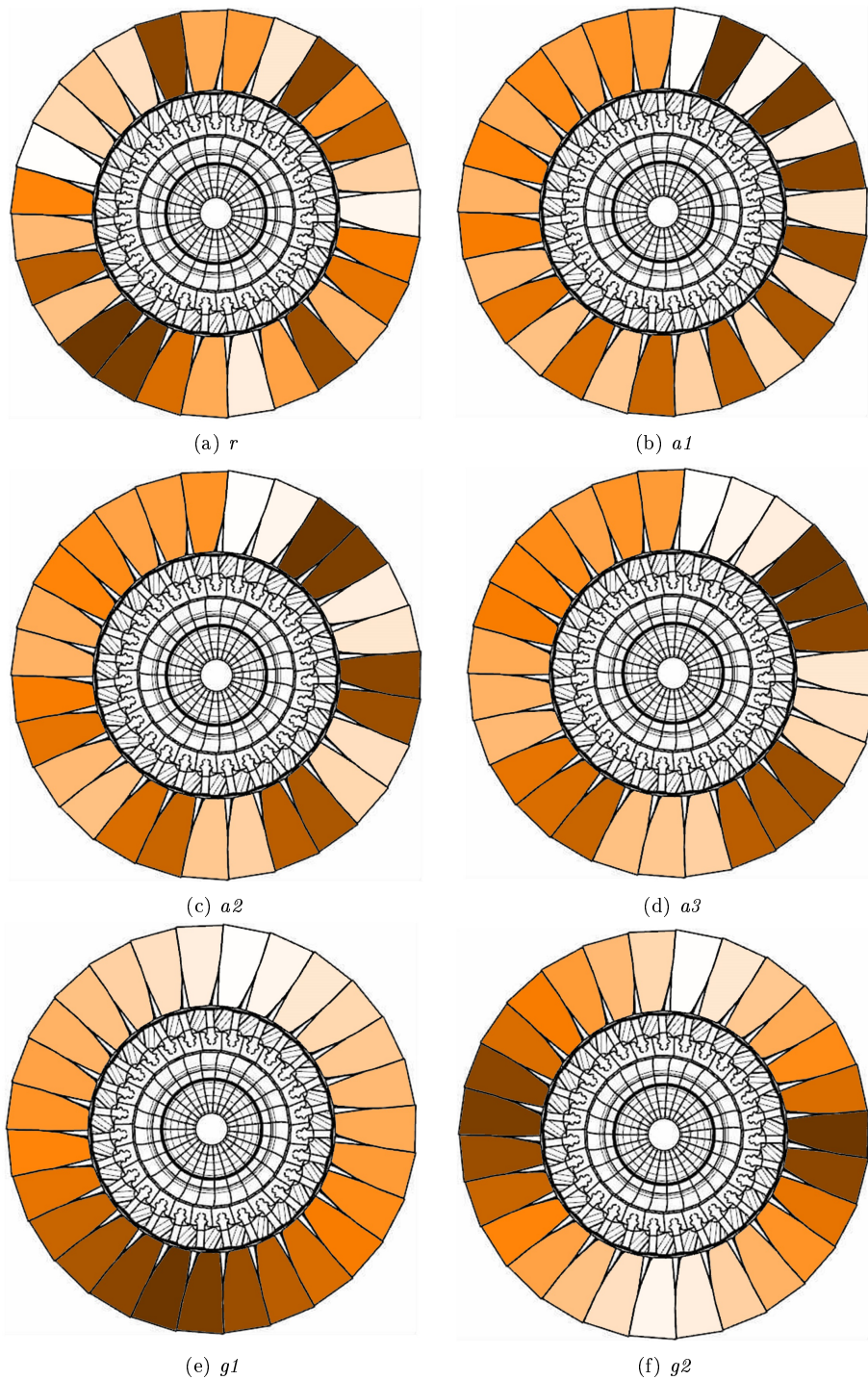


Figure 5.4: Different mistuned blades patterns visualization

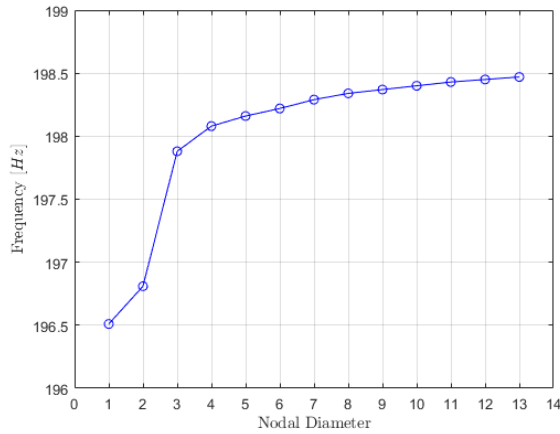


Figure 5.5: Free-vibration natural frequencies vs nodal diameters

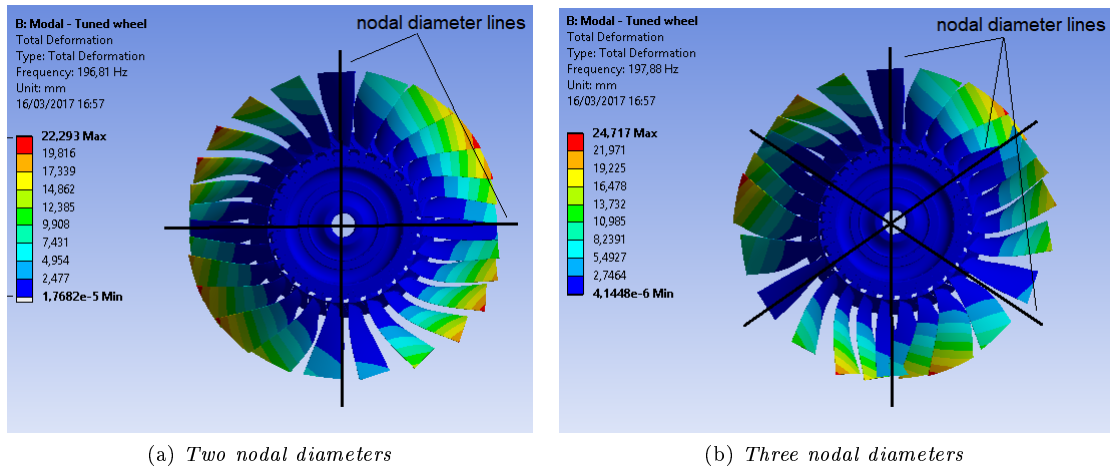


Figure 5.6: Mode shapes of the tuned bladed disk

The natural frequencies relative to these modes are then plotted as a function of the number of nodal diameters, or mode shapes in Fig. 5.5. These frequency values will be useful in the mistuned mode shapes identification, in which nodal diameters will be no more noticeable.

Among the modal analysis solution tab, an *User Defined Result*, expressed as the displacement in the  $Z$  direction, has to be set in the leading edge vertex of each blade. Collecting the results for each blade, allows to build the sinusoidal pattern of the mode shapes in the circumferential direction. The cyclic symmetry of the tuned system allows to predict the vibration and displacement trend of the entire bladed disk. Displacements for each blade are then normalized with their maximum value module and plotted as function of the number of blades. Normalized displacements for the first four mode shapes are represented in Fig. 5.7.

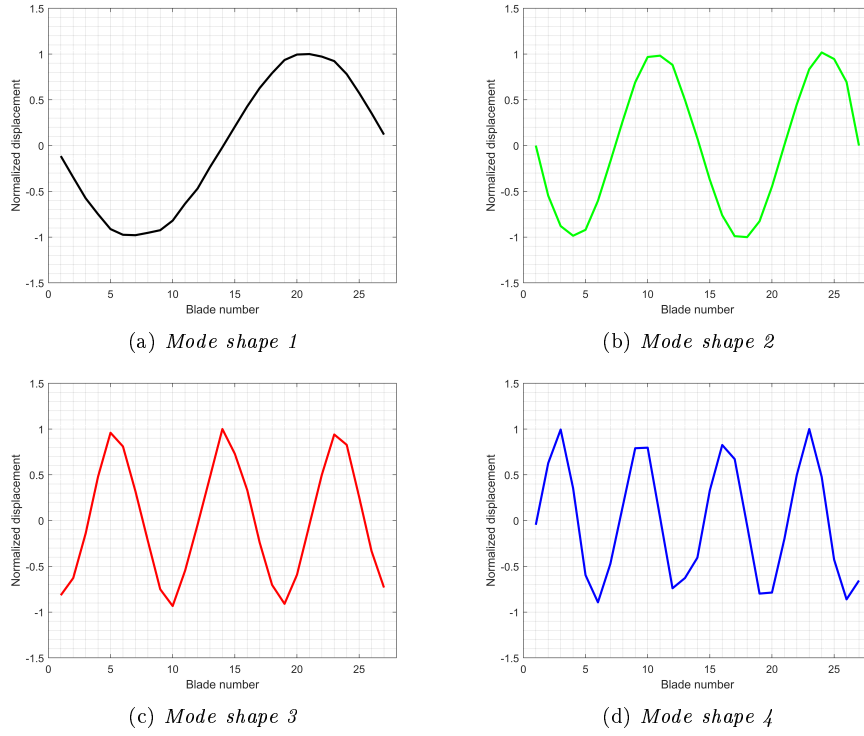


Figure 5.7: Sinusoidal patterns for some nodal diameters-mode shapes of the tuned bladed disk

### 5.2.2 Vibration of the mistuned bladed disk

As already explained, the tuned case is ideal. In reality, there are always small, random deviations in the blade properties. Mistuning affects the cyclic symmetry of the system, so that a single sector model can no longer be used to predict the vibration of the bladed disk.

Mistuned mode shapes are no longer pure nodal diameter modes and they show localization of the vibration within few blades. Vibration localization is well illustrated in Fig. 5.8. Because of this concentration of vibrational energy, some blades of the mistuned system are characterized by a certain deviation in vibration amplitudes and displacements compared to the tuned system. Displacement patterns of the mistuned system no longer follow a sinusoidal trend, but, in some modes, the maximum displacement amplitude tends to confine within few blades. Vibration localization level can be expressed with the following *vibration scatter* index:

$$\chi_m = \lambda \frac{\sum_{j=1}^N \bar{q}_j^2 - 1}{N - \lambda} \quad (5.1)$$

where

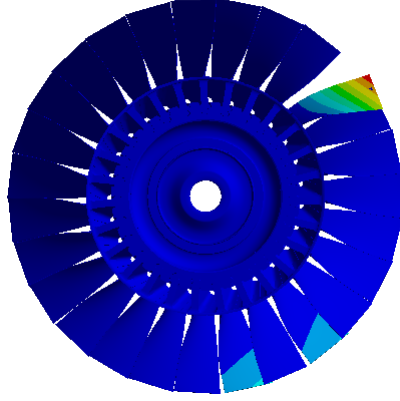


Figure 5.8: Localized mode shape of the mistuned bladed disk

$$\lambda = 1 \quad \text{if the bladed disk is vibrating in the mode shape } \frac{N+1}{2}$$

$$\lambda = 2 \quad \text{in the other cases}$$

$$\bar{q}_j = \frac{q_j}{q_{max}} \quad \text{is the normalized displacement of the } j\text{-th blade}$$

$$N = 27 \quad \text{is the number of blades}$$

For the ideal, tuned system this parameter assumes values close to 1. For a mistuned system, the more the vibration tends to localize, the closer the parameter is to 0.

Six copies of the *Modal Analysis System* need to be created. They only differ for the blades arrangements around the disk. Once solved all the simulations, the displacements file of the leading edge vertex of each blade can be exported and collected. Variations in normalized displacement of the mistuned systems from the tuned sinusoidal patterns for all modes are shown in Appendix C.

### 5.2.3 Modal analysis results

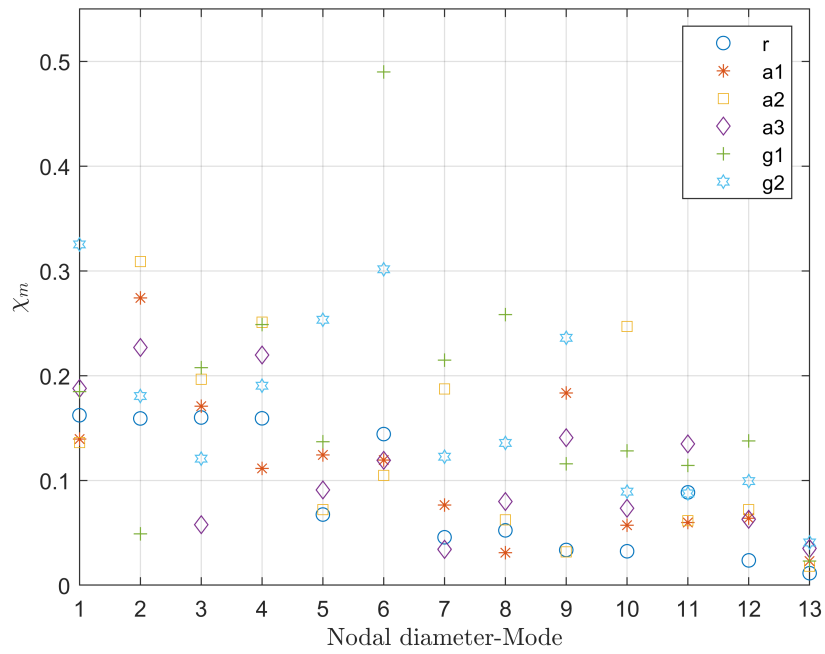
The next step is to calculate the index expressed in eq.(5.1) for each mode and for each blades arrangement. The resulting values are then plotted versus nodal diameter-modes in Fig. 5.9.

As already anticipated, the first modes are the most dangerous in vibration and fatigue terms. Taking into account this fact, it is possible to narrow the field to the first mode shapes.

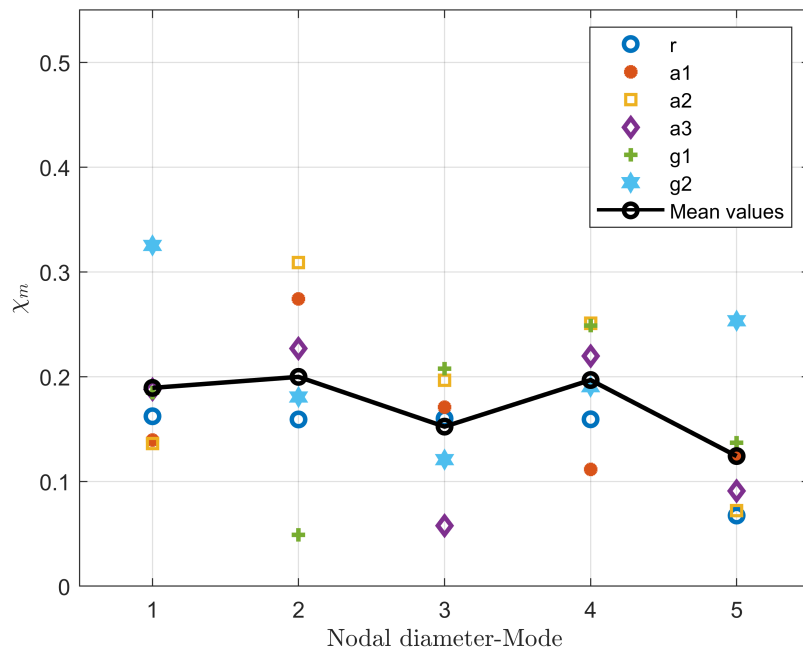
In order to find the “best” pattern, the worst possible situation will be taken into account. We can think the worst situation as the mode shape for which  $\chi_m$  mean value is the lowest. In Fig. 5.9b the line connecting mean values of the first five modes is plotted. The mean line has a minimum in the fifth mode shape, meaning that the “best” pattern has to be evaluated here.

In the selected mode it is clear that *g2* provides the best result in terms of displacement/vibration localization, with an index near to 0,3, followed by its similar pattern *g1*. As it was possible to foresee, the *r* arrangement, gives the worst result. However, also the alternated patterns don’t ensure high improvements related to the random arrangement, with  $\chi_m$  values less than 0,1.

In Fig. 5.10 are shown the bar charts of the  $\chi_m$  value for each blade arrangement evaluated in all mode-shapes.



(a) Complete plot



(b) First modes zoom

Figure 5.9: Vibration localization parameter vs nodal diameter-modes

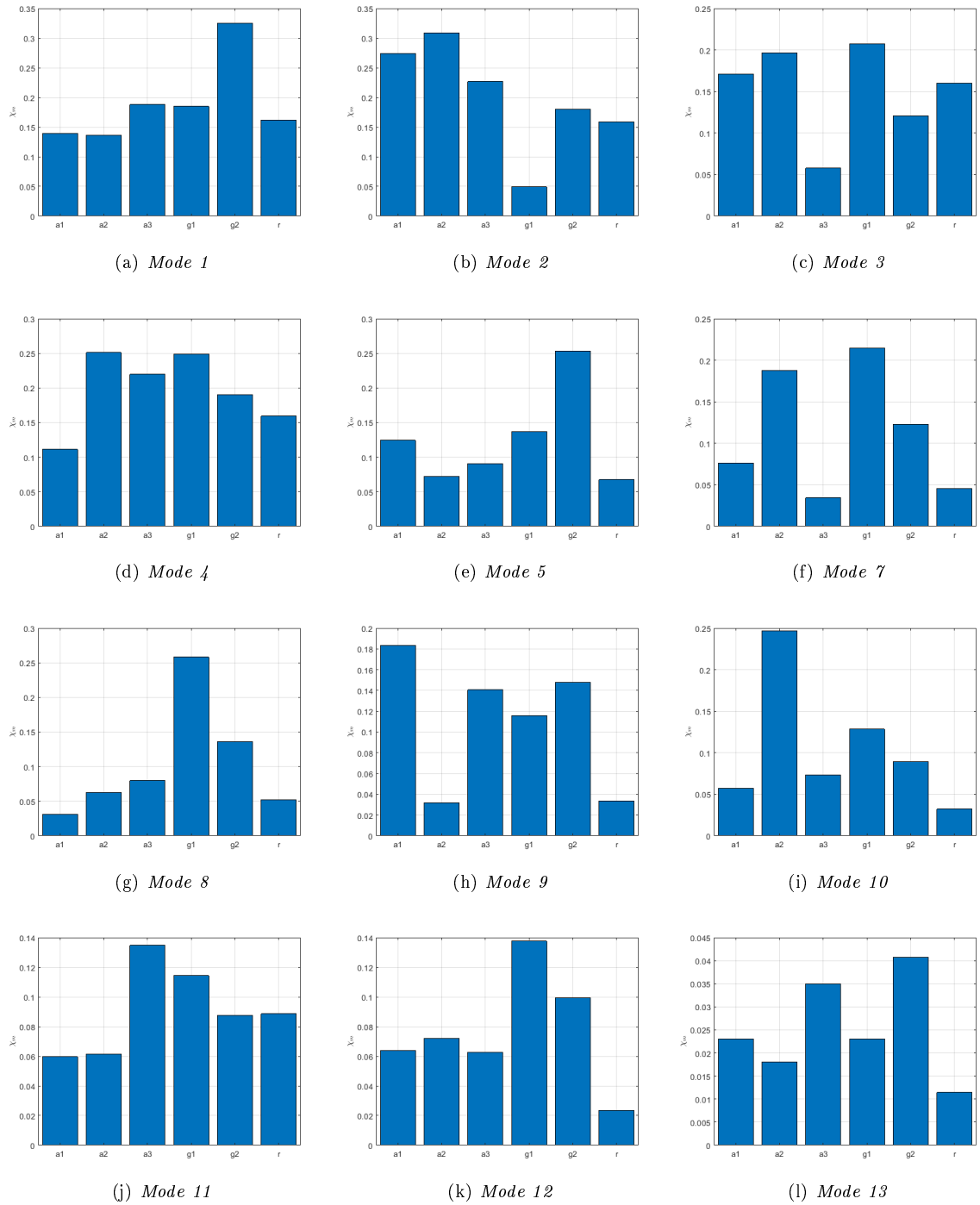


Figure 5.10: Vibration localization parameter bar charts

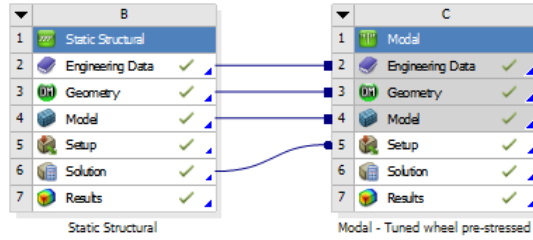


Figure 5.11: Linking of modal and structural analysis objects

## 5.3 Structural analysis and influence on stress scatter

The compressor rotor has been analyzed from a static point of view. The free-vibration modal analysis calculated natural frequencies and displacements due only to stiffness and mass characteristics of the system.

The engine compressor works by spinning at certain rotating velocities, thus it is needed to calculate frequencies (and mode shapes) of a prestressed structure. As explained in the paragraph 2.2.4, natural frequencies are related to rotating speed and, through the analysis of the *Campbell diagram*, it is possible to detect the most dangerous EOs in terms of resonance. After that, the EOs detected will be used for a *Transient Structural Analysis* in order to maximize the stress scatter.

### 5.3.1 Static structural linked to modal analysis and Campbell diagram

The procedure to do a prestressed modal analysis is essentially the same as a regular modal analysis, except that it is first needed to prestress the compressor rotor by doing a *Static Structural Analysis*:

1. a Static Structural analysis object is created in the Project Schematic of *ANSYS*. In the *Model* tab is sufficient to load the previous mesh from the modal analysis, apply the same constraints and provide a *Rotational Velocity* in the *Z* direction;
2. after duplicating the *Tuned Modal Analysis*, it is needed to drag and drop it onto the *Solution* tab of the Static Structural analysis object. This links the stress state from the static structural to the new Tuned Modal analysis object (Fig. 5.11).

The Campbell diagram can be built through the prestressed modal analysis by changing engine rotating speed and collecting frequencies values for each simulation. As shown in Tab. 1.1, engine nominal rotating speed is  $\Omega_n = 5005$  rpm. Values for null rotating speed are already available from the free-vibration modal analysis. Thus, to get the frequencies trend it is enough to run another simulation with rotating speed equal to  $\Omega = 0,6 \cdot \Omega_n$ . Once collected frequencies data and plotted EOs lines, the resonance diagram can be built. It is shown in Fig. 5.12.

Resonance occurs in those points where the EO line intersects the frequency curve. As explained in paragraph 2.2.3, only resonance at enduring speeds of the engine is dangerous, i.e. the nominal cruise speed of the engine or lower speeds. Thus, in the graph are highlighted intersections of EOs 3 and 4 with the frequency curve. They represents the most dangerous EOs because the compressor is more likely to protractedly work with those rotating speeds for which resonance could occur (critical speeds). These EOs will be analyzed for the following Transient Structural analysis.

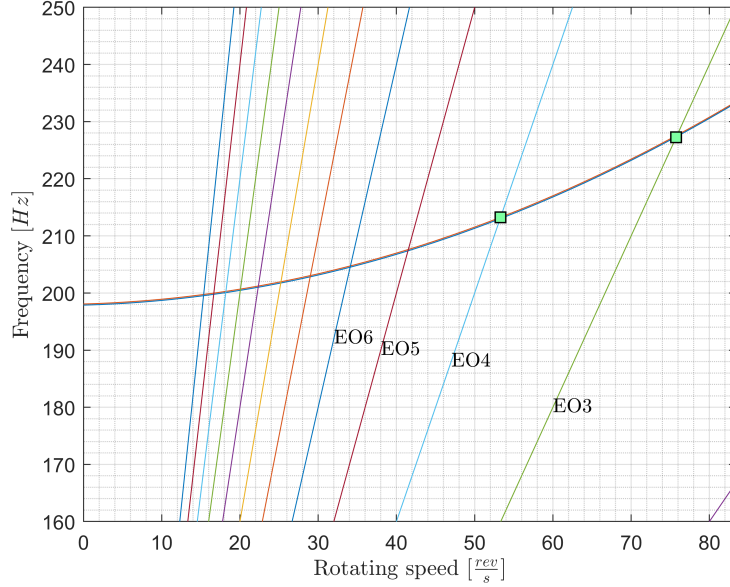


Figure 5.12: Campbell diagram of the NK-36ST LPC rotor

### 5.3.2 Transient structural analysis

A transient analysis, by definition, involves loads that are a function of time. For beginning, the *Transient Structural* analysis box can be selected and dragged in the WB Project Schematic.

This type of analysis is used to determine the dynamic response of the bladed disk under the action of the time-dependent forcing function defined in the paragraph 2.2.5. It is broken down in its three components in the following:

$$F_x = f_x \cos(k\varphi + \omega_k t) \quad (5.2)$$

$$F_y = f_y \cos(k\varphi + \omega_k t) \quad (5.3)$$

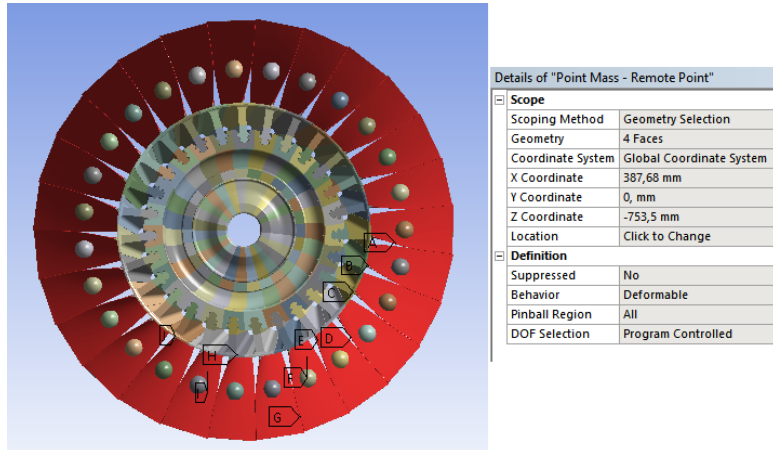
$$F_z = f_z \cos(k\varphi + \omega_k t) \quad (5.4)$$

where the force amplitudes  $f_x$ ,  $f_y$  and  $f_z$  come from the CFD calculation results, shown in Tab. 4.2. These exciting force components need to be applied to each blade, with its corresponding phase angle  $\varphi$ , expressed in radians. As already said in the previous paragraph the EO indices  $k$  chosen are 3 and 4.

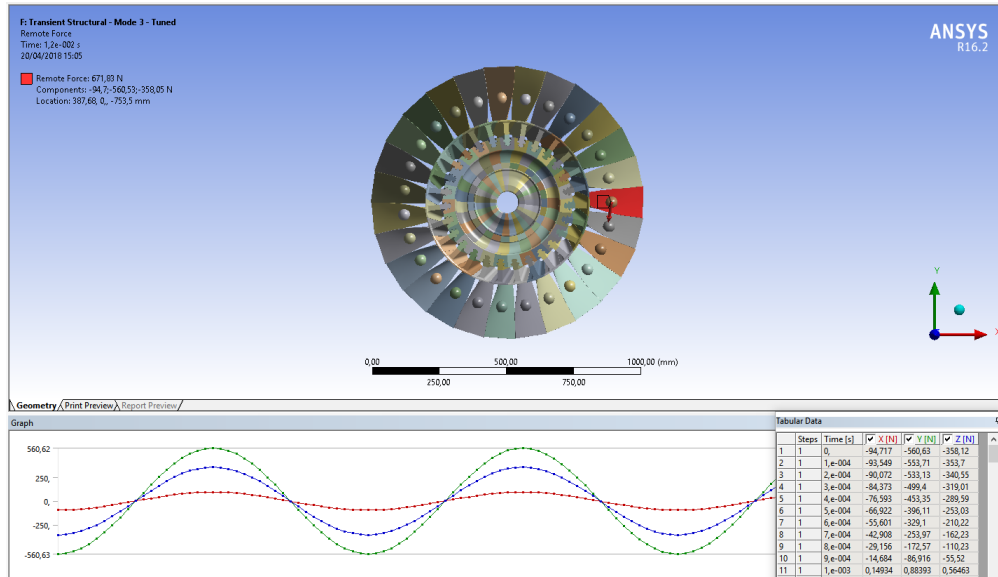
Regarding the frequency  $\omega_m$ , it is equal to the maximum rotating frequency (nominal rotating speed  $\Omega = 5005 \text{ rpm} = 83,417 \text{ Hz}$ ) of the compressor multiplied by the selected EO index (according to eq. 2.27):

$$\omega_{m=3} = 250,25 \text{ Hz} = 1572,37 \frac{\text{rad}}{\text{s}} \quad \omega_{m=4} = 333,67 \text{ Hz} = 2096,51 \frac{\text{rad}}{\text{s}}$$

Key points for a correct and accurate transient dynamic solution are the Initial Time Step (ITS) and Step End Time (SET) determination. According to what said in paragraph 2.2.5, the smaller is the ITS value, the greater will be the accuracy of results. Both time parameters are calculated by the following equations:



(a) Remote Points



(b) Remote Forces

Figure 5.13: Transient Structural analysis settings

$$\begin{aligned}
ITS_{(k=3)} &= \frac{1}{40 \cdot \omega_{(k=3)}} = 0,0001 \text{ s} \\
ITS_{(k=4)} &= \frac{1}{40 \cdot \omega_{(k=4)}} = 7,507 \cdot 10^{-5} \text{ s} \\
SET_{(k=3)} &= SET_{(k=4)} = \frac{1}{\Omega} = 0,012 \text{ s}
\end{aligned}$$

The force application point (in cylindrical coordinates  $\rho$ ,  $\phi$  and  $z$ ) of the first blade of the disk ( $\varphi = 0$ ) can be calculated through the torque expressions around  $Z$  and  $X$  axes (their values are written in Tab. 4.2):

$$\begin{aligned}
M_z = f_y \rho &\Rightarrow \rho = 387,68 \text{ mm} \\
M_x = f_y z &\Rightarrow z = 753,5 \text{ mm}
\end{aligned}$$

In *ANSYS* is easier to work with Cartesian coordinates, thus, all the other force application points for the remaining blades can be calculated through a simple transformation from cylindrical to Cartesian coordinates:

$$\begin{aligned}
x &= \rho \cos \phi \\
y &= \rho \sin \phi
\end{aligned}$$

A *Remote Point* needs to be inserted in each force application point with the Cartesian coordinates just calculated (Fig. 5.13a). After that, *Remote Forces* arrays (time varies from  $t = 0$  to  $t = SET$  with their own step time) are created and applied in each blade Remote Point (Fig. 5.13b). The simulation solves the equation (2.28).

### 5.3.3 Transient analysis results

Solution for transient analysis in *ANSYS* requires more time and memory than modal analysis. EOs 3 and 4 are analyzed separately. In each mode, the “best” pattern in terms of amplification factor, related to the tuned configuration, is found and investigated. The amplification factor, firstly defined by Whitehead in 1966, is expressed as:

$$\gamma = \frac{\max(u_{mistuned})}{\max(u_{tuned})} = \frac{1}{2}(1 + \sqrt{N})$$

where  $u_{mistuned}$  and  $u_{tuned}$  are the displacements calculated respectively in the mistuned pattern and in the tuned configuration in the  $Z$  (engine axis) direction of the leading edge vertex of each blade. Their values come from the *User Defined Results* imposed in the model setup. The lower the ratio, the better the arrangement will be. Commonly, the mistuned forced response remains far below the limit imposed by Whitehead because it is connected to a strong assumption: only one blade is mistuned by a particular amount. In general, common values of amplification factors range between 1 and 2 [12].

In Fig. 5.14 is shown the displacement trend over time: the step end time is the final solution while all the previous time steps results are needed for solution stabilization.

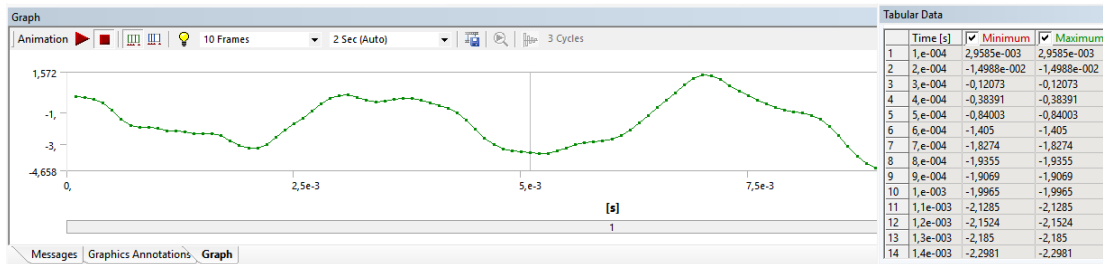


Figure 5.14: Displacement results of the first blade over time

Table 5.2:  $\gamma$  values for different arrangements in EO 3

r	a1	a2	a3	g1	g2
1,0459	1,0341	1,0298	1,0345	1,0341	1,0478

### Mode 3

Once collected results for each blade, the displacement pattern over disk circumference can be visualized and it is shown in Fig. 5.15. In the figure is no more visible a typical third mode pattern with three crests/wombs. In fact, differing from modal analysis results, in transient structural analysis a combination of different modes-shape may appear.

In Tab. 5.2 are displayed the amplification factor values for all the different blades arrangements. Giving a look to the these values, the *a2* layout is characterized by the lowest ratio and it can be selected as the “best” pattern for the third EO. However, arrangements *a1* and *g1*, give to the bladed disk good performances in terms of stress scatter. Finally, the blade pattern with highest amplification factor is the *g2*. In this pattern, the displacement amplification is maximum, even greater than in the random arrangement.

### Mode 4

Displacement pattern is shown in Fig. 5.16. Comparing it to the EO 3 pattern, it is clear how in the present case displacement amplitudes are much lower, meaning that increasing the engine order the bladed disk tends to stiffen and stress becomes more homogeneous along disk circumference.

Amplification factors for each blade pattern are displayed in Tab. 5.3. This time, the “best” pattern characterized by the lowest  $\gamma$  is *a2*, just followed by *a1* and *g1* arrangements, confirming to be good choices for homogenize the stress among blades, as in the previous case. The worst blade arrangement is again *g2*, endorsing that such blades layout is not suitable for this type of optimization.

Table 5.3:  $\gamma$  values for different arrangements in EO 4

r	a1	a2	a3	g1	g2
1,0611	1,0585	1,0579	1,0609	1,0600	1,0612

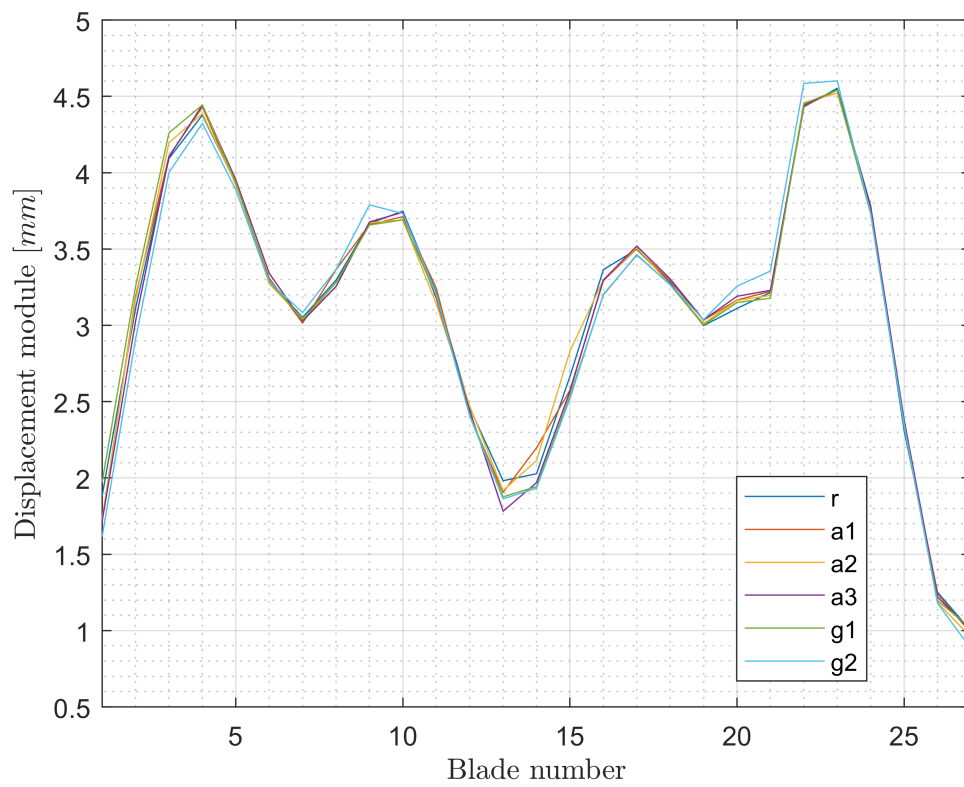


Figure 5.15: Displacement pattern along disk circumference for the EO 3

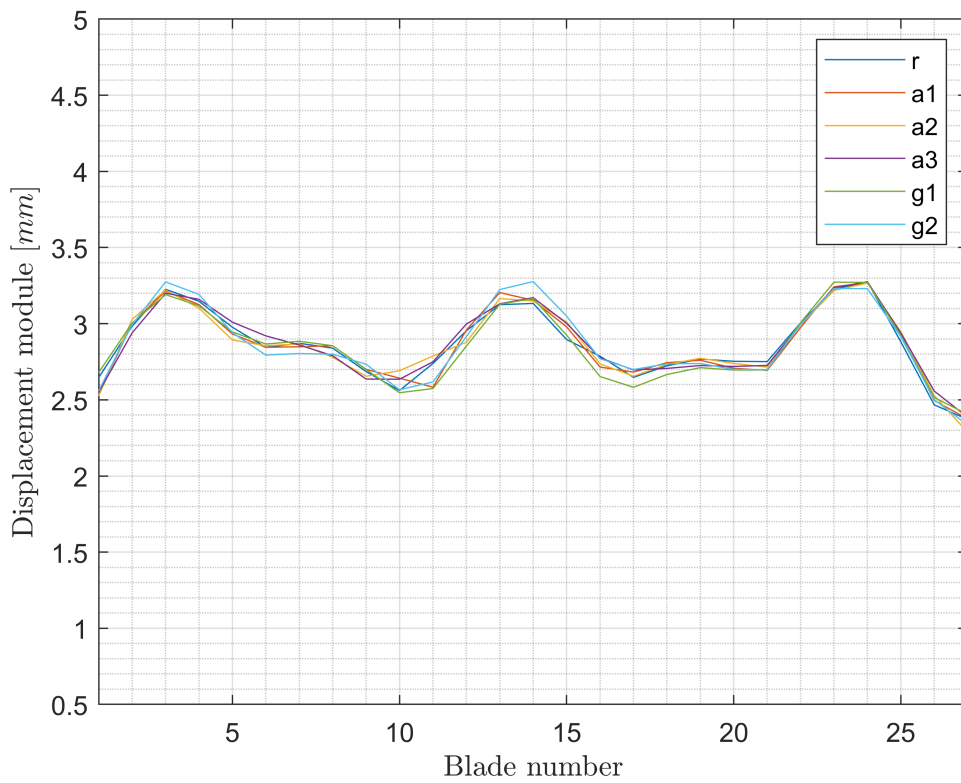


Figure 5.16: Displacement pattern along disk circumference for the EO 4

## Chapter 6

# Conclusions and recommendations for future work

In this final chapter, simulation results from both modal and transient analyzes are discussed and compared.

In the modal analysis, nodal diameter-mode shapes are clear and easily discoverable, at least for the first modes. In the mode shapes analysis of mistuned systems it was attempted to find a blade arrangement which could give good performances in terms of vibration localization. The more the vibration tends to localize within certain blades groups the greater is the attitude of the system to suffer of premature HCF problems. Mistuning cannot be avoided, thus different layouts of the same mistuned blades population have been tried and simulated in order to find out which is the pattern that gives best results. Vibration localization index  $\chi_m$  has been plotted versus nodal diameter-modes and its mean values have been calculated for each mode shape. The minimum of these values is analyzed in order to select the best layout in the worst possible situation. Highest  $\chi_m$  values have been achieved with the *g2* arrangement. Displacement patterns displayed in Appendix C show this feature, presenting a smoother trend and more scattered displacement peaks.

Transient analysis deals with the bladed disk in a more complex way, from a dynamical point of view. In this case, the forcing function is a harmonic which amplitude comes from the force components calculated in the CFD analysis. From the Campbell resonance diagram two EOs have been choosed: 3 and 4. The aerodynamic time dependant forces are applied to the blades, time steps and solution step end time are calculated. Displacement results at the step end time are then collected and analyzed. This time a new index, the amplification factor, is used to compare the effectiveness of each arrangement. It takes into account the ratio between maximum displacements in mistuned layouts and the maximum displacement obtained in the tuned, ideal configuration. Both for mode 3 and mode 4 the lower values of the amplification factors are obtained for the alternated arrangements *a2* and *a1*, while the remaining layouts provide higher values of that ratio, meaning that stress is not uniformly distributed as in the other arrangements.

From all these results can be extrapolated an important conclusion: although mistuning cannot be avoided, some expedients, like rearrange mistuned blades, can be applied. This work showed in a certain way that arranging blades with minimum stiffness gradient from one blade to its neighboring can give good results in terms of vibration localization in static analysis. While applying a time-dependant forcing function to the rotating system gives different results. Alternated layouts (low/high stiffness) provide better results than the “E gradient” designs.

Nevertheless, it should also be taken into account that these remarks and recommendations can be applied just to similar designs.

# Appendix A

## Mesh parameters

Influence of ER										
Mesh	Pressure Side	Suction Side	Width1	Width2	Width3	Width1	Width2	Width3	O-layer	Inlet
Mesh_b2b0_ER1.2	53	73	13	17	25	13	17	21	21	21
Mesh_b2b0_ER1.4	53	73	13	17	25	13	17	21	21	21
Mesh_b2b0_ER1.6	53	73	13	17	25	13	17	21	21	21
Mesh_b2b0_ER1.8	53	73	13	17	25	13	17	21	21	21
Mesh	Suction Side	Pressure Side	Width1	Width2	Width3	Width1	Width2	Width3	O-layer	Inlet
Mesh_b2b0_ER1.2	73	53	13	17	25	9	17	25	21	9
Mesh_b2b0_ER1.4	73	53	13	17	25	9	17	25	21	9
Mesh_b2b0_ER1.6	73	53	13	17	25	9	17	25	21	9
Mesh_b2b0_ER1.8	73	53	13	17	25	9	17	25	21	9
Influence of MR										
Mesh	Pressure Side	Suction Side	Width1	Width2	Width3	Width1	Width2	Width3	O-layer	Inlet
Mesh_b2b0_MR1000	53	73	13	17	25	13	17	21	21	21
Mesh_b2b0_MR500	53	73	13	17	25	13	17	21	21	21
Mesh_b2b0_MR200	53	73	13	17	25	13	17	21	21	21
Mesh_b2b0_MR2000	53	73	13	17	25	13	17	21	21	21
Mesh	Suction Side	Pressure Side	Width1	Width2	Width3	Width1	Width2	Width3	O-layer	Inlet
Mesh_b2b0_MR1000	73	53	13	17	25	9	17	25	21	9
Mesh_b2b0_MR500	73	53	13	17	25	9	17	25	21	9
Mesh_b2b0_MR200	73	53	13	17	25	9	17	25	21	9
Mesh_b2b0_MR2000	73	53	13	17	25	9	17	25	21	9
Influence of y+										
Mesh	Pressure Side	Suction Side	Width1	Width2	Width3	Width1	Width2	Width3	O-layer	Inlet
Mesh_b2b0_y1	53	73	13	17	25	13	17	21	21	21
Mesh_b2b0_y3	53	73	13	17	25	13	17	21	21	21
Mesh_b2b0_y7	53	73	13	17	25	13	17	21	21	21
Mesh_b2b0_y05	53	73	13	17	25	13	17	21	21	21
Mesh	Suction Side	Pressure Side	Width1	Width2	Width3	Width1	Width2	Width3	O-layer	Inlet
Mesh_b2b0_y1	73	53	13	17	25	9	17	25	21	9
Mesh_b2b0_y3	73	53	13	17	25	9	17	25	21	9
Mesh_b2b0_y7	73	53	13	17	25	9	17	25	21	9
Mesh_b2b0_y05	73	53	13	17	25	9	17	25	21	9

Figure A.1: FP mesh parameters

Influence of ER										
Mesh	Outlet	Edge Radius	ER_b2b	MR_FP	ER_FP	y+	Turb	FP	Midle,%	
Mesh_b2b0_ER1.2	13	17	1,2	1000	1,2	1	SA	105	11	Rotor
Mesh_b2b0_ER1.4	13	17	1,2	1000	1,4	1	SA	77	33	
Mesh_b2b0_ER1.6	13	17	1,2	1000	1,6	1	SA	61	40	
Mesh_b2b0_ER1.8	13	17	1,2	1000	1,8	1	SA	53	45	
Mesh	Outlet	Edge Radius	ER_b2b	MR_FP	ER_FP	y+	Turb	FP	Midle,%	
Mesh_b2b0_ER1.2	13	17	1,2	1000	1,2	1	SA	89	11	Stator
Mesh_b2b0_ER1.4	13	17	1,2	1000	1,4	1	SA	77	13	
Mesh_b2b0_ER1.6	13	17	1,2	1000	1,6	1	SA	45	37	
Mesh_b2b0_ER1.8	13	17	1,2	1000	1,8	1	SA	41	45	
Influence of MR										
Mesh	Outlet	Edge Radius	ER_b2b	MR_FP	ER_FP	y+	Turb	FP	Midle,%	
Mesh_b2b0_MR1000	13	17	1,2	1000	1,2	1	SA	105	11	Rotor
Mesh_b2b0_MR500	13	17	1,2	500	1,2	1	SA	113	22	
Mesh_b2b0_MR200	13	17	1,2	200	1,2	1	SA	129	40	
Mesh_b2b0_MR2000	13	17	1,2	2000	1,2	1	SA	85	5	
Mesh	Outlet	Edge Radius	ER_b2b	MR_FP	ER_FP	y+	Turb	FP	Midle,%	
Mesh_b2b0_MR1000	13	17	1,2	1000	1,2	1	SA	89	11	Stator
Mesh_b2b0_MR500	13	17	1,2	500	1,2	1	SA	93	25	
Mesh_b2b0_MR200	13	17	1,2	200	1,2	1	SA	113	40	
Mesh_b2b0_MR2000	13	17	1,2	2000	1,2	1	SA	73	5	
Influence of y+										
Mesh	Outlet	Edge Radius	ER_b2b	MR_FP	ER_FP	y+	Turb	FP	Midle,%	
Mesh_b2b0_y1	13	17	1,2	1000	1,2	1	SA	105	11	Rotor
Mesh_b2b0_y3	13	17	1,2	1000	1,2	3	SA	105	11	
Mesh_b2b0_y7	13	17	1,2	1000	1,2	7	SA	105	11	
Mesh_b2b0_y05	13	17	1,2	1000	1,2	0,5	SA	105	11	
Mesh	Outlet	Edge Radius	ER_b2b	MR_FP	ER_FP	y+	Turb	FP	Midle,%	
Mesh_b2b0_y1	13	17	1,2	1000	1,2	1	SA	89	11	Stator
Mesh_b2b0_y3	13	17	1,2	1000	1,2	3	SA	89	11	
Mesh_b2b0_y7	13	17	1,2	1000	1,2	7	SA	89	11	
Mesh_b2b0_y05	13	17	1,2	1000	1,2	0,5	SA	89	11	

Figure A.2: FP mesh parameters

Influence of mesh density										
Mesh	Pressure Side	Suction Side	Width1	Width2	Width3	Width1	Width2	Width3	O-layer	Inlet
Mesh_b2b-1	41	57	9	17	17	9	17	17	21	17
Mesh_b2b0	53	73	13	17	25	13	17	21	21	21
Mesh_b2b1	89	109	21	25	37	25	25	29	21	29
Mesh_b2b2	137	165	29	33	49	33	33	41	21	41
Mesh_b2b3	197	249	41	41	73	41	41	61	21	61
Mesh_b2b4	289	373	61	57	109	57	57	93	21	93
Mesh	Suction Side	Pressure Side	Width1	Width2	Width3	Width1	Width2	Width3	O-layer	Inlet
Mesh_b2b-1	57	41	9	17	17	9	17	17	21	9
Mesh_b2b0	73	53	13	17	25	9	17	25	21	9
Mesh_b2b1	109	77	21	25	29	13	25	29	21	13
Mesh_b2b2	165	105	33	33	33	29	33	33	21	29
Mesh_b2b3	249	165	49	41	41	37	41	41	21	37
Mesh_b2b4	373	245	73	57	61	57	57	61	21	57
Influence of O-layer										
Mesh	Outlet	Suction Side	Width1	Width2	Width3	Width1	Width2	Width3	O-layer	Inlet
Mesh_Olayer_0	13	73	13	17	25	13	17	21	21	21
Mesh_Olayer_-1	13	73	13	17	25	13	17	21	17	21
Mesh_Olayer_-2	13	73	13	17	25	13	17	21	13	21
Mesh_Olayer_1	13	73	13	17	25	13	17	21	25	21
Mesh_b2b0_O_2	13	73	13	17	25	13	17	21	29	21
Mesh	Outlet	Pressure Side	Width1	Width2	Width3	Width1	Width2	Width3	O-layer	Inlet
Mesh_Olayer_0	13	53	13	17	25	9	17	25	21	9
Mesh_Olayer_-1	13	53	13	17	25	9	17	25	17	9
Mesh_Olayer_-2	13	53	13	17	25	9	17	25	13	9
Mesh_Olayer_1	13	53	13	17	25	9	17	25	25	9
Mesh_Olayer_1	13	53	13	17	25	9	17	25	29	9
Influence of ER_b2b										
Mesh	Pressure Side	Suction Side	Width1	Width2	Width3	Width1	Width2	Width3	O-layer	Inlet
Mesh_b2b0_ER_b2b1.2	73	53	13	17	25	21	17	13	21	21
Mesh_b2b0_ER_b2b1.4	73	53	13	17	25	21	17	13	21	21
Mesh_b2b0_ER_b2b1.6	73	53	13	17	25	21	17	13	21	21
Mesh_b2b0_ER_b2b1.8	73	53	13	17	25	21	17	13	21	21
Mesh	Suction Side	Pressure Side	Width1	Width2	Width3	Width1	Width2	Width3	O-layer	Inlet
Mesh_b2b0_ER_b2b1.2	73	53	13	17	25	9	17	25	21	9
Mesh_b2b0_ER_b2b1.4	73	53	13	17	25	9	17	25	21	9
Mesh_b2b0_ER_b2b1.6	73	53	13	17	25	9	17	25	21	9
Mesh_b2b0_ER_b2b1.8	73	53	13	17	25	9	17	25	21	9

Figure A.3: B2B mesh parameters

Influence of mesh density									
Mesh	Outlet	Edge Radius	ER_b2b	MR_FP	ER_FP	y+	Turb	FP	Midle, %
Mesh_b2b-1	9	17	1,2	1000	1,2	1	SA	105	11
Mesh_b2b0	13	17	1,2	1000	1,2	1	SA	105	11
Mesh_b2b1	21	25	1,2	1000	1,2	1	SA	105	11
Mesh_b2b2	29	33	1,2	1000	1,2	1	SA	105	11
Mesh_b2b3	41	41	1,2	1000	1,2	1	SA	105	11
Mesh_b2b4	61	57	1,2	1000	1,2	1	SA	105	11
Mesh	Outlet	Edge Radius	ER_b2b	MR_FP	ER_FP	y+	Turb	FP	Midle, %
Mesh_b2b-1	13	17	1,2	1000	1,2	1	SA	89	11
Mesh_b2b0	13	17	1,2	1000	1,2	1	SA	89	11
Mesh_b2b1	17	25	1,2	1000	1,2	1	SA	89	11
Mesh_b2b2	29	33	1,2	1000	1,2	1	SA	89	11
Mesh_b2b3	41	41	1,2	1000	1,2	1	SA	89	11
Mesh_b2b4	61	57	1,2	1000	1,2	1	SA	89	11
Influence of O-layer									
Mesh	Outlet	Edge Radius	ER_b2b	MR_FP	ER_FP	y+	Turb	FP	Midle, %
Mesh_Olayer_0	13	17	1,2	1000	1,2	1	SA	105	11
Mesh_Olayer_-1	13	17	1,2	1000	1,2	1	SA	105	11
Mesh_Olayer_-2	13	17	1,2	1000	1,2	1	SA	105	11
Mesh_Olayer_1	13	17	1,2	1000	1,2	1	SA	105	11
Mesh_b2b0_O_2	13	17	1,2	1000	1,2	1	SA	105	11
Mesh	Outlet	Edge Radius	ER_b2b	MR_FP	ER_FP	y+	Turb	FP	Midle, %
Mesh_Olayer_0	13	17	1,2	1000	1,2	1	SA	89	11
Mesh_Olayer_-1	13	17	1,2	1000	1,2	1	SA	89	11
Mesh_Olayer_-2	13	17	1,2	1000	1,2	1	SA	89	11
Mesh_Olayer_1	13	17	1,2	1000	1,2	1	SA	89	11
Mesh_Olayer_1	13	17	1,2	1000	1,2	1	SA	89	11
Influence of ER_b2b									
Mesh	Outlet	Edge Radius	ER_b2b	MR_FP	ER_FP	y+	Turb	FP	Midle, %
Mesh_b2b0_ER_b2b1.2	13	17	1,2	1000	1,2	1	SA	105	11
Mesh_b2b0_ER_b2b1.4	13	17	1,1	1000	1,2	1	SA	105	11
Mesh_b2b0_ER_b2b1.6	13	17	1,3	1000	1,2	1	SA	105	11
Mesh_b2b0_ER_b2b1.8	13	17	1,4	1000	1,2	1	SA	105	11
Mesh	Outlet	Edge Radius	ER_b2b	MR_FP	ER_FP	y+	Turb	FP	Midle, %
Mesh_b2b0_ER_b2b1.2	13	17	1,2	1000	1,2	1	SA	89	11
Mesh_b2b0_ER_b2b1.4	13	17	1,1	1000	1,2	1	SA	89	11
Mesh_b2b0_ER_b2b1.6	13	17	1,3	1000	1,2	1	SA	89	11
Mesh_b2b0_ER_b2b1.8	13	17	1,4	1000	1,2	1	SA	89	11

Figure A.4: B2B mesh parameters

# Appendix B

## Blade section coordinates

In this appendix the blade data of the first compressor rotor stage are presented. For each section at given radius from the axis the coordinates are given in tab. B.2. The shroud coordinates at changing radius are also given in tab. B.1.

SHROUD		
x	y	z
0	0	253,6
15	0	259,64
30	0	265,71
45	0	271,71
60	0	277,74
75	0	283,78
85	0	287,8
100	0	293,6
115	0	299
130	0	303,7
145	0	308
146,8	0	308,5

Figure B.1: Shroud coordinates

A1-A1			A3-A3			A5-A5			A8-A8			A10-A10		
suction side			suction side			suction side			suction side			suction side		
x	y	z	x	y	z	x	y	z	x	y	z	x	y	z
-79,64	-14,92	505	-78,5	-11,3	465	-77,6	-3,37	385	-74,68	11,06	290	-70,66	18,6	250
-74,94	-13,21	505	-73,86	-9,74	465	-72,96	-2,02	385	-69,8	12,21	290	-65,55	19,57	250
-68,65	-11,01	505	-67,66	-7,75	465	-66,78	-0,35	385	-63,3	13,52	290	-58,8	20,58	250
-59,99	-8,15	505	-59,12	-5,19	465	-58,26	1,7	385	-54,41	14,87	290	-49,64	21,41	250
-48,13	-4,54	505	-47,41	-2,03	465	-46,61	4,03	385	-42,38	15,87	290	-37,45	21,53	250
-36,21	-1,26	505	-35,66	0,74	465	-34,93	5,8	385	-30,54	15,9	290	-25,67	20,47	250
-24,23	1,68	505	-23,85	3,12	465	-23,24	7,02	385	-18,91	14,95	290	-14,38	18,24	250
-12,21	4,3	505	-12	5,12	465	-11,55	7,66	385	-7,58	12,99	290	-3,68	14,82	250
-0,12	6,59	505	-0,1	6,74	465	0,14	7,71	385	3,42	10,01	290	6,34	10,2	250
12,01	8,57	505	11,85	7,98	465	11,781	7,17	385	14	5,98	290	15,58	4,39	250
24,21	10,24	505	23,84	8,84	465	23,45	6,03	385	24,09	0,88	290	23,96	-2,62	250
36,46	11,61	505	35,87	9,34	465	35,05	4,28	385	33,59	-5,34	290	31,41	-10,82	250
48,77	12,7	505	47,94	9,48	465	46,6	1,9	385	42,41	-12,67	290	37,89	-20,17	250
61,13	13,51	505	60,05	9,28	465	58,08	-1,11	385	50,47	-21,15	290	43,42	-30,62	250
70,24	13,93	505	68,95	8,92	465	66,45	-3,73	385	55,85	-28,08	290	46,9	-38,93	250
76,88	14,16	505	75,44	8,54	465	72,5	-5,85	385	59,47	-33,5	290	49,16	-45,28	250
81,87	14,28	505	80,31	8,2	465	77,02	-7,56	385	62,01	-37,77	290	50,72	-50,2	250
pressure side			pressure side			pressure side			pressure side			pressure side		
x	y	z	x	y	z	x	y	z	x	y	z	x	y	z
82,08	13,12	505	-78,32	-12,68	465	-77,58	-4,84	385	-75,04	9,48	290	-71,25	17,01	250
77,21	12,31	505	-73,58	-11,86	465	-72,95	-4,39	385	-70,44	9,5	290	-66,61	16,79	250
70,72	11,23	505	-67,26	-10,79	465	-66,77	-3,84	385	-64,32	9,4	290	-60,48	16,34	250
61,8	9,74	505	-58,57	-9,36	465	-58,27	-3,18	385	-55,92	9,03	290	-52,14	15,4	250
49,65	7,72	505	-46,72	-7,5	465	-46,67	-2,44	385	-44,55	8,07	290	-41	13,51	250
37,51	5,69	505	-34,85	-5,74	465	-35,06	-1,92	385	-33,3	6,56	290	-30,16	10,91	250
25,37	3,64	505	-22,97	-4,08	465	-23,44	-1,61	385	-22,22	4,49	290	-19,69	7,57	250
13,25	1,55	505	-11,08	-2,51	465	-11,82	-1,53	385	-11,32	1,84	290	-9,63	3,5	250
1,14	-0,57	505	0,83	-1,03	465	-0,2	-1,68	385	-0,66	-1,41	290	-0,05	-1,32	250
-10,96	-2,74	505	12,74	0,36	465	11,41	-2,08	385	9,73	-5,27	290	9	-6,9	250
-23,05	-4,97	505	24,67	1,67	465	23,02	-2,71	385	19,81	-9,77	290	17,49	-13,23	250
-35,13	-7,26	505	36,61	2,91	465	34,61	-3,59	385	29,52	-14,9	290	25,4	-20,27	250
-47,21	-9,62	505	48,55	4,09	465	46,18	-4,71	385	38,82	-20,67	290	32,73	-28,01	250
-59,28	-12,06	505	60,51	5,22	465	57,73	-6,06	385	47,66	-27,08	290	39,52	-36,39	250
-68,13	-13,89	505	69,28	6,02	465	66,19	-7,2	385	53,84	-32,18	290	44,18	-42,89	250
-74,56	-15,24	505	75,66	6,6	465	72,32	-8,1	385	58,16	-36,1	290	47,42	-47,78	250
-79,39	-16,28	505	80,44	7,03	465	76,92	-8,81	385	61,31	-39,15	290	49,78	-51,54	250

Figure B.2: Blade sections coordinates

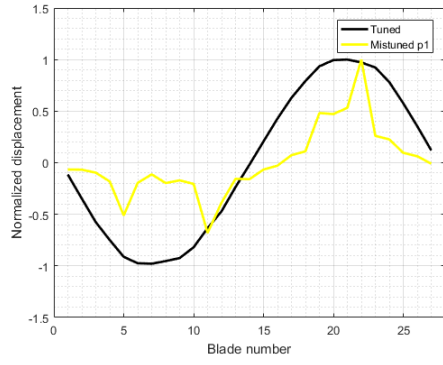
## Appendix C

# Displacement patterns of mistuned blades arrangements

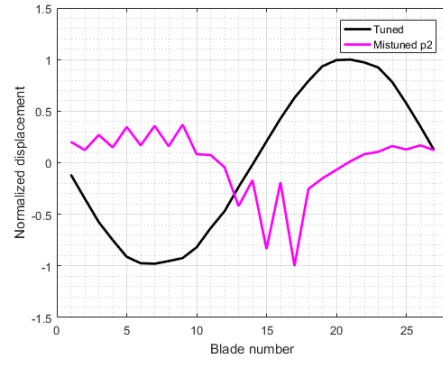
Plots representing normalized displacements of blades for each mode shape are shown in this appendix. The first mode shapes (from mode 1 to mode 5) are pretty clear and easily understandable. Until the tenth mode shape, crests and wombs of the sinusoidal tuned patterns are clearly visible and each mode is characterized by a number of crests/wombs equal to its own nodal diameter. For instance, the third mode is constituted by three crests (also three wombs if the first and the last halfwaves are considered as subsequent) (Fig. C.3).

Shifting the focus on mistuned patterns compared with their tuned counterparts, sinusoidal trends disappear, giving way to vibration localization on few blades. For a simple understanding let's consider the first mode plots. The random mistuned arrangement displayed in Fig. C.1a, shows how vibration tends to gather on blades 15, 11 and 22. Regarding the the arrangements  $a1$ ,  $a2$ ,  $a3$  and  $g1$ , some improvements are reached in terms of smoothness, even if vibration always seems to locate on 14-th to 18-th blades. A significant melioration in vibration characteristics is obtained with the  $g2$  arrangement: its pattern seems to be mirrored to the tuned one. Vibration localization parameter values, evaluated in Chapter 5 and shown in Fig. 5.9, just confirm what said, with the maximum value reached by the  $g2$  arrangement.

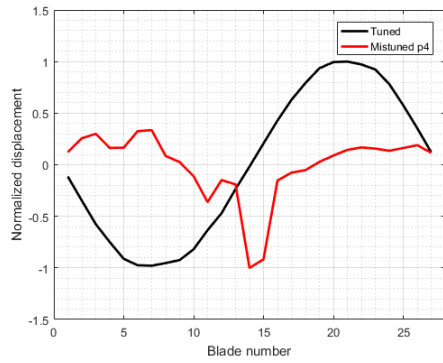
For the remaining mode shapes, with increasing number of crests and complexity, this type of analysis tends to be trickier than the first mode.



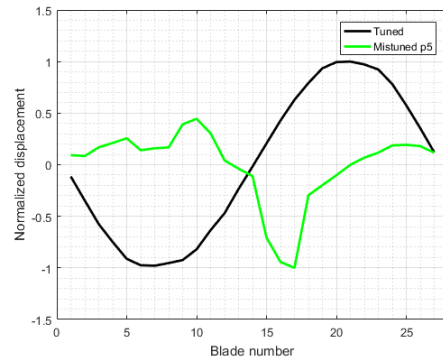
(a)  $r$



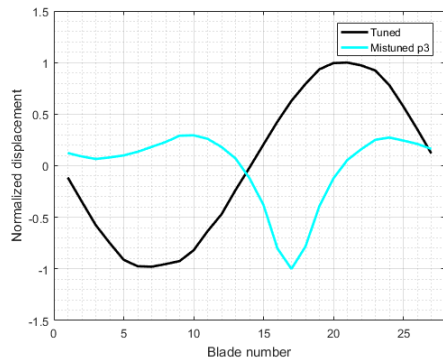
(b)  $a1$



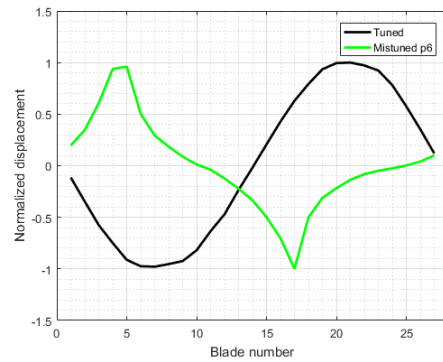
(c)  $a2$



(d)  $a3$

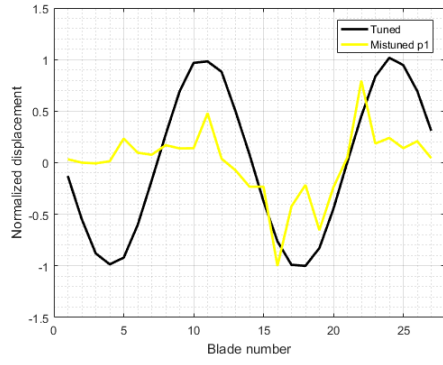


(e)  $g1$

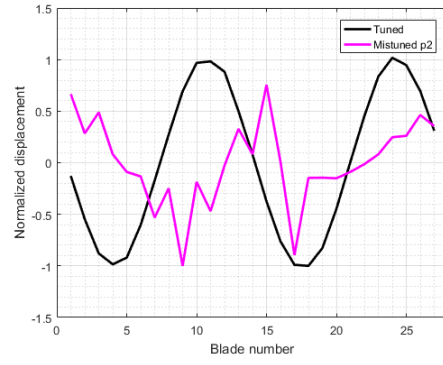


(f)  $g2$

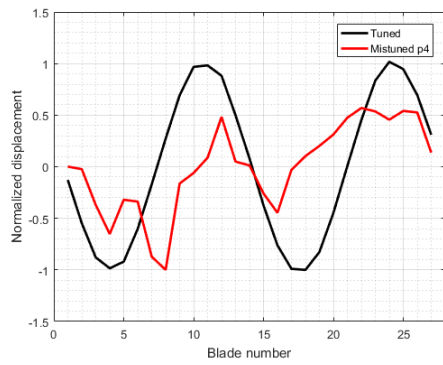
Figure C.1: Mode 1 variations in normalized displacements from tuned system for different mistuned patterns.



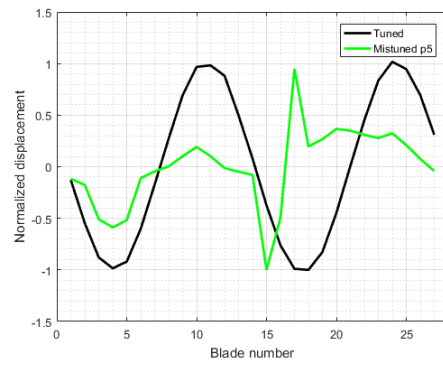
(a)  $r$



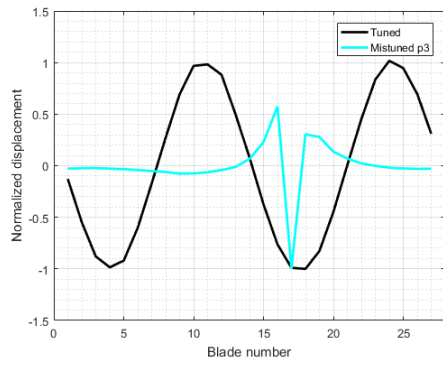
(b)  $a1$



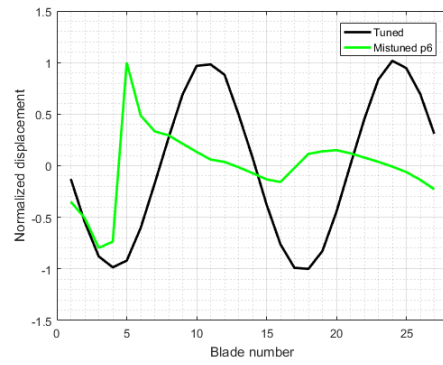
(c)  $a2$



(d)  $a3$

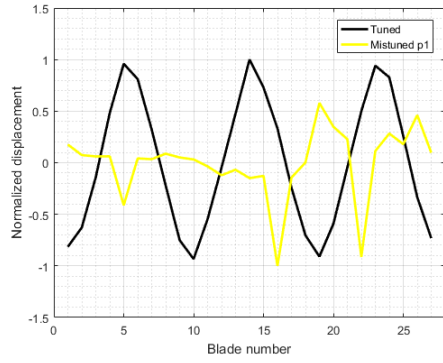


(e)  $g1$

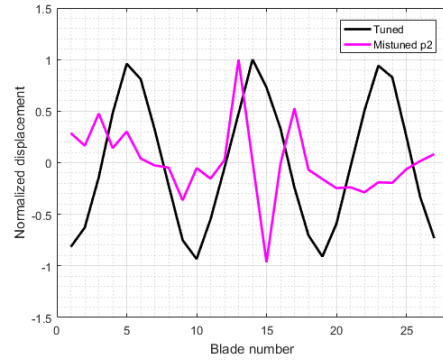


(f)  $g2$

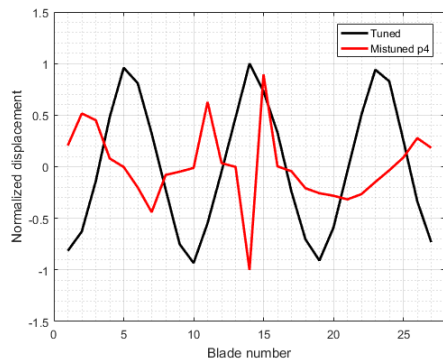
Figure C.2: Mode 2 variations in normalized displacements from tuned system for different mistuned patterns.



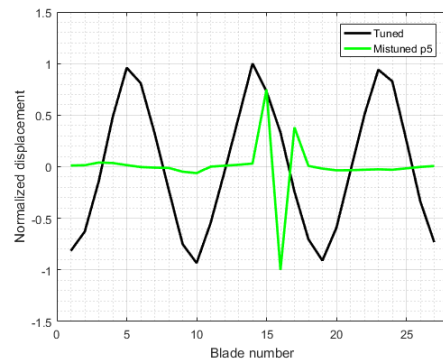
(a)  $r$



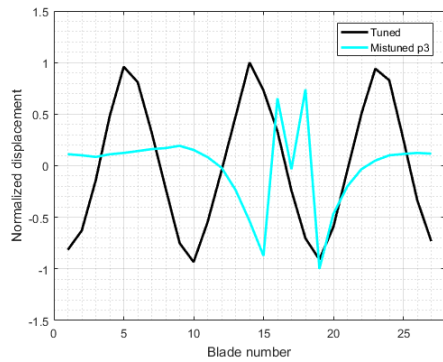
(b)  $a1$



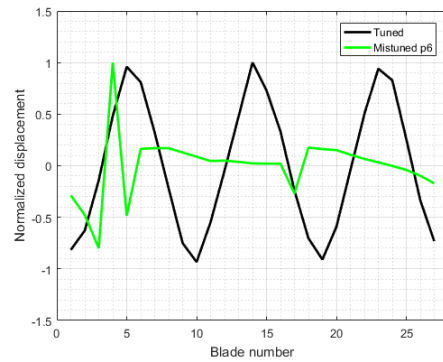
(c)  $a2$



(d)  $a3$

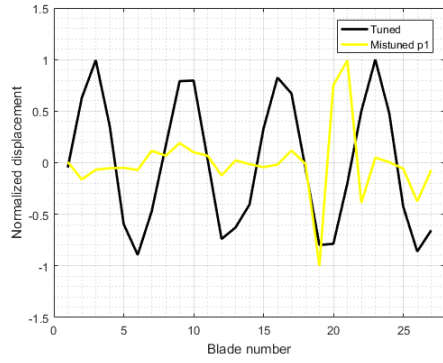


(e)  $g1$

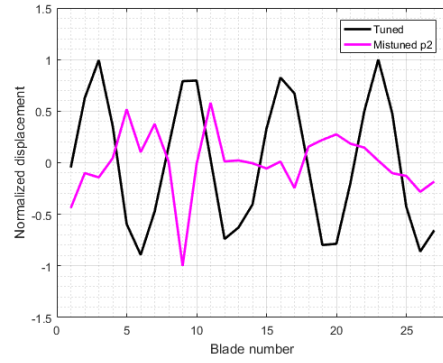


(f)  $g2$

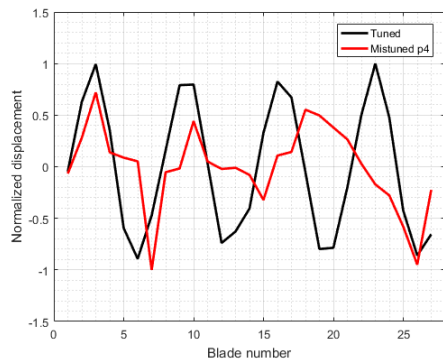
Figure C.3: Mode 3 variations in normalized displacements from tuned system for different mistuned patterns.



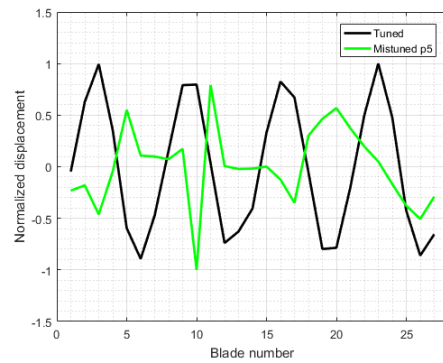
(a)  $r$



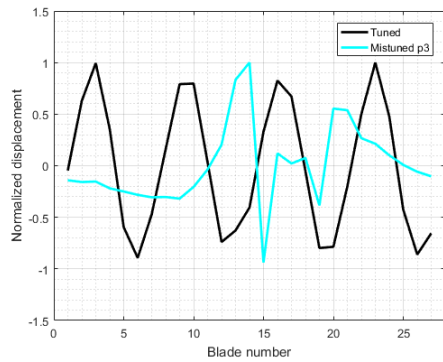
(b)  $a1$



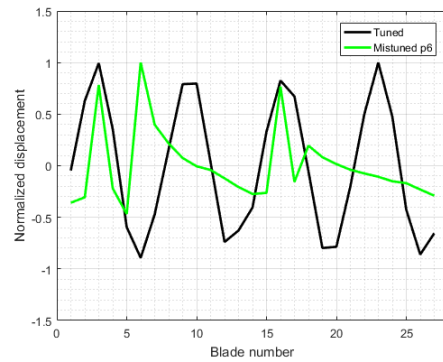
(c)  $a2$



(d)  $a3$

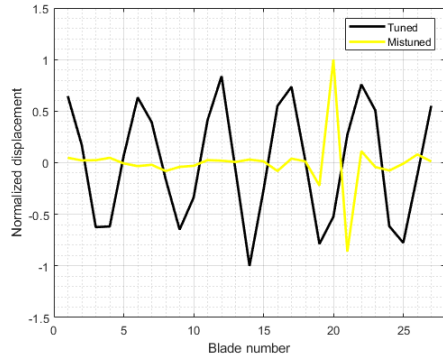


(e)  $g1$

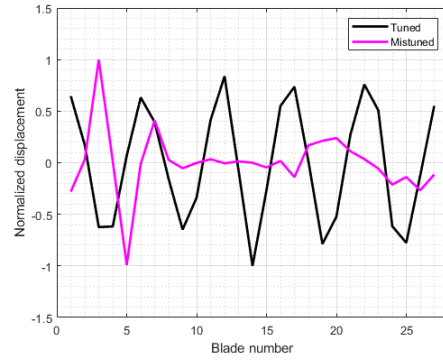


(f)  $g2$

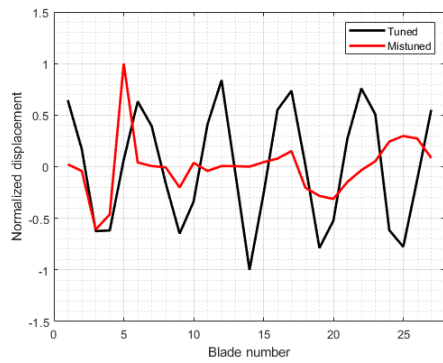
Figure C.4: Mode 4 variations in normalized displacements from tuned system for different mistuned patterns.



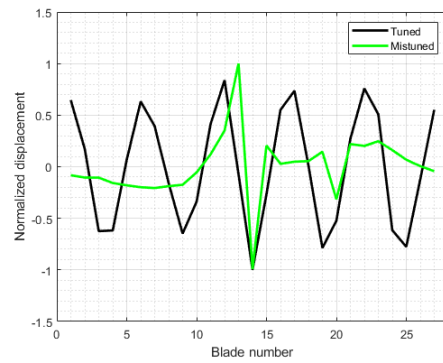
(a)  $r$



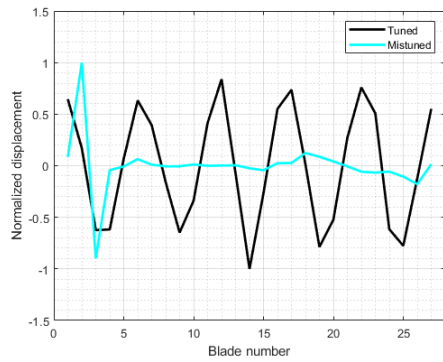
(b)  $a1$



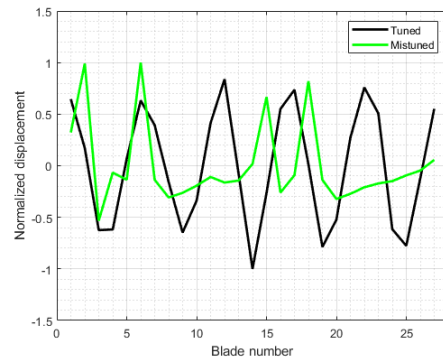
(c)  $a2$



(d)  $a3$

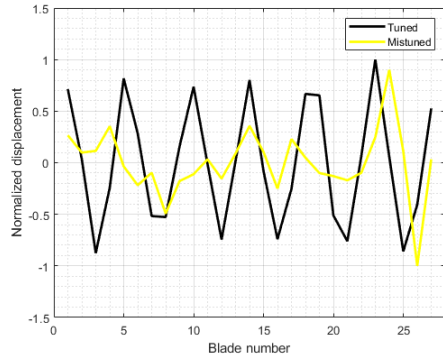


(e)  $g1$

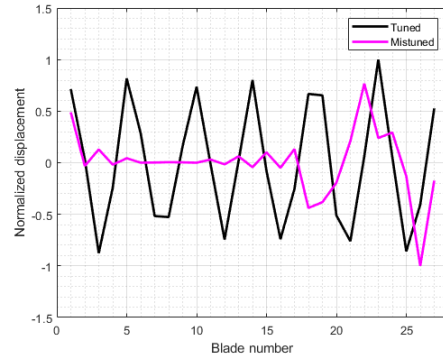


(f)  $g2$

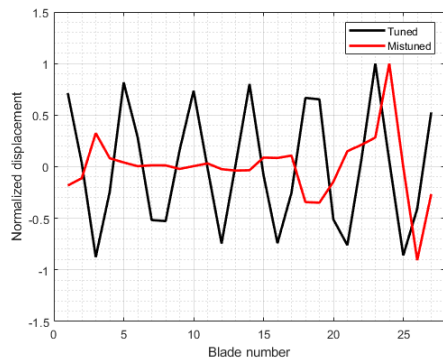
Figure C.5: Mode 5 variations in normalized displacements from tuned system for different mistuned patterns.



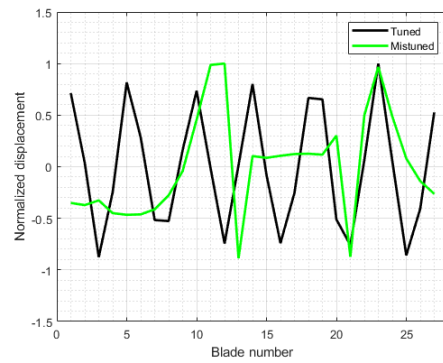
(a)  $r$



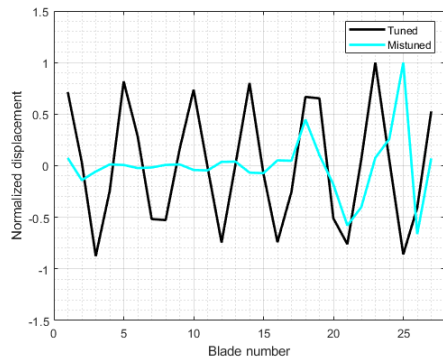
(b)  $a1$



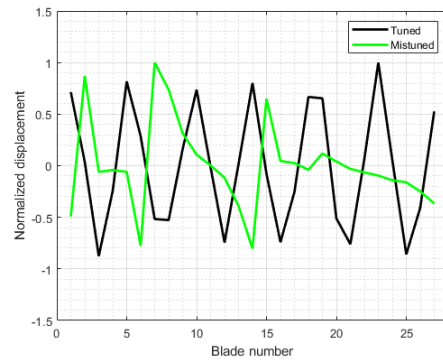
(c)  $a2$



(d)  $a3$

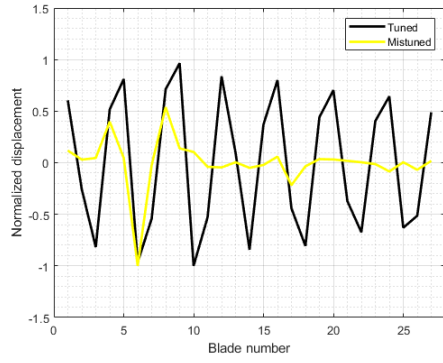


(e)  $g1$

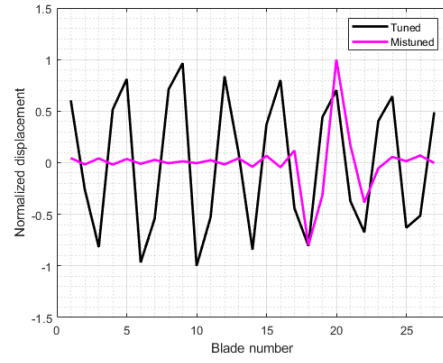


(f)  $g2$

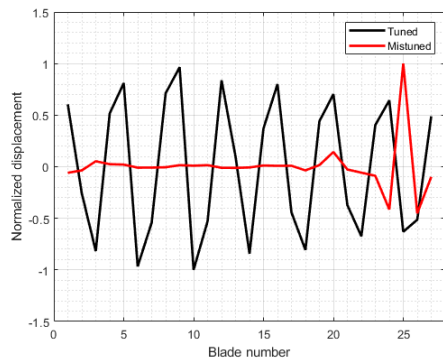
Figure C.6: Mode 6 variations in normalized displacements from tuned system for different mistuned patterns.



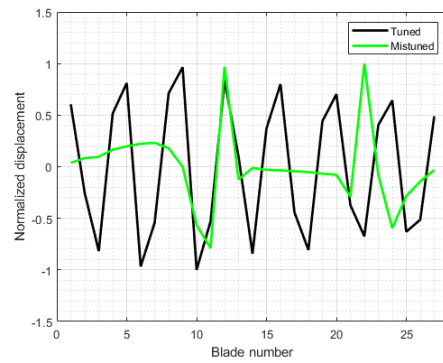
(a)  $r$



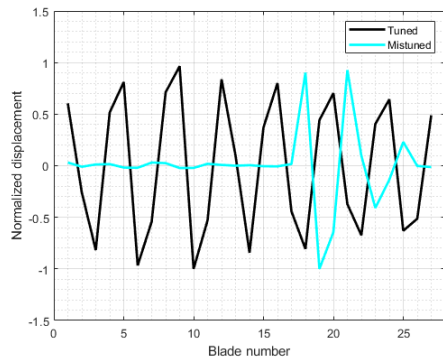
(b)  $a1$



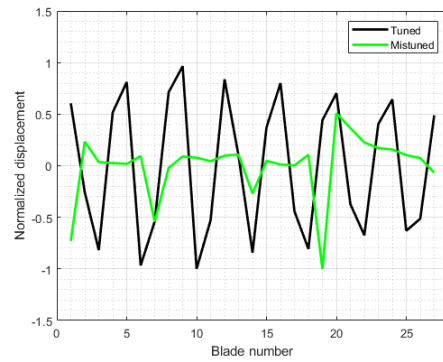
(c)  $a2$



(d)  $a3$

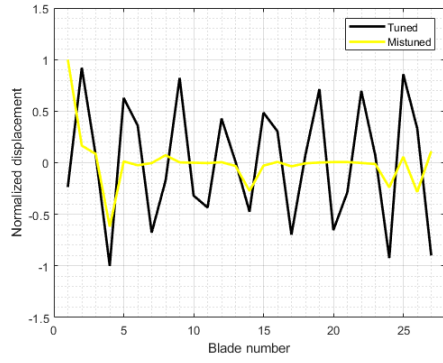


(e)  $g1$

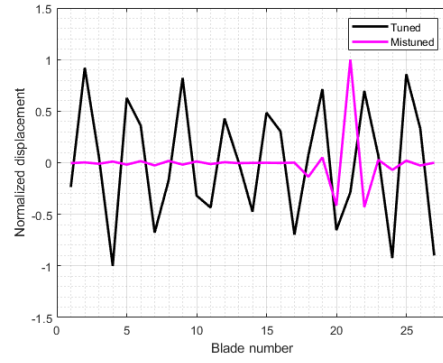


(f)  $g2$

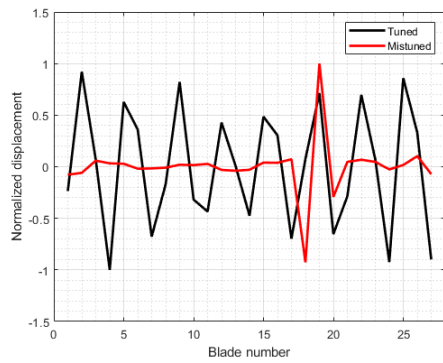
Figure C.7: Mode 7 variations in normalized displacements from tuned system for different mistuned patterns.



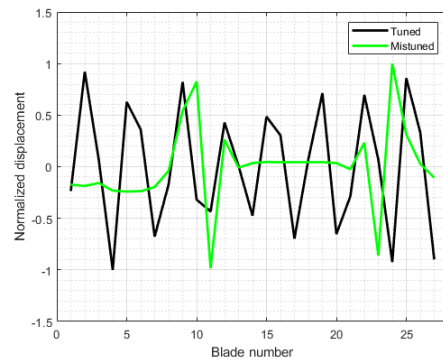
(a)  $r$



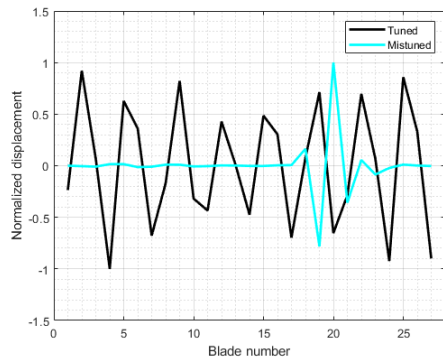
(b)  $a1$



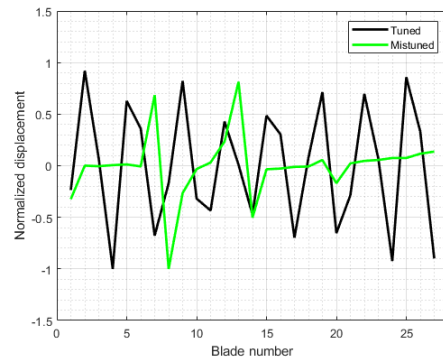
(c)  $a2$



(d)  $a3$

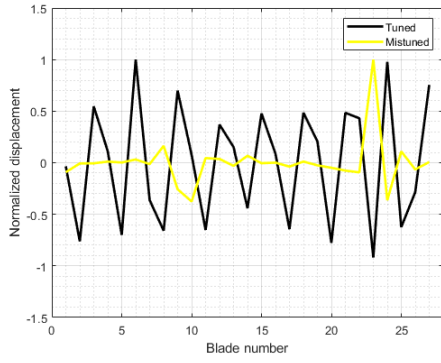


(e)  $g1$

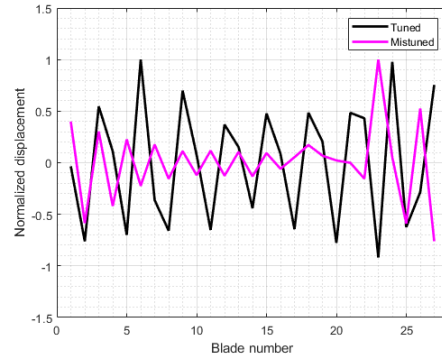


(f)  $g2$

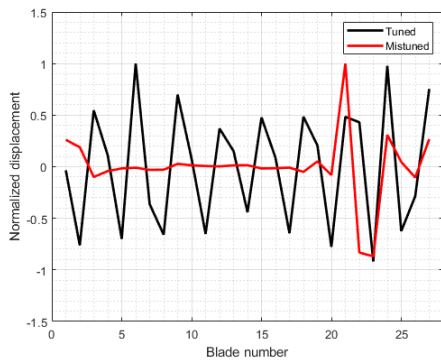
Figure C.8: Mode 8 variations in normalized displacements from tuned system for different mistuned patterns.



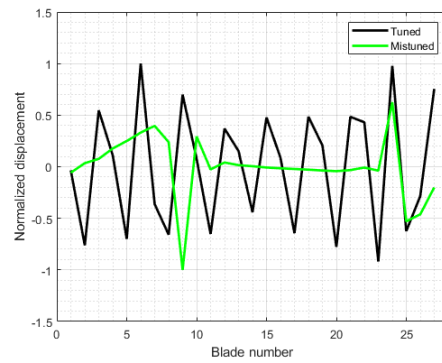
(a)  $r$



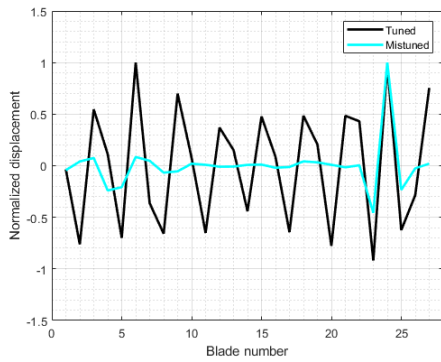
(b)  $a1$



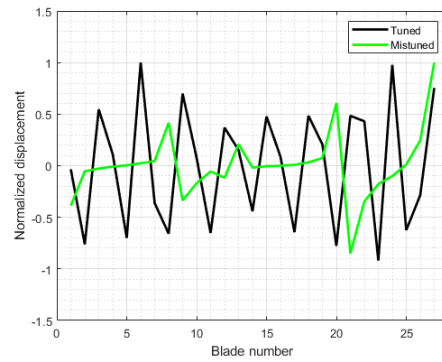
(c)  $a2$



(d)  $a3$

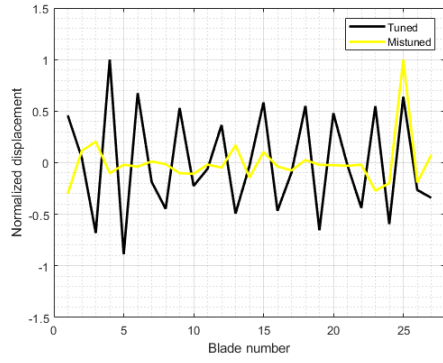


(e)  $g1$

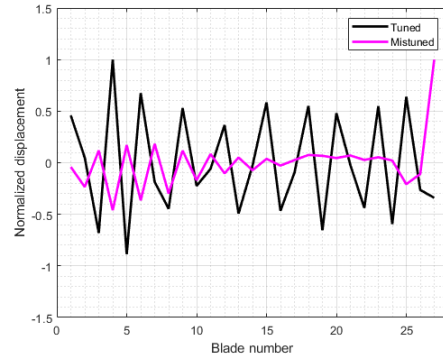


(f)  $g2$

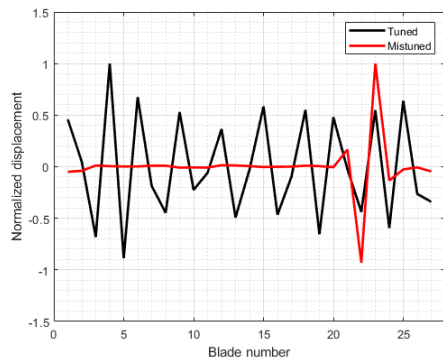
Figure C.9: Mode 9 variations in normalized displacements from tuned system for different mistuned patterns.



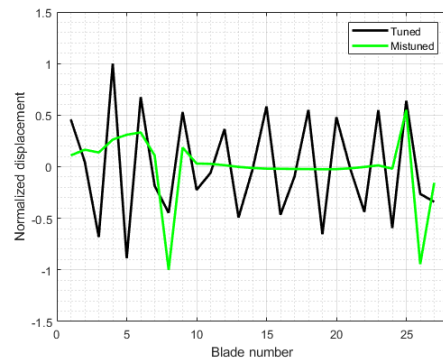
(a)  $r$



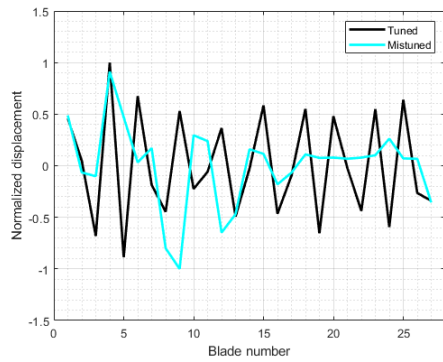
(b)  $a1$



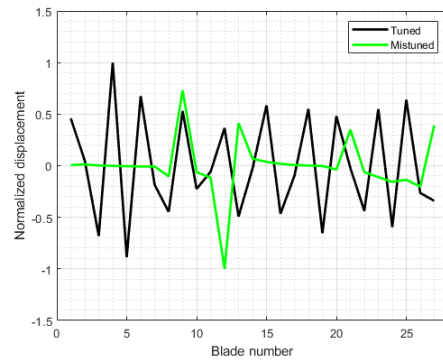
(c)  $a2$



(d)  $a3$

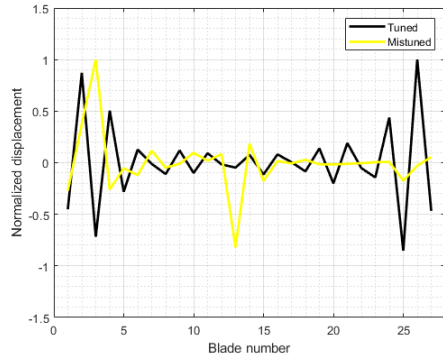


(e)  $g1$

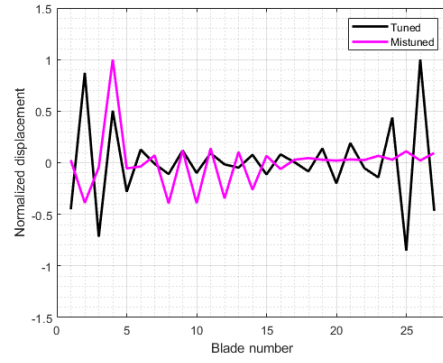


(f)  $g2$

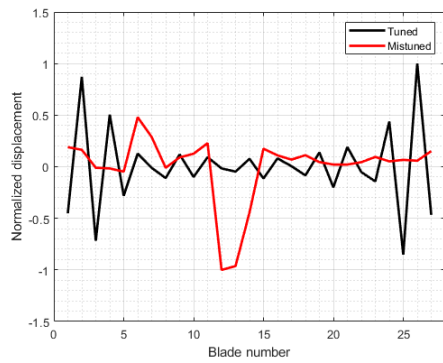
Figure C.10: Mode 10 variations in normalized displacements from tuned system for different mistuned patterns.



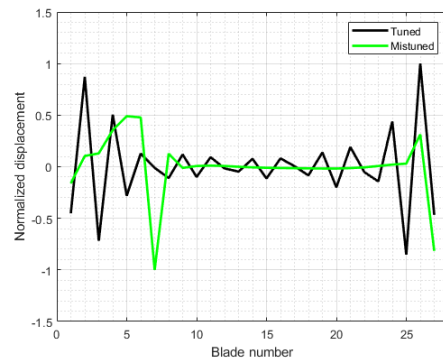
(a)  $r$



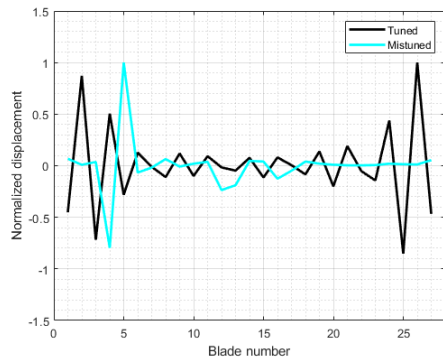
(b)  $a1$



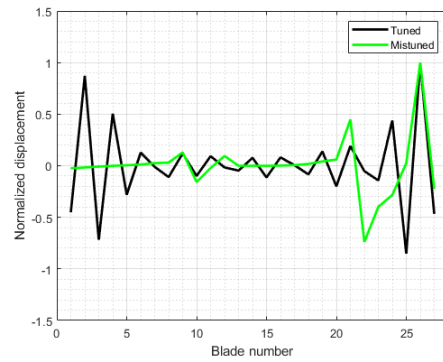
(c)  $a2$



(d)  $a3$

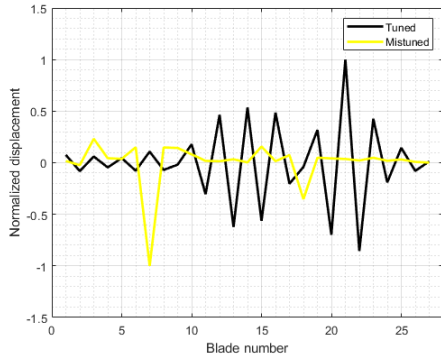


(e)  $g1$

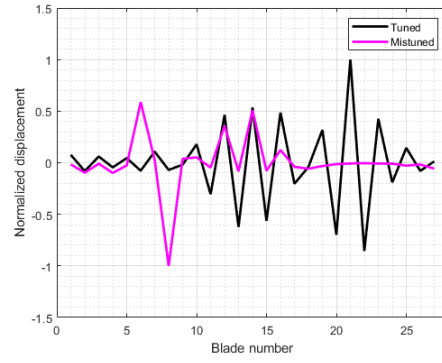


(f)  $g2$

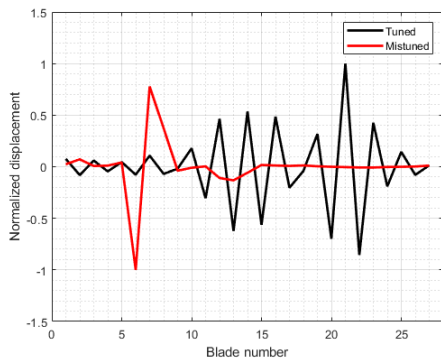
Figure C.11: Mode 11 variations in normalized displacements from tuned system for different mistuned patterns.



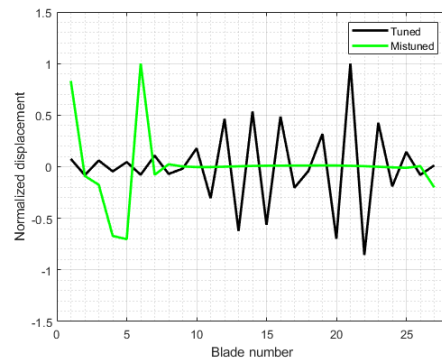
(a)  $r$



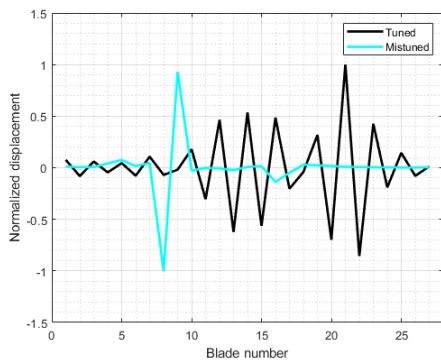
(b)  $a1$



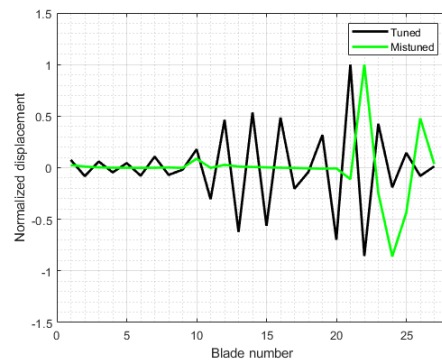
(c)  $a2$



(d)  $a3$

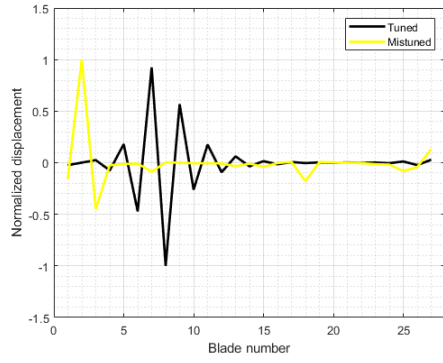


(e)  $g1$

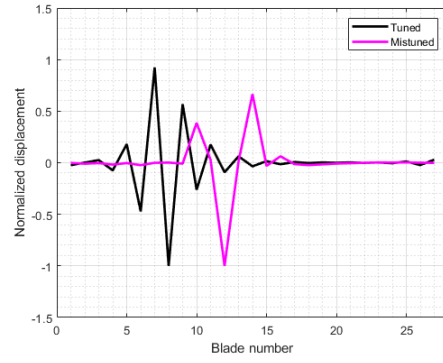


(f)  $g2$

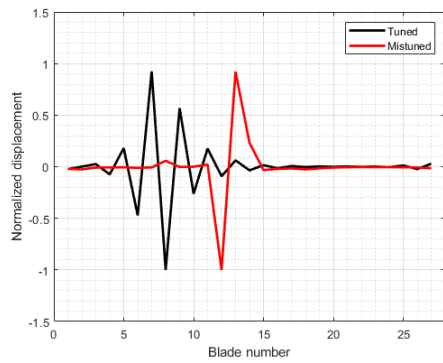
Figure C.12: Mode 12 variations in normalized displacements from tuned system for different mistuned patterns.



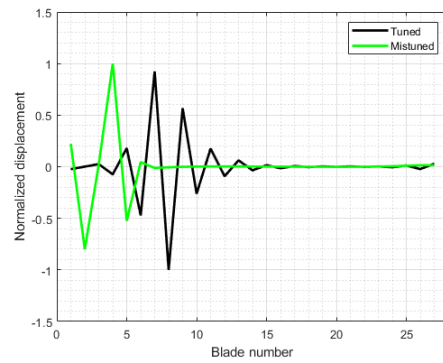
(a)  $r$



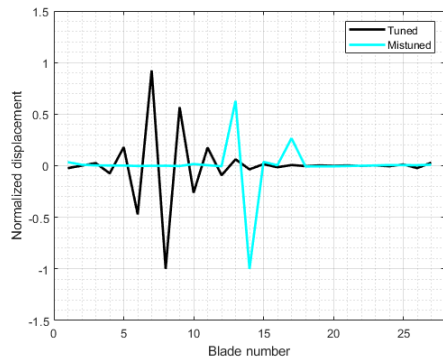
(b)  $a1$



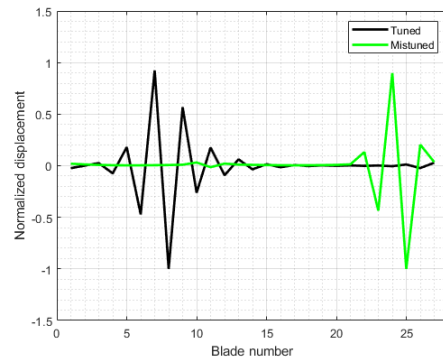
(c)  $a2$



(d)  $a3$



(e)  $g1$



(f)  $g2$

Figure C.13: Mode 13 variations in normalized displacements from tuned system for different mistuned patterns.

# Bibliography

- [1] **Srinivasan, A.V. (1997)**, "Flutter and Resonant Vibration Characteristics of Engine Blades", *ASME Journal of Engineering for Gas Turbines and Power*, Vol. 119
- [2] **Choi, B.K., Lents, J., Rivas-Guerra, A.J. and Mignolet, M.P., (2003)**, "Optimization of Intentional Mistuning Patterns for the Reduction of the Forced Response Effects of Unintentional Mistuning: Formulation and Assessment", *ASME Journal of Engineering for Gas Turbines and Power*, Vol. 125
- [3] **Thomson, D. E., and Griffin, J. T.,** "The National Turbine Engine High Cycle Fatigue Program", *Global Gas Turbine News*, Vol. 39
- [4] **JSC Kuznetsov** URL: <http://www.kuznetsov-motors.ru>
- [5] URL: <http://www.numeca.com/products>
- [6] **ANSYS, Inc. (2010)** "ANSYS Customer Training Material"
- [7] **NUMECA Int.** "Numeca Autogrid5 User Guide - version FINE™/Turbo 10.1"
- [8] **Spalart, P. R. and Allmaras, S. R., (1994)** "A one-Equation Turbulence Model for Aerodynamic Flows", *Recherche Aerospatiale*, No. 1, pp. 5-21
- [9] **Lonnie, R. and Royce, D. M., (1978)** "Design and Overall Performance of Four Highly Loaded, High-Speed Inlet Stages for an Advanced High-Pressure-Ratio Core Compressor", *NASA Technical Paper 1337*
- [10] **Castanier, M. P. and Pierre, C., (2006)** "Modeling and Analysis of Mistuned Bladed Disk Vibration: Status and Emerging Directions", *Journal of Propulsion and Power*, Vol. 22, No. 2
- [11] **ANSYS, Inc. (2010)** "ANSYS Help 16.2"
- [12] **Beirow, B., Giersch, T., Kuhhorn, A. and Nipkau, J. (2014)**, "Forced Response Analysis of Mistuned Compressor Blisk", *ASME Journal of Engineering for Gas Turbines and Power*, Vol. 136